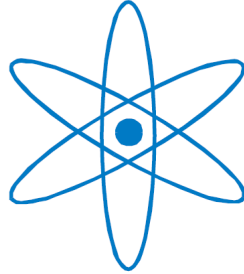


PHYSIK-DEPARTMENT



Studies of Scintillator Optical Properties,
Electronics Simulation and Data Analysis for
the BOREXINO Neutrino Experiment

Dissertation
von

Timo Lewke



TECHNISCHE UNIVERSITÄT
MÜNCHEN

TECHNISCHE UNIVERSITÄT MÜNCHEN
Physik-Department
Lehrstuhl für Experimentalphysik und Astroteilchenphysik
Univ.-Prof. Dr. Stefan Schönert

Studies of Scintillator Optical Properties, Electronics Simulation and Data Analysis for the BOREXINO Neutrino Experiment

Timo Lewke

Vollständiger Abdruck der von der Fakultät für Physik der Technischen Universität München zur Erlangung des akademischen Grades eines

Doktors der Naturwissenschaften (Dr. rer. nat.)

genehmigten Dissertation.

Vorsitzender: Univ.-Prof. Dr. Alejandro Ibarra

Prüfer der Dissertation: 1. Univ.-Prof. Dr. Lothar Oberauer

2. Priv.-Doz. Dr. Hubert Kroha

Die Dissertation wurde am 08.08.2013 bei der Technischen Universität München eingereicht und durch die Fakultät für Physik am 18.10.2013 angenommen.

Abstract

Borexino is a state-of-the-art low-energy neutrino detector. Many results, like the first real-time measurement of ${}^7\text{Be}$ neutrinos and the detection of pep neutrinos, could be reported. However, still some parts of the solar neutrino spectrum remain unseen. With a better detector understanding and monitoring these unexploited regions could be investigated. The results achieved in course of the present thesis account for accomplishing these improvements.

First, the ionization quenching for electrons in liquid scintillators is investigated using a specially designed and build experiment. This effect is especially interesting for low-energy events and, therefore, has a direct influence on the possibility to detect CNO and pp neutrinos. With a coincidence circuit and the properties of Compton scattering the quenching is analysed. Further, the so-called Birks factor k_B is measured for the scintillator used in the running Borexino experiment. As the Birks factor is also an important input parameter to simulations of the future large scale neutrino experiment LENA, the Birks factor of LENA's most probable scintillator is determined as well.

Second, as muons are responsible for a large amount of background, an excellent working muon veto is essential. During this thesis, it was achieved to monitor the muon tagging stability and efficiency for a long period of time.

Further, to verify the muon track reconstruction Monte Carlo simulations are needed. For the Inner Detector of Borexino the simulation is fully operable. In course of this thesis the complete electronics system of the Outer Detector is included into the simulation tool. In this way, a functioning simulation mimicking real physical events is generated. In addition, the output of the simulation can now be accessed and evaluated by the normal data handling system of Borexino. A comparison to real data and, therefore, validating the muon track reconstruction is now possible.

Last, to check the neutron tagging, CNGS neutrino beam induced muons and their respective neutrons are investigated. As result, the production rate of low-energy neutrons within the scintillator volume of Borexino is determined.

Zusammenfassung

Borexino ist ein hochmoderner Niederenergie-Neutrino-detektor. Viele Resultate, wie die erste Echtzeit-Messung der ${}^7\text{Be}$ Neutrinos und der Nachweis von pep Neutrinos, konnten berichtet werden. Jedoch bleiben nach wie vor Teile des solaren Neutrinospektrums ungehen. Mit einem besseren Detektorverständnis und einer besseren Detektorüberwachung können auch diese, bis dato noch unentdeckten Bereiche erkundet werden. Die Ergebnisse dieser Arbeit, dienen dazu einige dieser Verbesserungen einzuführen.

Zuerst wird das ionisations Quenching für Elektronen in Flüssigszintillatoren in einem speziell entwickelten und gefertigten Experiment untersucht. Dieser Effekt ist besonders für niederenergetische Ereignisse interessant, und hat deswegen einen direkten Einfluss auf die Möglichkeit CNO und pp Neutrinos zu messen. Mit einer Koinzidenzmessung und den Eigenschaften der Compton-Streuung wird das Quenching analysiert. Weiter wird der sogenannte Birks-Faktor für den in Borexino verwendeten Szintillator gemessen. Da der Birks-Faktor auch eine wichtige Größe bei Simulationen für das zukünftige Neutrino-Großexperiment LENA ist, wird der Birks-Faktor zusätzlich noch für den geplanten LENA Szintillator bestimmt.

Als Zweites ist ein gut arbeitendes Myon-Veto wichtig, da ein großer Anteil des Untergrunds durch Myonen erzeugt wird. Während dieser Arbeit konnte die Stabilität und die Effizienz des Myonnachweises erstmals über einen großen Zeitraum überwacht und bestätigt werden.

Zur Verifikation der Rekonstruktion der Myonspur sind Monte Carlo Simulationen von nöten. Für Borexino's Inneren Detektor ist diese Simulation bereits voll funktionsfähig. Im Rahmen dieser Arbeit wurde die komplette Elektronik des Äußeren Detektors in das Simulationsmodul integriert. Auf diese Art wird eine funktionierende Simulation erzeugt, die den kompletten Einfluß der Detektoranordnung detailliert nachbilden kann. Ferner kann das Simulationsergebnis nun mit dem normalen Datenverarbeitungssystem von Borexino behandelt werden. Ein Vergleich mit echten Daten, und somit die Validierung der Myonspur-Rekonstruktion, ist jetzt möglich.

Zuletzt werden Myonen, die durch den CERN-Neutrinostrahl generiert werden und ihre zugehörigen Neutronen untersucht, um die Neutronenidentifizierung zu testen. Als Ergebnis wird die Produktionsrate von niederenergie Neutronen im Szintillatorvolumen von Borexino bestimmt.

Contents

| | | |
|----------|---|-----------|
| 1 | Neutrinos as Low-Energy Messengers | 1 |
| 1.1 | Neutrino Properties | 2 |
| 1.2 | Solar Neutrinos | 4 |
| 1.3 | Supernova Neutrinos | 6 |
| 1.4 | Diffuse Supernova Neutrino Background | 7 |
| 1.5 | Geoneutrinos | 8 |
| 2 | Real-Time Neutrino Detection | 11 |
| 2.1 | Liquid-Scintillator Detectors | 11 |
| 2.2 | Neutrino Interactions at Low Energies | 12 |
| 2.2.1 | Elastic Scattering | 12 |
| 2.2.2 | Inverse Beta Decay | 14 |
| 2.2.3 | CC and NC Interactions with Carbon | 14 |
| 2.3 | Borexino Detector Design | 15 |
| 3 | Liquid Scintillator | 19 |
| 3.1 | Theoretical Properties | 19 |
| 3.2 | Attenuation Length | 21 |
| 3.3 | Light Yield | 21 |
| 3.4 | Quenching Effect | 22 |
| 3.4.1 | The Birks Factor | 24 |
| 4 | Quenching Experiment | 25 |
| 4.1 | Experimental Method | 25 |
| 4.2 | Experimental Setup | 26 |
| 4.2.1 | Measurement Setup | 27 |
| 4.2.2 | Electronics and DAQ | 29 |
| 4.3 | Investigated Scintillators | 30 |
| 4.4 | Light Yield Test Measurements | 31 |
| 4.5 | Quenching Measurements | 33 |
| 4.6 | Systematic Uncertainties | 35 |
| 4.6.1 | Setup Accuracy | 37 |
| 4.6.2 | System Stability | 38 |

| | | |
|----------|---|-----------|
| 4.7 | Results – Birks Factor | 40 |
| 5 | BOREXINO Background Rejection | 45 |
| 5.1 | Background Signals | 45 |
| 5.1.1 | Radioactive Contaminants | 45 |
| 5.1.2 | Muons | 46 |
| 5.1.3 | Muon Induced Spallation Processes | 46 |
| 5.1.4 | Neutrons | 47 |
| 5.2 | BOREXINO’s Outer Detector | 47 |
| 5.2.1 | Electronics | 47 |
| 5.2.2 | Electronics Stability | 50 |
| 5.2.3 | Electronics Simulation (BxElec) | 53 |
| 5.2.4 | Outer Detector Performance | 61 |
| 5.3 | CNGS-Beam induced Neutrons | 66 |
| 5.3.1 | Data Selection | 66 |
| 5.3.2 | Applied Cuts | 66 |
| 5.3.3 | Neutron Multiplicity | 68 |
| 6 | BOREXINO Results and Prospects | 71 |
| 6.1 | BOREXINO Results | 71 |
| 6.1.1 | ^7Be Neutrinos | 71 |
| 6.1.2 | ^8B Neutrinos | 72 |
| 6.1.3 | pep Neutrinos and CNO Neutrino Limit | 75 |
| 6.1.4 | Geoneutrinos | 78 |
| 6.1.5 | Neutrino Velocity Measured with the CNGS-Beam | 80 |
| 6.2 | BOREXINO Prospects | 80 |
| 6.2.1 | CNO Neutrinos | 80 |
| 6.2.2 | pp Neutrinos | 80 |
| 6.2.3 | Short Distance Neutrino Oscillations | 81 |
| 6.2.4 | Supernova Neutrinos | 82 |
| 7 | The LENA Project | 83 |
| 7.1 | Detector Design | 83 |
| 7.2 | Physics Program | 85 |
| 8 | Conclusion & Outlook | 89 |
| | List of Figures | 91 |
| | List of Tables | 94 |
| | References | 95 |

Chapter 1

Neutrinos as Low-Energy Messengers

A long time after neutrinos had been postulated by Wolfgang Pauli in 1930 as a consequence of missing energy and spin in a β -decay of radioactive nuclei [1] it was possible to measure them. So it had been 23 years until Frederick Reines and Clyde L. Cowan were able to detect the particle for the first time [2]. Up to our days, many neutrino issues have been solved. One of the most prominent questions was the so-called Solar Neutrino Problem, the difference between the measured and the expected neutrino flux from the sun. The neutrino deficit was observed by several neutrino experiments [3][4][5][6] and finally was explained by neutrino oscillations [7]. Efforts in determining the parameters of neutrino oscillations were made, using new experiments [8][9][10][11][12][13], but still a lot of parameters remain unknown: the hierarchy of neutrino mass eigenstates, the neutrino mass itself, the CP violating phase δ in the mixing matrix. Even questions concerning the very fundamental properties of the particle itself, Majorana or Dirac, are not yet understood [14].

Nevertheless, it is possible probing the universe with neutrinos. The well known fact that neutrinos interact very rarely with matter and that they do not interfere with magnetic fields offers a great opportunity to examine their production processes and points of origin. Thereby they can be classified in high-energetic and low-energetic neutrinos. Whereas the high-energetic ones are examined by large-volume neutrino telescopes like IceCube [15] or ANTARES [16], this work will focus on the low-energetic neutrino experiments Borexino [17] and LENA [18] (see chapter 6 and 7, respectively). The energy window observed ranges from 100 keV up to 50 MeV. Because the different neutrino sources observed produce neutrinos with energies very similar to each other, it is important to have a good detector energy resolution and background understanding. This includes the understanding of the used electronics as well as knowing all the different properties of the organic liquid scintillator used.

1.1 Neutrino Properties

Neutrinos are included in the Standard Model [19][20] and fit smoothly in the three generation fermion scheme (table 1.1). They are regarded as massless left-handed particles

| Fermions | Family | | | el. charge | color | weak Isospin | | Spin |
|----------|---------|-----------|------------|------------|-------|--------------|--------------|------|
| | 1 | 2 | 3 | | | left handed | right handed | |
| Leptons | ν_e | ν_μ | ν_τ | 0 | — | 1/2 | — | 1/2 |
| | e | μ | τ | -1 | — | 1/2 | 0 | |
| Quarks | u | c | t | +2/3 | r,g,b | 1/2 | 0 | 1/2 |
| | d | s | b | -1/3 | r,g,b | 1/2 | 0 | |

Table 1.1: Generation scheme for fermions as applied in the Standard Model (translated from [20])

| Boson | Mass | Interaction |
|---------|--------|-----------------|
| W^\pm | 80 GeV | charged current |
| Z^0 | 91 GeV | neutral current |

Table 1.2: Exchange bosons of the weak interaction with their related masses and interaction process [20]

that interact via exchange of massive vector bosons (table 1.2), in processes of charged or neutral current interactions. However, neutrino oscillations require mass afflicted particles. Hence, it is necessary to look beyond the Standard Model. An overview of different models introducing neutrino masses can be found in several publications [14][21][22].

There are two different neutrino mixing mechanisms. The first are vacuum oscillations. Analogous to the hadronic CKM matrix the weak interaction eigenstates of neutrinos ν_α , $\alpha = e, \mu, \tau$, are mixtures of the mass eigenstates ν_i , $i = 1, 2, 3$. The mixing can be described using the PMNS¹ matrix U and leads to equations 1.1 and 1.2 [21][23],

$$|\nu^\alpha\rangle = \sum_i U_{\alpha i} |\nu^i\rangle \quad (1.1)$$

with

$$U = \begin{pmatrix} 1 & 0 & 0 \\ 0 & c_{23} & s_{23} \\ 0 & -s_{23} & c_{23} \end{pmatrix} \begin{pmatrix} c_{13} & 0 & s_{13}e^{i\delta} \\ 0 & 1 & 0 \\ -s_{13}e^{i\delta} & 0 & c_{13} \end{pmatrix} \begin{pmatrix} c_{12} & s_{12} & 0 \\ -s_{12} & c_{12} & 0 \\ 0 & 0 & 1 \end{pmatrix} \quad (1.2)$$

where $s_{ij} = \sin \theta_{ij}$, $c_{ij} = \cos \theta_{ij}$ and δ is the phase for possible CP-violations. Taking time development into account, equation 1.1 transforms into

$$|\nu^\alpha\rangle_t = \sum_i U_{\alpha i} e^{-iE_i t} |\nu^i\rangle \quad (1.3)$$

¹Named after Pontecorvo, Maki, Nakagawa and Sakata for introducing this formalism

The probability for a neutrino ν_α travelling the distance L with energy E , to transfer into a neutrino $\nu_{\alpha'}$ is given by [14]

$$P(\nu_\alpha \rightarrow \nu_{\alpha'}) = \left| \sum_i U_{\alpha'i} e^{-i\Delta m^2 \frac{L}{2E}} U_{\alpha i}^* \right|^2. \quad (1.4)$$

Looking at neutral current (NC) and charged current (CC) interactions of neutrinos, a second oscillation mechanism must be regarded: matter-induced oscillations. The different potential of electron neutrinos (CC and NC interaction) and muon/tau neutrinos (only NC interaction) traversing matter leads to a greatly enhanced conversion of ν_e into ν_μ and ν_τ [21]. This mechanism, the MSW mechanism², is the most attractive solution to the Solar Neutrino Problem. Also considered is an extra contribution to the electron neutrino energy in equation 1.3 of $\sqrt{2}G_F n_e$ that is formed by the electrons of the traversed matter (see [21] for detailed information). Here, n_e is the electron number density in matter and G_F the Fermi constant. The matter oscillation angle $\tilde{\theta}$ can be expressed by the values of the vacuum oscillation angle θ . Because sufficient, only a two neutrino case is demonstrated in the following [21]:

$$\sin 2\tilde{\theta} = \frac{\sin 2\theta}{\sqrt{(A/\Delta m^2 - \cos 2\theta)^2 + \sin^2 2\theta}}, \quad (1.5)$$

where $A = 2\sqrt{2}EG_F n_e$. The new mass eigenvalues can be calculated to

$$\tilde{m}_{1,2}^2 = \frac{A}{2} \mp \frac{1}{2} \sqrt{(A - \Delta m^2 \cos 2\theta)^2 + (\Delta m^2)^2 \sin^2 2\theta}. \quad (1.6)$$

Regarding equation 1.6 as a function of n_e leads to a level-crossing phenomenon. It plays an important role in solar neutrino physics and can explain the conversion of a neutrino, e.g. an electron neutrino generated by a fusion process in the core of the sun propagating to the surface (see figure 1.1). The level-crossing respectively resonance occurs at the electron number density of

$$n_e = n_{e,res} = \frac{1}{2\sqrt{2}G_F} \frac{\Delta m^2}{E} \cos 2\theta \quad (1.7)$$

A lot of experiments aim to measure one of the many different neutrino properties described in this section. Good results for θ_{12} have been achieved by solar neutrino experiments like SNO [24], KamLAND [25] and Super-Kamiokande [26]. The atmospheric mixing angle θ_{23} was observed by MINOS [27] and Super-Kamiokande [28]. The short-baseline reactor experiments Double-Chooz [8], DayaBay [9] and RENO [29] were able to give values for θ_{13} . Also strenuous effort is or was made to determine the neutrino masses, for example by MAINZ [30], KATRIN [31], GERDA [32]. A summary of some neutrino oscillation data is given in table 1.3.

²named by Mikheyev, Smirnov and Wolfenstein

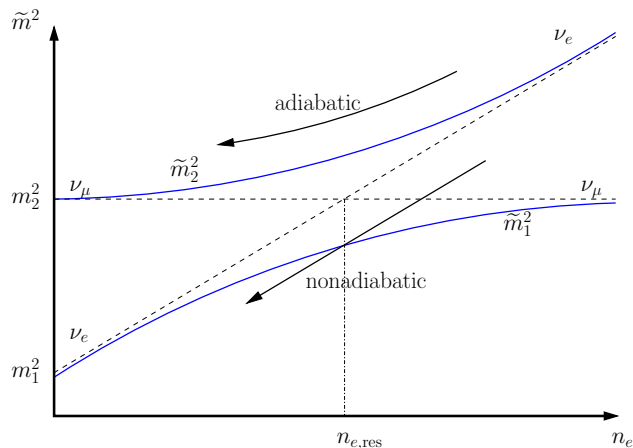


Figure 1.1: Survival probability of a generated ν_e (upper right side) taking the passed solar matter into account. There are two possible branches: the upper, adiabatic one and the lower, non adiabatic one. Under adiabatic conditions, a ν_e will leave the sun surface in the mass eigenstate ν_2 and, therefore, will be converted into a ν_μ (see [23] for additional information).

1.2 Solar Neutrinos

In our days, with most of the basic neutrino properties being known, it is possible to use neutrinos as messengers. They can be regarded as distinguished probes to learn about physics processes linked to their production, propagation and, hence, their sources of origin. The first source to mention is the sun. Due to solar neutrinos, the different fusion processes taking place in the center of the sun can be investigated. Depending on the different fusion reactions in the pp-/pep-chain and CNO-cycle (see figures 1.2 and 1.3), tests of underlying models can be performed. The net reaction for the pp- /pep-chain and CNO-cycle is given by



| Parameter | Best Fit $\pm 1\sigma$ | 3σ Intervall |
|---|---------------------------|---------------------|
| Δm_\odot^2 [10^{-5} eV^2] | $7.58^{+0.22}_{-0.26}$ | 6.99 – 8.18 |
| Δm_A^2 [10^{-5} eV^2] | $2.35^{+0.12}_{-0.09}$ | 2.06 – 2.67 |
| $\sin^2 \theta_{12}$ | $0.312^{+0.018}_{-0.015}$ | 0.265 – 0.364 |
| $\sin^2 \theta_{23}$ | $0.42^{+0.08}_{-0.03}$ | 0.34 – 0.64 |
| $\sin^2 \theta_{13}$ | 0.0251 ± 0.0034 | 0.015 – 0.036 |

Table 1.3: Neutrino properties as measured by different experiments, with the solar and atmospheric mass splitting $\Delta m_\odot^2 = \Delta m_{12}^2$ and $|\Delta m_A^2| = |\Delta m_{13}^2| \cong |\Delta m_{23}^2|$, respectively. (Data collected by the Particle Data Group in 2012 [33])

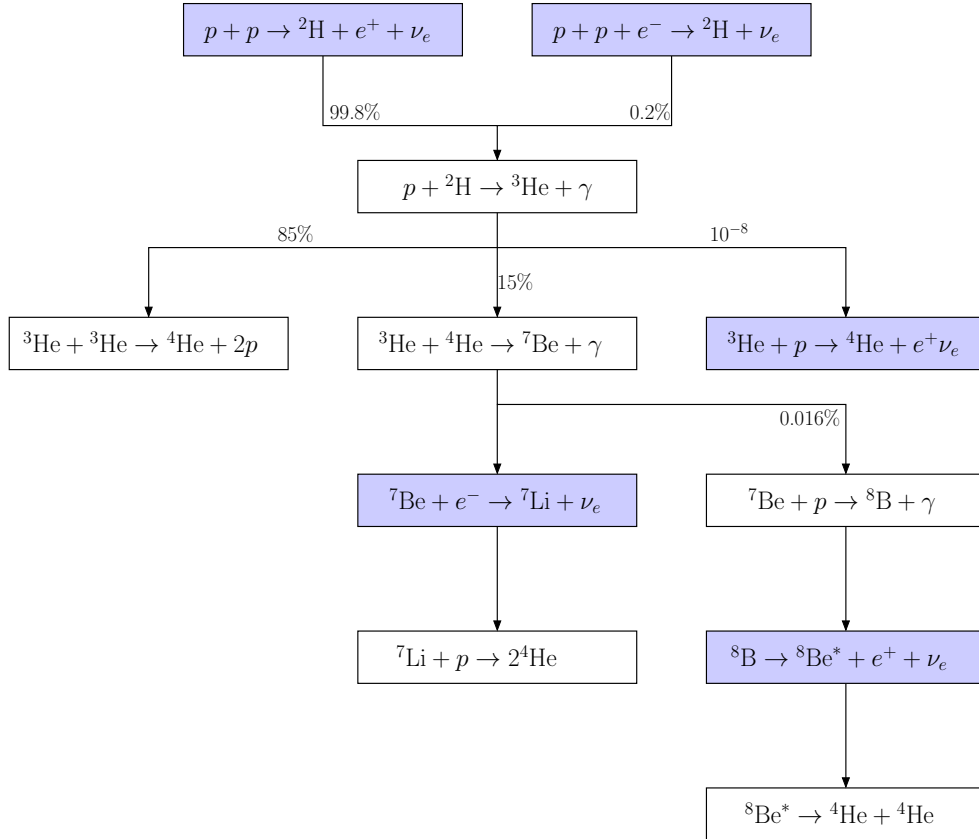


Figure 1.2: Fusion processes to ${}^4\text{He}$ taking place in the sun by the pp-chain. This chain contributes the biggest part of the sun's luminosity and solar neutrino flux. The ratios of the different sub-branches are depicted. The neutrino producing processes are highlighted.

Nevertheless, the neutrino energy is not the same for the different branches. It is strongly dependent on the products of its originating nuclear reaction. Compared to the pp-/pep-chain, the CNO-circles provides just a minor contribution to the total neutrino flux of the sun, as its rate is directly linked to the size of the star. Because of their small rate CNO neutrinos are difficult to detect experimentally. However, CNO neutrinos are important for understanding the solar fusion processes and have to be taken into consideration.

There are many different solar models (SM) predicting the neutrino spectrum [34] generated by these different fusions. One of the state-of-the-art spectrum is depicted in figure 1.4, as calculated by Bahcall in 2005 [35]. With ongoing neutrino experiments like Borexino (section 2.3), it is now possible to test, for example, this spectrum and, therefore, the underlying solar model (see chapter 6).

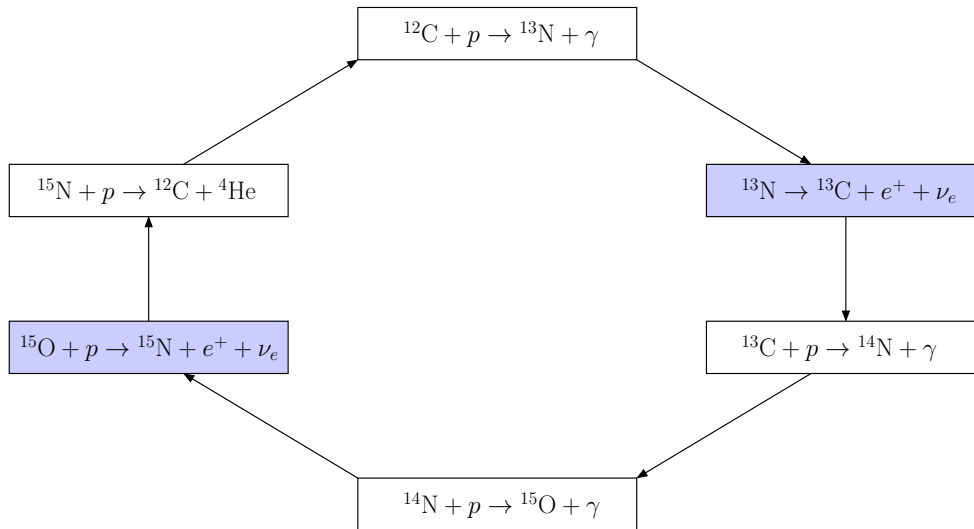


Figure 1.3: There are several possible CNO-cycles producing neutrinos in stars. For small stars like the sun, however, only one of these is prominent. Its reaction scheme is shown here. The neutrino producing processes are highlighted.

1.3 Supernova Neutrinos

The next object under investigation are core-collapse Supernovae (SN) dynamically dominated by neutrinos. When a massive star ($M \gtrsim 8M_{\text{Solar}}$) reaches the end of shell burning and the iron core is collapsing because the Fermi-pressure of electrons can't withstand the gravitational force, a shock wave is formed. This wave is pushing the shells outwards, while a neutron star or a black hole is remaining. Just a small part of the total energy emitted is linked to the kinetic energy of the shock front, most part is carried away by neutrinos. There are two different mechanisms powering and producing neutrinos. First is the so-called neutronisation burst. During the core collapse protons are turned into neutrons where electron neutrinos are emitted. As the remaining proto-neutron star is heating up, it is cooled by emitting $\nu\bar{\nu}$ -pairs of different flavors. This second mechanism for neutrino production is called neutrino cooling. The explosion is driven by these neutrinos, preventing the expansion from stalling. A more detailed view on the SN mechanism and the neutrino production theory can be found in [36][37]. Being different in time and energy (see figure 1.5), the neutrino burst and the following neutrino wind can be distinguished by experiments. So, it is possible to test different SN-models.

In addition, the neutrino signal should arrive on earth several hours before the trapped photons of the SN. For that reason an alert system called SNEWS (SuperNova Early Warning System [39]) was installed. Several neutrino telescopes participate in this project. When a certain amount of detectors detect a SN, an alarm is formed. The warning is sent to optical telescopes giving them the opportunity to observe the sky at the right position and time. So the SN can be investigated visually.

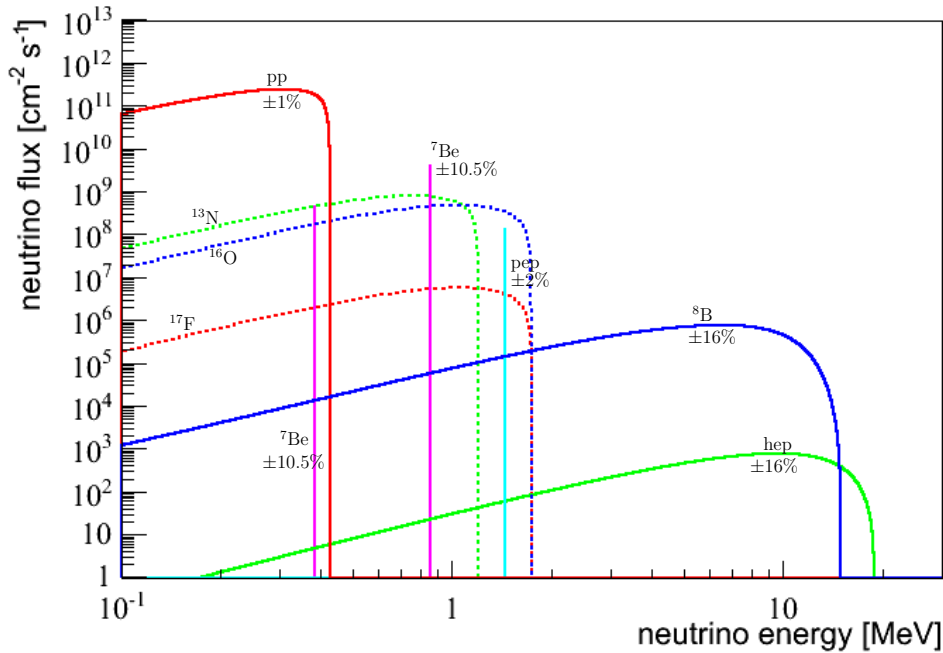


Figure 1.4: Calculation of the Standard Solar Model (SSM) neutrino spectra. The different neutrinos are color coded according to their production mechanism. The solid lines refer to neutrinos produced by the pp-/pep-chain, whereas the dotted lines refer to neutrinos produced by the CNO-cycle. Three produced neutrino sorts are mono energetic. Input data is taken from [35].

1.4 Diffuse Supernova Neutrino Background

Detectable SN have to be in a certain range from earth in order to be visible in the neutrino light. However, SN originate all over the universe. Soon the question aroused, if the radiation and the neutrinos emitted by SN far away could contribute to a visible background [40][41]. Today, the diffuse supernova neutrino background (DSNB) is regarded as the isotropically spread flux of all neutrinos and antineutrinos emitted by all core-collapse SN in the universe. Hence, the DSNB can be used as a regular source of SN neutrinos. Although it is not possible to detect the single SN far away, the total flux of all emitted neutrinos of all SN should yield a nonzero signal [42]. As it is assumed that the total star formation rate in the universe equals the total SN rate [42], an estimation of the DSNB flux at earth can be performed. As the neutrino sources are distributed isotropically and the earth can be regarded as transparent to neutrinos, the remaining integral is just a line of sight integral. Using the neutrino emission per SN, $\varphi(E_\nu)$, and the developing core-collapse SN rate $R_{SN}(z)$, the neutrino-number flux-spectrum $\frac{d\phi}{dE_\nu}$, in units of $\text{cm}^{-2}\text{s}^{-1}\text{MeV}^{-1}$, is (see [42])

$$\frac{d\phi}{dE_\nu}(E_\nu) = \int_0^\infty [(1+z)\varphi[E_\nu(1+z)]] [R_{SN}(z)] \left[\left| \frac{c dt}{dz} \right| dz \right]. \quad (1.9)$$

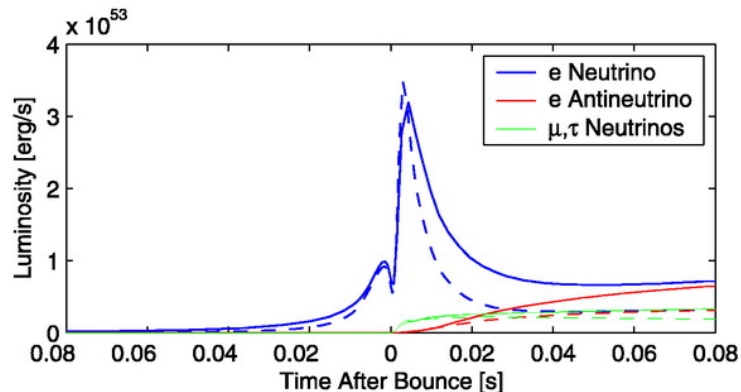


Figure 1.5: Neutrino flux development around the early time of a core collapse Supernova. The color indicates the different neutrino flavors, whereas the dashed and solid lines represent two different Supernova models. Clearly distinguishable are the neutronisation burst (mainly electron neutrinos) and the following neutrino cooling (increase of all neutrino flavors). Picture taken from [38], *reproduced by permission of the ASS*.

The first term in brackets is the emission spectrum $\varphi(E_\nu)$. The detected neutrino with energy E_ν was emitted with a higher energy $E_\nu(1+z)$, the pre-factor $(1+z)$ compresses the energy spectra due to redshift z . The second term is the already mentioned SN rate density $R_{SN}(z)$. The differential distance is given by the third term, where $dt/dz = H_0(1+z)[\Omega_\Lambda + \Omega_m(1+z)^3]^{1/2}$, using the cosmological parameters $H_0 = 70 \text{ km s}^{-1} \text{ Mpc}^{-1}$, $\Omega_m = 0.3$ and $\Omega_\Lambda = 0.7$ [42].

Hence, the detectable signal at earth is dependent on two parameters: the cosmic SN rate and the SN neutrino emission. In addition the detected signal is influenced by the detector itself. The different detectability of neutrinos at detectors and the impact of the DSNB signal on different fields of physics can be found in [43]. The possibility to use the DSNB as a probe for neutrino oscillations is discussed in [44]. First results regarding the DSNB have been published by the SuperKamiokande collaboration [45]. Using almost 1500 days of data, new limits on the total flux of different theoretical models were set, in the absence of a signal (see table 1.4). As the DSNB hasn't been measured directly yet, future detectors include the DSNB analysis in their R&D-phase. Two promising detectors for the DSNB confirmation are LENA [46], that will be explained in detail in chapter 7, and GLACIER [47].

1.5 Geoneutrinos

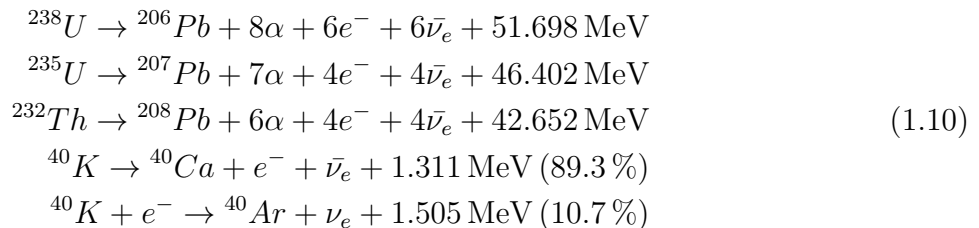
The last neutrino source to be mentioned in this introduction, is the earth itself. Here, the so-called geoneutrinos are generated. This was assumed quite early in the middle of the last century, taking into account neutrinos from the radioactive decay of Potassium

| Theoretical model | Event rate limit (90% C.L.) | SRN flux limit (90% C.L.) | Predicted flux | Predicted flux ($E_\nu > 19.3$ MeV) |
|---------------------------|--------------------------------|---|--|---|
| Galaxy evolution | < 3.2 events/yr | $< 130\bar{\nu}_e \text{ cm}^{-2}\text{s}^{-1}$ | $44\bar{\nu}_e \text{ cm}^{-2}\text{s}^{-1}$ | $0.41\bar{\nu}_e \text{ cm}^{-2}\text{s}^{-1}$ |
| Cosmic gas infall | < 2.8 events/yr | $< 32\bar{\nu}_e \text{ cm}^{-2}\text{s}^{-1}$ | $5.4\bar{\nu}_e \text{ cm}^{-2}\text{s}^{-1}$ | $0.20\bar{\nu}_e \text{ cm}^{-2}\text{s}^{-1}$ |
| Cosmic chemical evolution | < 3.3 events/yr | $< 25\bar{\nu}_e \text{ cm}^{-2}\text{s}^{-1}$ | $8.3\bar{\nu}_e \text{ cm}^{-2}\text{s}^{-1}$ | $0.39\bar{\nu}_e \text{ cm}^{-2}\text{s}^{-1}$ |
| Heavy metal abundance | < 3.0 events/yr | $< 29\bar{\nu}_e \text{ cm}^{-2}\text{s}^{-1}$ | $< 54\bar{\nu}_e \text{ cm}^{-2}\text{s}^{-1}$ | $< 2.2\bar{\nu}_e \text{ cm}^{-2}\text{s}^{-1}$ |
| Constant supernova rate | < 3.4 events/yr | $< 20\bar{\nu}_e \text{ cm}^{-2}\text{s}^{-1}$ | $52\bar{\nu}_e \text{ cm}^{-2}\text{s}^{-1}$ | $3.1\bar{\nu}_e \text{ cm}^{-2}\text{s}^{-1}$ |
| Large mixing angle osc. | < 3.5 events/yr | $< 31\bar{\nu}_e \text{ cm}^{-2}\text{s}^{-1}$ | $11\bar{\nu}_e \text{ cm}^{-2}\text{s}^{-1}$ | $0.43\bar{\nu}_e \text{ cm}^{-2}\text{s}^{-1}$ |

Table 1.4: The supernova relic neutrino (SRN) search results as reported by the SuperKamiokande collaboration for six theoretical models (shown in the first column). The efficiency-corrected limit on the SRN event rate is depicted in the second column. The new calculated flux limit is shown in the third column. The theoretical predictions are shown in the fourth column. The fifth column contains the $\bar{\nu}$ -flux predictions above a threshold of $E_\nu > 19.3$ MeV. The data shown is taken from [45] including references.

and from the radioactive decay chains of Thorium and Uranium (see [48]). At that time radiochemical detectors, e.g. using chlorine as detector material, measured the neutrino flux only time- and energy-integrated and were just sensitive to neutrinos and not anti-neutrinos. Hence, the small rate of geoneutrinos was expected not to be detectable.

The neutrino-generating decays taking place in the earth's crust and mantle are as following [49]:



Models assume that the energy provided by the processes quoted in equation 1.10, contribute 50 % to the total terrestrial heat flow of about 40 TW. The rest of the energy should be provided by crystallization of the liquid outer core [50] and by a natural georeactor located in the core itself [51]. An overview of the geoneutrino sector can be found in [49], including different earth and crust models.

The first results on a measurement of geoneutrinos originating from the $^{238}\text{U}/^{232}\text{Th}$ -chains were reported by the KamLAND collaboration in 2005 [52]. Taking into account the detection efficiency, life-time and number of target protons, a detected geoneutrino rate of $5.1_{-3.6}^{+3.9} \cdot 10^{-31} \bar{\nu}_e$ per target proton per year was reported in good agreement with the different models. The energy distribution of all uncut candidates is depicted in figure 1.6. An upper limit on the power of the georeactor was set to 60 TW.

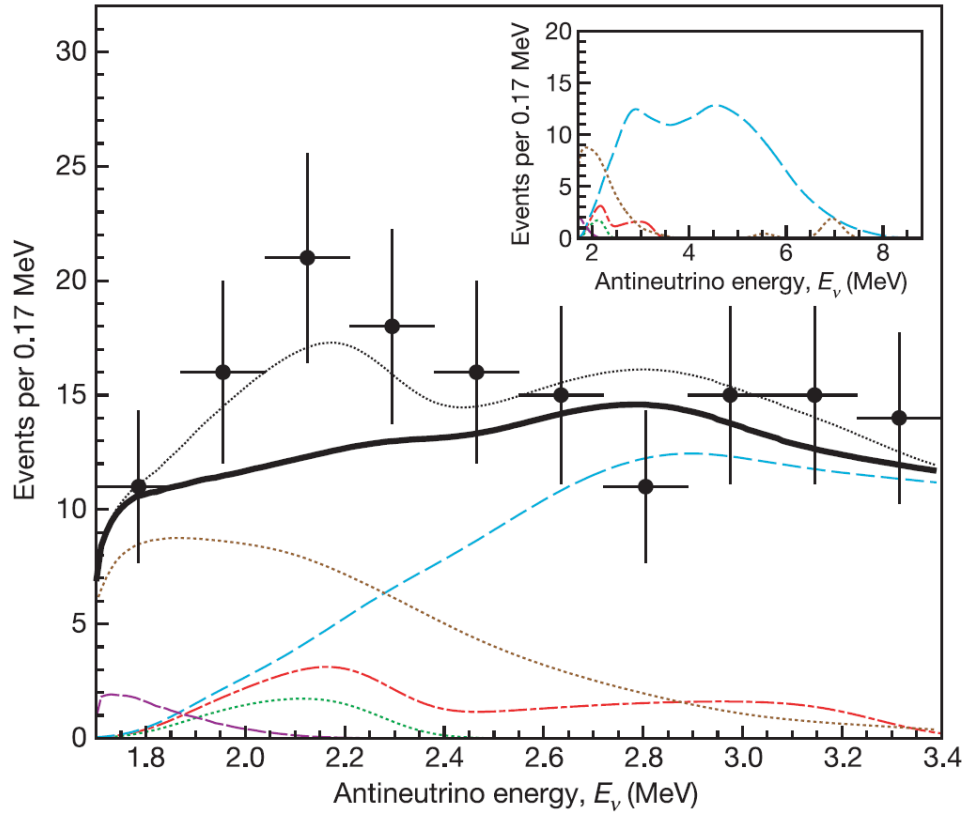


Figure 1.6: Geoneutrino spectrum as reported by KamLAND [52] (*reprinted by permission from Macmillan Publishers Ltd*). The thin black dotted line in the main panel shows the total expected energy spectrum in agreement with the experimental data (black dots including error bars). The spectrum with no geoneutrinos is given by the black solid line. The expected geoneutrino contribution originated by ^{238}U - and ^{232}Th -decay chain is depicted by the red and the green line, respectively. The main background source are reactor $\bar{\nu}_e$ (blue line). The remaining brown line is due to $^{13}\text{C}(\alpha, n)^{16}\text{O}$ reactions, the purple line is due to existing random coincidences. The inset shows the extension of the spectrum to higher energies.

Chapter 2

Real-Time Neutrino Detection

As mentioned in the previous chapter the early radiochemical detectors [3][4][5][6] were only able to measure the time- and energy-integrated neutrino fluxes. The first measurements of neutrinos were performed in that way, but soon the detectors were limited by their detection principles. New detectors were developed, so called water Cherenkov detectors. The first one was the KamiokaNDE detector [53], the most prominent one the Super-Kamiokande detector [54], which is still taking data. With these detectors it was possible to measure some parts of the solar neutrino spectra in real-time. But due to the high energy threshold of 5 MeV, the low energy part remained unobserved (see figure 1.4). A solution for this problem is the use of organic liquid-scintillator detectors. This detection principle will be discussed in this chapter.

2.1 Liquid-Scintillator Detectors

The state-of-the-art detector principle for low energy solar neutrino physics is the liquid scintillator detector. These detectors have the great advantage that the energy threshold is typically in the keV range. In order to achieve this, a high level of radiopurity has to be obtained during the construction phase. Therefore, strict requirements on radiopurity are set in the R&D-phase and are later-on monitored accurately. In addition, in some cases an afterward cleaning has to be performed to grant the stability of the used scintillator. An overview can be found in [55][56] describing the processes and achievements of purification done and achieved by the Borexino collaboration.

The main part of such a detector is the liquid scintillator observed by photomultiplier tubes (PMTs)[57]. The different designs of the containment of different detectors vary due to the different purposes of the different projects.¹ Particles passing the active detector volume scatter mainly off scintillator electrons generating excited states of the liquid scintillator molecules. The interaction processes are described in sections 2.2.1 - 2.2.3, scintillator properties will be discussed in detail in chapter 3. The relaxation of the excited state to the ground state releases photons. In order to detect the emitted photons with the PMTs,

¹As an example, the Borexino layout will be described in detail in section 2.3

the wavelength of the emitted light has to be shifted by a dissolved flour to approximately 400 nm. Using the time and energy information obtained by the PMTs the position of the particle hit can be reconstructed. Compared to water Cherenkov detectors, a low energetic neutrino hit only generates a point-like hit pattern. Only higher energetic particles like muons are able to generate tracks inside the liquid scintillator volume. But there are unwanted background events in the low energy range that produce a point-like hit signature. Therefore, neutrino hits can be mimicked in first order by a background events.

There are several processes to discriminate between signal and background events. The first step is of course to reduce background events. Therefore, neutrino detectors are build in underground laboratories. The overburden of rock provides a good shielding against unwanted cosmic radiation. Nevertheless, high-energy muons still reach the detector, or produce particles in the surrounding rock entering the detector. Also impurities contained inside the detector cannot be shielded. This kind of unavoidable background has to be distinguished from the neutrino signal in the data analysis. Prominent examples to discriminate between signal and background are the usage of the coincidence signals of inverse beta decay, the proton decay to $K^+\bar{\nu}$ and the following decay of the Kaon. Also the fast ^{214}Bi - β - and ^{214}Po - α -coincidences can be used to tag radioactivity-induced background due to the very fast time response of the liquid scintillator. In addition, pulse shape analysis can be performed to distinguish signals produced by beta decays and gamma or neutrino electron recoils from α -particles and protons. Heavier particles deposit their energy over a shorter distance compared to light particles, according to the Bethe-Bloch law [58].

With an efficient light production of the organic scintillator of approximately 10^4 photons per 1 MeV and the previous mentioned background suppression along with the radiopurity requirements, a detector threshold of a few hundreds of keV and an energy resolution of a few percent in the low energy region is feasible using large volume detectors. This is far better than the energy resolution of water Cherenkov detectors and allows the observation of low-energy solar neutrinos.

2.2 Neutrino Interactions at Low Energies

As already mentioned the neutrino interacts mainly with the electrons but also with the other constituents of the liquid scintillator. Aside from the neutrinos the educts of this reaction are electrons, free protons of the contained Hydrogen and protons or neutrons that are bound in the Carbon nuclei of the liquid scintillator. The interaction itself can be CC or NC reactions influencing the cross section of the different neutrino flavour. The single interactions will be described in detail in this chapter.

2.2.1 Elastic Scattering

The main reaction channel for low-energy neutrinos detected in liquid scintillators is the neutrino – electron scattering. All neutrino flavors are able to scatter off electrons via the NC. Only the electron neutrino has the possibility to scatter off the electron via CC

reactions to the same final state. As a result, the cross section of the electron neutrino scattering off an electron is enlarged and, therefore, is the most prominent reaction channel of all for low neutrino energies. An overview of all possible Compton like scattering reaction and their different cross sections is presented in table 2.1.

As can be seen, there is no threshold for the first reactions because all involved particles

| Rection channel | Current | Threshold [MeV] | Cross section [10^{-44} cm^2] |
|--|---------|-----------------|---|
| $e^-(\nu_e, \nu_e)e^-$ | NC/CC | - | $0.95 E_\nu$ |
| $e^-(\bar{\nu}_e, \bar{\nu}_e)e^-$ | NC/CC | - | $0.40 E_\nu$ |
| $e^-(\nu_x, \nu_x)e^-$ | NC | - | $0.16 E_\nu$ |
| $e^-(\bar{\nu}_x, \bar{\nu}_x)e^-$ | NC | - | $0.13 E_\nu$ |
| $p(\nu_\mu, \nu_\mu)p$ | NC | | $0.32 E_\nu^2$ |
| $p(\bar{\nu}_e, e^+)n$ | CC | 1.8 | $9.5 (E_\nu - 1.29)^2$ |
| $^{12}\text{C}(\nu_e, e^-)^{12}\text{N}$ | CC | 17.34 | 3.6 @ 18 MeV |
| $^{12}\text{C}(\bar{\nu}_e, e^+)^{12}\text{B}$ | CC | 13.37 | 32.7 @ 18 MeV |
| $^{12}\text{C}(\nu_a, \nu_a)^{12}\text{C}^*$ | NC | | 10.6 @ 18 MeV |
| $^{12}\text{C}(\bar{\nu}_a, \bar{\nu}_a)^{12}\text{C}^*$ | NC | 15.11 | 9.9 @ 18 MeV |
| $^{13}\text{C}(\nu_e, e^-)^{13}\text{N}$ | CC | 2.22 | 85.7 @ $\langle E_{\nu_{8B}} \rangle$ |
| $^{13}\text{C}(\nu_a, \nu_a)^{13}\text{C}^*$ | NC | 3.68 | 11.5 @ $\langle E_{\nu_{8B}} \rangle$ |

Table 2.1: Low-energy neutrino reaction channels in liquid scintillators with their associated weak current, energy threshold and the energy dependent cross section. ν_a and $\bar{\nu}_a$ stand for all neutrino flavours, whereas the flavours μ and τ are summarized by the index x . Values contained in this table are taken from [21] for the neutrino – electron scattering and the ^{12}C reactions, from [59] for the proton scattering, and from [60] for the ^{13}C channels. The cross section values are presented without radiation corrections.

remain unchanged. The detection threshold is therefore limited by the electronics or the radioactive background. The thresholds of the other channels derive from the energy of the exited and transformed final state, respectively.

Of course, the neutrino is not just able to scatter elastically off electrons. There is also the possibility to scatter off protons of the scintillator. This process is especially interesting for supernova neutrino detection as can be seen in [61]. The vanishingly low threshold of the electron recoil corresponds to a threshold in the MeV energy range for proton recoil deriving from the high proton mass and the associated low light output.

An effect that has to be taken into account for all scattering processes is the quenching of the scintillation light. It has influence on the energy reconstruction and, therefore, is crucial to be exactly known in order to identify or understand the observed signal in a correct way. The influence and the measurement of the quenching effect will be explained in detail in section 3.4 and chapter 4.

2.2.2 Inverse Beta Decay

The best channel for electron antineutrino detection is the inverse beta decay. This capture of an electron antineutrino on a proton has a large cross section even for low energies and offers the opportunity to use a coincidence signal detection to identify the event. The first signal is given by the ionization energy deposition and annihilation of the positron in the liquid scintillator. This signal is detected by the PMTs and defines the time and charge information of the hit. Due to the spatial information, the generated free neutron can be observed and detected when captured on a free proton 180 μs - 250 μs later, releasing a gamma quantum with an energy of 2.2 MeV, the deuteron binding energy. The neutron itself can be vetoed due to the spatial and time coincidence to the positron, whereas the positron itself can be clearly identified via the coincidence measurement of the neutron capture. A good signal identification and background suppression is possible in this way. While the neutrino – electron scattering is the main detection process for solar neutrinos especially in the low-energy regime, the inverse beta decay is the best detection channel for the DSNB and geo-neutrinos. Because water Cherenkov detectors typically have an energy threshold too high to use this detection mechanism, an additive has to be dissolved in the water to enhance the neutron signal. A possible option would be Gadolinium, generating an 8 MeV gamma signal instead of the 2.2 MeV signal. This option was discussed for the DSNB detection in SuperKamiokande [42]. But it is also a possibility for liquid scintillator detectors to focus on the inverse beta decay as it is a main reaction channel for reactor-electron-antineutrino detection, as for example performed by the Double-Chooz experiment [62].

2.2.3 CC and NC Interactions with Carbon

The last reaction channel to mention and also listed in table 2.1 is the interaction of neutrinos with Carbon. First, the three possible reactions with ^{12}C shall be mentioned. With a threshold $\gtrsim 14$ MeV, however, these reactions cannot be used for the solar neutrino measurement. But they offer a good opportunity for higher-energetic neutrinos, like SN neutrinos.

When the neutrino and the antineutrino interacts via the CC with a ^{12}C nucleus, the generated products decay a few milliseconds after the initial signal of the e^\pm under emission of another e^\pm , respectively. This coincidence in time and space can once more be used to identify the signal of interest. However, it is difficult to distinguish experimentally between the neutrino and the antineutrino signal because of the very similar event signature. The NC reactions are sensitive to all neutrino flavours. As it is an inelastic scattering off ^{12}C , the only signal observed is the de-excitation of the Carbon nucleus, releasing a gamma particle with an energy of 15.11 MeV.

The last reaction for neutrinos to be mentioned here is the interaction with ^{13}C . Because of the low threshold of both, CC and NC channel, this detection mechanism is not only interesting for SN neutrino measurement but also plays an important role for the solar ^8B neutrino measurement. More interesting than the excitation of the ^{13}C is the reaction to

^{13}N and its subsequent decay. Though the abundance of ^{13}C in a liquid scintillator is low² and the ^{13}N decay is 862.6 seconds [60] after the initial signal, the coincidence provides a sufficient signal for background identification. The implication of this reaction channel to the neutrino detector Borexino can be found in [60].

2.3 Borexino Detector Design

A state-of-the-art liquid scintillator neutrino detector is the Borexino detector [17]. It is located in the underground laboratories of the Laboratori Nazionali del Gran Sasso (LNGS), INFN Italy. With an overburden of approximately 3500 m.w.e this site offers enough shielding for low-energy neutrino detection. The assembling of the detector was finished 2004, data taking with a fully serviceable detector started May, 15th 2007 and is still continuing. A schematic view of the detector is shown in figure 2.1.

The detector has a typical design for liquid scintillator detectors. It comprises several interleaved spheres. The outermost volume is a water tank (WT) called Outer Detector (OD). It contains a stainless steel sphere (SSS) including the outer and inner vessel (OV/IV). All parts contained in the SSS are forming the Inner Detector (ID). Underneath the detector carbon plates serve as additional shielding against radioactivity emitted by the floor. The main parts will be described in detail in the following.

The inner vessel defines the innermost volume of the detector. It is composed of high-purity nylon with a thickness of 125 μm and forms a sphere with 8.5 m diameter. It is designed impermeable for scintillator as it separates the active scintillator volume from the buffer liquid. In addition, it shields the scintillator and prevents α -, β -particle and isotope diffusion. Nylon strings keep the sphere in the correct form and position. The volume inside can be accessed by the chimney on top of the sphere. For detailed information see [63].

The heart of the detector is formed by the liquid scintillator. It is filled in the IV. The mixture is composed of pseudocumene (PC: 1,2,4-trimethylbenzene, $C_6H_3(CH_3)_3$) and PPO (2,5 diphenyloxazole, $C_{15}H_{11}NO$). PC serves as the sensitive material for neutrino interaction. Because the molecules emit in the UV-light regime, the light output has to be shifted to lower energies that are detectable at the PMTs. The dissolved fluor PPO is added with a concentration of $c = 1.5 \text{ g/l}$ and acts as the needed wavelength shifter. The total amount of liquid contained in the IV is 270 t. In order to have a better shielding against external gammas resulting in a better background suppression, only the innermost 100 t serve as fiducial volume³ for the analysis.

The already mentioned buffer liquid is contained in the SSS outside the IV. Its purpose is to shield the sensitive volume of the detector against external radiation. In order to keep the IV from floating, the density of the buffer liquid has to be similar to that of the liquid scintillator. Hence, it was decided to use pure PC. To keep it from scintillating by itself, DMP (dimethylphthalate, $C_6H_4(COOCH_3)_2$) was added in a concentration of $c = 5 \text{ g/l}$ as

²natural isotopic abundance $I = 1.07\%$ [60]

³the reduction is performed via a software-cut during data analysis

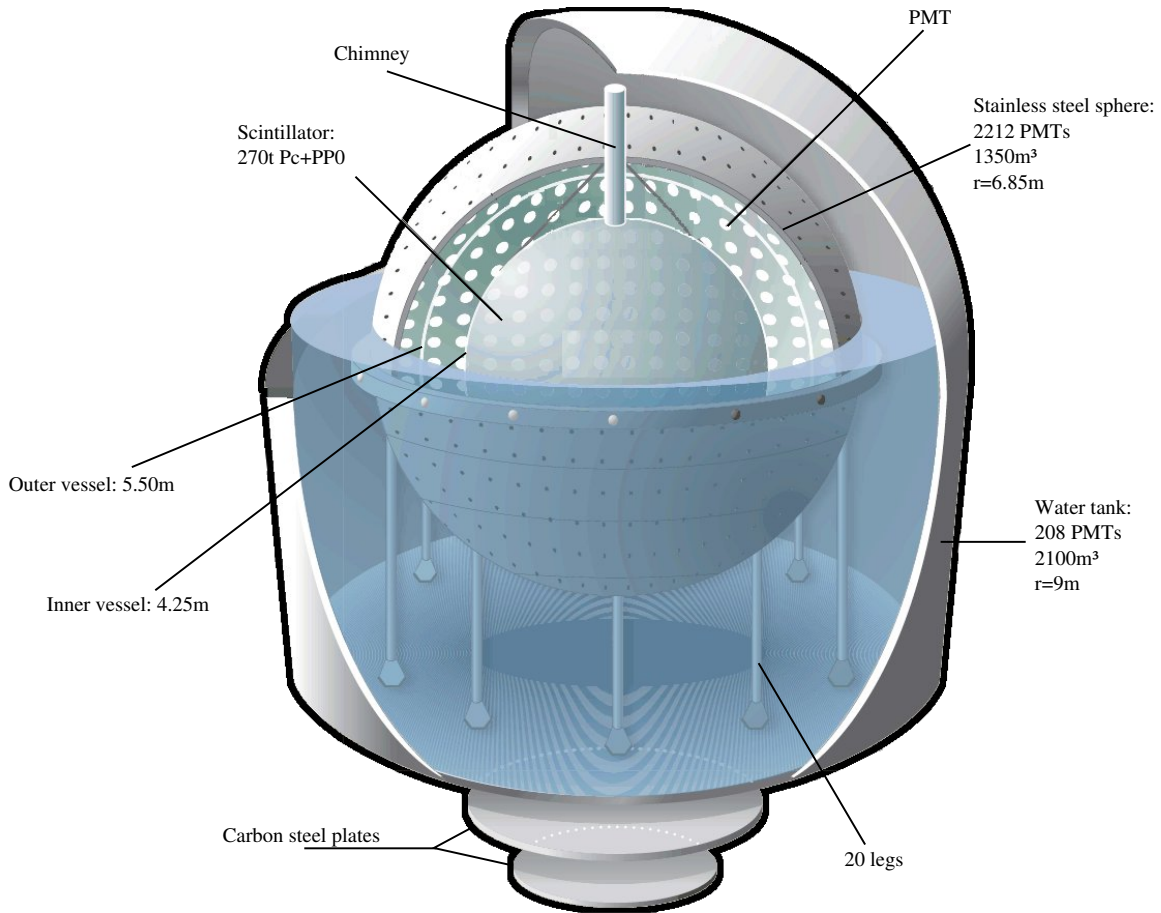


Figure 2.1: The Borexino detector design as an example for a state-of-the-art liquid scintillator detector. The scintillator contained in the Inner Vessel is shielded by several layers of buffer liquid and water. It is monitored by PMTs mounted to the Stainless Steel Sphere. More details are explained within the text.

quencher material. The total amount of buffer liquid is 1040 t.

The outer vessel is also made of nylon and has a diameter of 11 m and again a thickness of 125 μm . It is set up inside the buffer liquid and avoids radon entering to the innermost detector volume. Nylon stripes are used to fix it at top and bottom to the SSS. As for the IV, high radiopurity requirements were set during planing and production phase [63].

The stainless steel sphere separates the detector into ID and OD. It has a diameter of 13.7 m and a thickness of approximately 10 mm. The structure is supported by 20 steel legs. For the ID the SSS is equipped with 2212 PMTs, monitoring the innermost volume, the IV. In order to enlarge the light output and to focus on the IV, 1838 PMTs are equipped with light-concentrators, so-called Winston cones. These are made of highly reflective aluminium with a high radiopurity. Together with the unmodified 374 PMTs, the configuration can be used to distinguish between muon-like and neutrino-like events

[64]. For calibration purposes, a laser signal can be transmitted via optical fibers to each PMT.

The water tank acts as OD. It is formed by a steel dome with a base of 18 m diameter and a height of 17 m. It is filled with 2400 t of ultra-pure water as detector material. 208 PMTs, mounted mainly to the outside of the upper half of the SSS and to the bottom of the WT, monitor the OD volume. Some PMTs are mounted on the lower half of the SSS and on the lower inner walls of the WT. In this design the WT forms a water Cherenkov detector that is used as an active muon veto. In order to enhance the detection efficiency, the inner walls of the dome and the outside of the SSS are covered with highly reflective white Tyvek sheets. Compared to the calibration system of the ID, the OD uses a LED and optical fiber system.

Chapter 3

Liquid Scintillator

The liquid scintillator volume is the heart of many modern neutrino detectors. The light signal observed by the PMTs is strongly dependent on the properties of the used scintillator. First, it is crucial to choose the right scintillator for the respective detector layouts. Second, in order to understand and to interpret the obtained signals in a correct way, the scintillator properties have to be known exactly. Often the different requirements are dependent on the energy window under examination. The most important characteristics of organic liquid scintillators will be explained in this chapter.

3.1 Theoretical Properties

Organic liquid scintillators consist of hydrocarbon molecules containing benzene-ring structures. There are several bonds formed by the four available valence electrons of the carbon. The interesting ones for scintillation are the so called π -bonds with their electrons forming π -orbitals. They are not as strongly bound as the σ -bonds and can therefore be excited more easily. Depending on the de-excitation time, fluorescence ($\tau \sim \text{ns}$) and phosphorescence ($\tau \sim \text{ms}$) are distinguished. For a better explanation a so called Jabłoński diagram¹ is shown in figure 3.1. As can be seen, a triplet or singlet state can be formed by the excited scintillator molecules depending on the spin orientation of the π -electrons. The electronic levels S_i , $i = 1, 2, 3, \dots$ are separated by 2 - 4.5 eV, while the vibrational levels S_{ij} have a gap between each other of approximately 0.1 eV. Due to absorption, the singlet state can be excited to higher energy levels. The molecule loses some of this energy gained due to collision with neighboring molecules including vibrational relaxation until it reaches the state S_1 . These processes happen quite fast (10^{-12} s). The energy of vibrational relaxation is released in form of heat. The state S_1 de-excites then to the ground state S_0 or one of its vibrationally excited levels. The energy is released in form of fluorescence photons. The direct excitation of triplet states $S_0 \rightarrow T_1$ needs a spin flip which is forbidden due to selection rules for electromagnetic radiation. Therefore, the higher energetic states are populated by intersystem crossing or by recombination of ionized molecules with electrons.

¹named after A. Jabłoński who invented the diagram in 1935 [65]

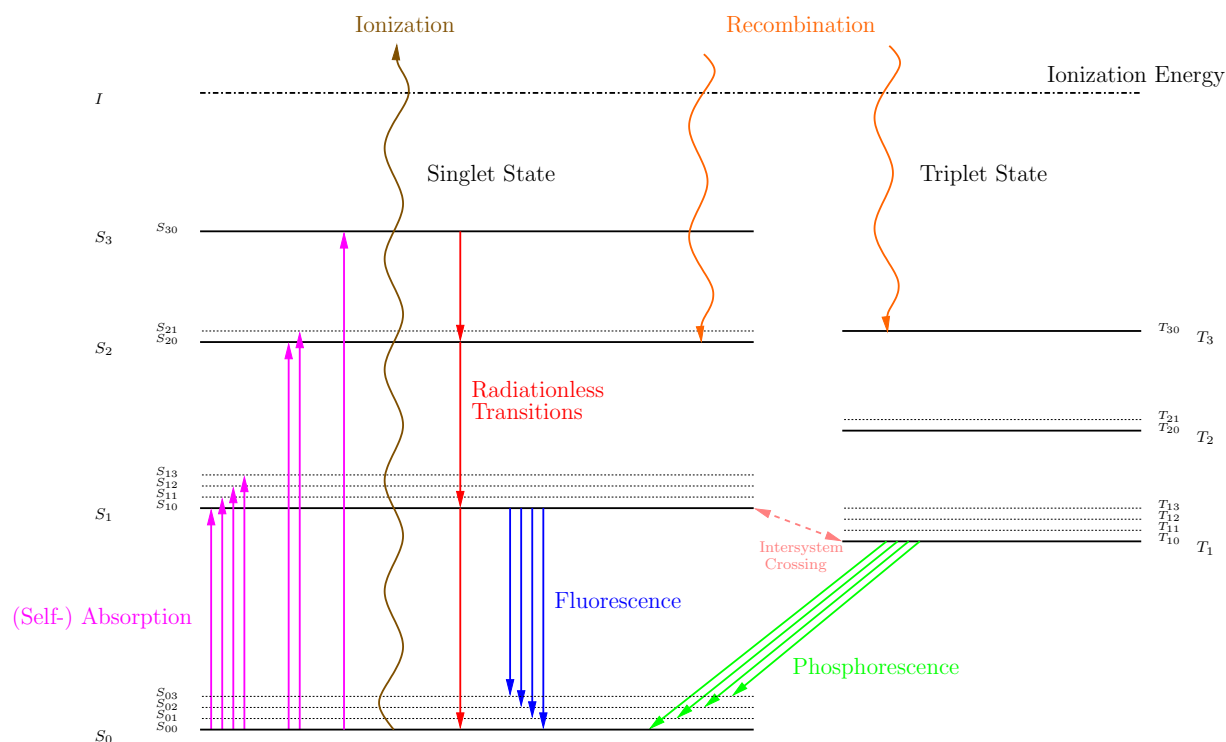


Figure 3.1: π -electron energy levels of liquid scintillator molecules. S_0 defines the ground state, S_i and T_i , $i = 1, 2, 3, \dots$ are the energy levels of the singlet and triplet state, respectively. The vibrational states of each energetic level are denoted by S_{ij} . The possible absorption and de-excitation processes are marked in colors: pink = absorption, red = radiationless transitions due to e.g. collisions, blue = fluorescence, green = phosphorescence. Ionization (brown) and recombination (orange) is possible for all energy levels. Intersystem crossing (pink) between singlet and triplet energy levels can occur.

Because of the likewise forbidden de-excitation from $T_1 \rightarrow S_0$ this process has a time scale of ms and, therefore, generates phosphorescence.

The emitted light can, of course, be directly reabsorbed by a scintillator molecule. This self-absorption is an unwanted process, as energy losses might occur as well as the spatial and timing information of a particle hit might be adulterated. To avoid this, fluor is added. This wavelength-shifter absorbs the emitted light of the scintillator and emits it at a different wavelength, not absorbable by the scintillator anymore. Hence, the solvent becomes transparent for the produced light and the information of hit-time and energy is conserved. A typical concentration for fluor is in the region of a few g/l, as for higher concentrations self-absorption of the fluor exists. In addition, a higher light collection efficiency for the PMTs is a spin-off product. For instance, in Borexino PC is used as solvent and PPO in a concentration of 1.5 g/l as fluor.

For a detailed view on the theory and properties of organic liquid scintillators see [66][67].

3.2 Attenuation Length

A crucial property of liquid scintillators used in neutrino detectors is the ability of light to traverse through the solvent and fluor. As future neutrino detectors aim for an increase of their active detection volume, the photons produced must still be able to reach the PMTs undisturbedly. All interferences would have an impact on the energy and spatial reconstruction of the event. Two interactions of the traveling photon must be taken into account: absorption and scattering. The intensity of the effects is described by the related mean free path lengths of the photon before interaction, the absorption length λ_{abs} and the scattering length λ_{sct} . The light intensity I for a covered distance x is exponentially linked to these values:

$$I(x) = I_0 \cdot \exp\left(-\frac{x}{\lambda_{\text{abs}}}\right) \cdot \exp\left(-\frac{x}{\lambda_{\text{sct}}}\right) = I_0 \cdot \exp\left(-\frac{x}{\lambda_{\text{att}}}\right) \quad (3.1)$$

The combination of scattering and absorption is the attenuation effect, and thus λ_{att} is declared as the attenuation length. For this reason a direct relation between the respective lengths exists:

$$\frac{1}{\lambda_{\text{att}}} = \frac{1}{\lambda_{\text{abs}}} + \frac{1}{\lambda_{\text{sct}}} \quad (3.2)$$

Absorption takes place on any component available in the scintillator or buffer liquid. The energy of the photon can be transformed into heat during the interaction and thereby is lost for creating a signal at the PMTs. But also absorption and reemission on a scintillator molecule may occur. In these two cases, also counted to the scatter effect, and in the case of scattering itself, the signal is not lost completely, but to use with care. The photon may transfer just a fraction of its energy and change its direction. All this makes reconstruction a difficult mission. Besides absorption and reemission, scattering mainly exists in form of Rayleigh- and Mie-scattering. Due to the problem of distinguishing the different scattering mechanisms in experiments, the process can only be divided into isotropic and anisotropic scattering, and the corresponding λ_{is} and λ_{an} (see [68]). Equation 3.2 than transfers into

$$\frac{1}{\lambda_{\text{att}}} = \frac{1}{\lambda_{\text{abs}}} + \frac{1}{\lambda_{\text{is}}} + \frac{1}{\lambda_{\text{an}}}. \quad (3.3)$$

There are several works that address the topic of the attenuation length and use different approaches [59][68][69][70][71][72]. A collection of different parameters determined in these works is given in table 3.1.

3.3 Light Yield

A further important characteristic of liquid scintillators is the light yield. It is a measure of the efficiency of the light production. It describes the number of photons emitted per amount of energy deposited in the scintillator. It is therefore linked directly to the energy

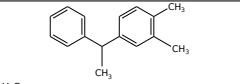
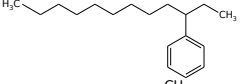
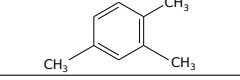
| LS | chemical structure | λ [nm] | λ_{is} [m] | λ_{an} [m] | λ_{scat} | λ_{att} [m] |
|-----|---|----------------|---------------------------|---------------------------|-------------------------|----------------------------|
| PXE |  | 430 | 40.0 ± 3.9 | 51 ± 13 | $22.3 \pm 2.7 \pm 1.6$ | — |
| LAB |  | 430 | 66.3 ± 5.7 | 40.0 ± 4.6 | $25.0 \pm 1.9 \pm 1.6$ | 9.09 ± 0.82 |
| PC |  | 430 | 13.0 ± 0.9 | 19.3 ± 3.3 | $7.8 \pm 0.6 \pm 0.6$ | — |

Table 3.1: Attenuation and scattering lengths of different liquid scintillators (LS) together with their respective chemical structure. λ_{is} represents the isotropic, λ_{an} the anisotropic, λ_{scat} the resulting total scattering length, and λ_{att} the attenuation length. The measurements were performed for the wavelength λ . Data taken from [68][69].

resolution of the detector, as the resolution improves significantly with the number of photons detected. Together with the collection efficiency of the PMTs the light yield of the whole detector can be estimated. In order to gain a high light yield it is essential that the light can propagate unaffectedly towards the PMTs. Therefore, this parameter is strongly dependent on the used solvent and fluor. The light yield is growing along with the used fluor concentration, until saturation of the light yield is reached. The influence of the fluor concentration is shown in table 3.2.

The challenge for an experiment to measure the absolute light yield is the light detection itself. A 4π detector is required with an exact knowledge of the light collection efficiency. Therefore, relative light yield measurements are often performed due to the better feasibility. The results achieved are compared to a calibration measurement based on known light yields determined by other experiments like the CTF [73][74] and Borexino [75][76]. An example of a relative measurement will be presented in section 4.4. Other works treating this subject are for example [69][77]. A collection of values for some liquid scintillator compositions is presented in table 3.3. The measured light yields show a behaviour that strongly depends on the observed scintillator and fluor samples.

Of course, there are effects that interfere with the light production or propagation and, hence, effect the total light yield of the detector. Some effects like absorption and scattering have already been discussed in section 3.2. But there are also minor effects that have to be taken into account, like quenching that will be described in the next section.

3.4 Quenching Effect

As previously mentioned, the light output of a liquid scintillator depends on many different variables. In any case it is linked to the incident particle type, to the energy and the resulting ionization. Due to the ionization an effect occurs, mainly for low-energy electrons or heavier particles that is called ionization quenching. A particle traveling through the scintillator ionizes molecules on its path. These 'damaged' molecules are responsible for

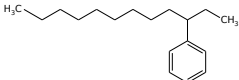
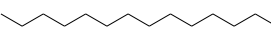
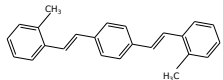
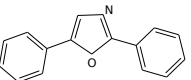
| LAB  | Tetradecan  | bisMSB  | PPO  | Light yield [$\frac{\text{ph}}{\text{keV}}$] |
|--|---|--|--|---|
| 37.5 % vol. | 62.5 % vol. | 20 mg/l | 0 g/l | 1.7±0.2 |
| 37.5 % vol. | 62.5 % vol. | 20 mg/l | 1.0 g/l | 7.4±0.8 |
| 37.5 % vol. | 62.5 % vol. | 20 mg/l | 1.5 g/l | 8.5±0.9 |
| 37.5 % vol. | 62.5 % vol. | 20 mg/l | 2.0 g/l | 9.2±1.0 |
| 37.5 % vol. | 62.5 % vol. | 20 mg/l | 2.5 g/l | 9.6±1.1 |
| 37.5 % vol. | 62.5 % vol. | 20 mg/l | 3.0 g/l | 9.8±1.1 |
| 37.5 % vol. | 62.5 % vol. | 20 mg/l | 3.5 g/l | 10.0±1.1 |
| 37.5 % vol. | 62.5 % vol. | 20 mg/l | 4.0 g/l | 10.2±1.2 |

Table 3.2: Influence of the fluor concentration on the light yield (in photons per keV). The light yield is growing along with the used fluor concentration, until saturation of the light yield is reached. Data taken from [69].

| Scintillator composition | Light yield relative to PXE + 2 g/l PPO |
|--------------------------|---|
| PXE + PPO | 100.0% ± 3.3% (syst.) ± 0.1% (stat.) |
| LAB + PPO | 103.4% ± 3.1% (syst.) ± 0.2% (stat.) |
| PXE + PMP | 79.1% ± 2.8% (syst.) ± 0.3% (stat.) |
| LAB + PMP | 83.9% ± 2.8% (syst.) ± 0.2% (stat.) |
| PXE + PPO + bisMSB | 102.0% ± 3.0% (syst.) ± 0.3% (stat.) |
| LAB + PPO + bisMSB | 99.7% ± 3.0% (syst.) ± 0.2% (stat.) |

Table 3.3: Light yield of different scintillators relative to a reference scintillator (PXE + 2 g/l PPO). The measured behaviour shows a strong dependency on the different observed samples, especially on the additive. Data taken from [77].

the quenching and lower the light yield of the scintillator. The larger the energy deposition per unit path length (dE/dx) the higher is the ionization and for this reason the quenching. This effect was first observed for crystals but later was extended also to liquid scintillators [78].

Still today parameters describing this quenching for different materials are not well known. For liquid scintillator experiments [79] it is of great interest to know these parameters to understand the exact detector response, as decoding small energy differences in the signals detected play an important role.

3.4.1 The Birks Factor

In this work the focus is on the ionization quenching effect for electrons. An empirical model to explain the effect is given by the Birks formula [78]

$$\frac{dL}{dx} = \frac{L_0 \frac{dE}{dx}}{1 + kB \frac{dE}{dx}}. \quad (3.4)$$

Here, dL/dx is the number of photons emitted per unit path length. The specific energy loss is given by $L_0 dE/dx$, at which L_0 is a constant that defines the absolute scintillation efficiency. The material specific Birks factor kB links the densities of the ionization and damaging centers to the energy deposition per unit path length dE/dx . This dE/dx can be described in general via the energy-dependent Bethe-Bloch formula [21]

$$-\frac{dE}{dx} = \frac{4\pi Z^2 \alpha^2 n_e}{\beta^2 m_e} \left[\ln \frac{2\beta^2 m_e}{\bar{I}(1-\beta^2)} - \beta^2 \right]. \quad (3.5)$$

The velocity of the charged particle is given by β , the electron number density of the scintillator is n_e . With a value of $\bar{I} = 13.5$ eV the mean ionization energy is defined. α is the fine structure constant and Z the proton number of the scintillator. For the observation of electron quenching corrections to equation 3.5 have to be applied, taking into account exchange interactions, and energy and density corrections of the medium. With the indistinguishability of electrons passing through the matter and the ones contained within it, this leads to [80][81]

$$\begin{aligned} \frac{dE}{dx} = & \frac{2\pi r_e^2 n_e E_0}{1 - \left(\frac{E_0}{T+E_0}\right)^2} \left[\ln \left(2 \left(\frac{T+E_0}{E_0} + 1 \right) \frac{E_0^2}{I^2} \right) + \left(\frac{E_0}{T+E_0} \right)^2 + \ln \left(\left(\frac{T+E_0}{E_0} - 1 \right)^2 \right) + \right. \\ & \left. + \left(\frac{T+E_0}{E_0} - 1 \right)^2 \frac{1}{8} \left(\frac{E_0}{T+E_0} \right)^2 - \frac{2 \left(\frac{T+E_0}{E_0} - 1 \right) + 1}{\left(\frac{T+E_0}{E_0} \right)^2} \ln(2) \right] \end{aligned} \quad (3.6)$$

with the kinetic energy of the electron T . E_0 is the electron rest energy of 511 keV. n_e is again the electron number density of the scintillator and r_e is the classical electron radius. The mean ionization energy I can be calculated according to [80] to

$$I = \exp \frac{\sum_j w_j \frac{Z_j}{A_j} \ln(I_j)}{\sum_j w_j \frac{Z_j}{A_j}}, \quad (3.7)$$

where the index j represents the j th element of the compound, w_j is the respective fraction by weight, and Z_j and A_j represent the respective atomic number and atomic weight.

A determination of the Birks factor kB and, therefore, a classification for liquid scintillators is possible in experiments. An example of a measurement, including the evaluation of the gained data, is demonstrated in chapter 4. An other approach using Germanium detectors can be found in [79].

Chapter 4

Quenching Experiment

As many existing neutrino experiments use different scintillators compared to each other, it is necessary to determine the respective quenching factor. For some experiments like Double-Chooz, measurements have been done to determine the previously mentioned Birks factor [79]. In this chapter, an experiment to measure the scintillators used in the Borexino and the LENA detector is presented. First, the used experimental method is described followed by the description of the scintillators investigated. The experimental setup itself is explained in section 4.2. Test measurements for the Double-Chooz detector and the following Birks factor measurement are reported in section 4.4 and 4.5, respectively. After a discussion of uncertainties (section 4.6) the final results of the measured Birks factors are presented in section 4.7.

4.1 Experimental Method

Quenching is a measure for the amount of light produced by a certain charged particle in a liquid scintillator in relation to its energy deposition. Hence, it is essential to determine the input and the output energy of a liquid scintillator. The output energy can simply be measured by a PMT. The input energy, however, can only be determined indirect. There are several different methods possible to do so. One possibility using a germanium detector can be read in [79].

For the experiment introduced in the present thesis, the properties of Compton scattering, see figure 4.1, are used. Using a radioactive source with a well-known energy and a reference detector, the deposited energy within the scintillator can be determined. The energy of the scattering photon, E'_{photon} , is dependent on the scattering angle θ and calculates to [58]

$$E'_{\text{photon}} = \frac{E}{1 + \frac{E}{m_e c^2} (1 - \cos \theta)}, \quad (4.1)$$

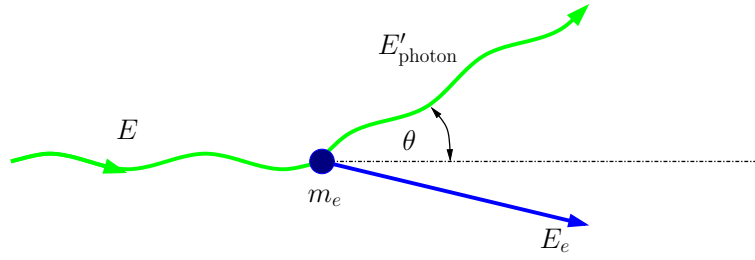


Figure 4.1: Compton scattering of a photon with initial energy E off an electron with the electron mass m_e . E'_{photon} is the energy of the scattering photon, E_e is the energy of the recoil electron. The scattering angle is given by θ .

where m_e denotes the electron mass and c the speed of light in vacuum. E is the initial energy of the photon. Thus, the energy of the recoil electron, E_e , is

$$E_e = E - E'_{\text{photon}} = \frac{\frac{E^2}{m_e c^2} (1 - \cos \theta)}{1 + \frac{E}{m_e c^2} (1 - \cos \theta)}. \quad (4.2)$$

The reference detector shall detect the scattering photon. Setting up a coincidence circuit between this second detector and the detector observing the liquid scintillator, the energy deposited in the sample can be calculated. The only necessity is the knowledge of the scattering angle. A schematic setup of the experiment explained in section 4.2 is depicted in figure 4.2 illustrating the previous mentioned coincidence detection mechanism. Because of the movable radioactive source, this angle can be modified. Therefore different deposited energies in the liquid scintillator can be investigated. An accurate coincidence time setup is essential to suppress unwanted background. The expected recorded spectrum of the scintillator detector is depicted in figure 4.3. The red line represents still persisting background, following an exponential distribution. The detected Compton energy of the scattering electron is illustrated by the dashed blue Gaussian distribution. The overlay of both, and therefore the measured signal, is given by the black curve. Using the different energies and the respective light output of the liquid scintillator, the Birks parameter and the quenching can be determined, respectively.

4.2 Experimental Setup

This section gives an overview of the setup and the electronics used in the experiment performed in the context of the present thesis. First, the mechanical structure is explained followed by an introduction of the DAQ (data acquisition) system used.

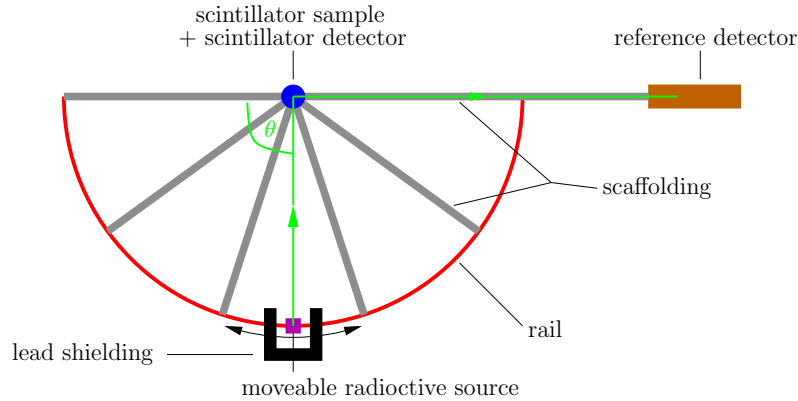


Figure 4.2: Schematic view of the coincidence experiment performed in the present thesis to determine the Birk's factor. Blue represents the detector and the investigated scintillator. Brown is the reference/coincidence detector. The movable radioactive source (magenta) is positioned on a rail (red) with angle marks and therefore allows the observation of different deposited energies. The source is surrounded partially by a lead shielding (black). θ is the scattering angle, the green line represents the track of the in coincidence detected gamma particle. The different setup parts are attached to each other via the scaffolding (grey).

4.2.1 Measurement Setup

As already mentioned in section 4.1, the experiment performed in the context of this thesis is a coincidence measurement. A picture of the setup is shown in figure 4.4. The different components are highlighted. Marked in red is the rail equipped with angle marks. It forms a semi-circle of 51 cm radius, hosting the source holder, shown in magenta. The point-like radioactive source used, consists of ^{137}Cs with an activity of 10^8 Bq. The gamma quanta released have an energy of 662 keV. This results in a maximum deposited energy of 477 keV for backscattering in the scintillator detector due to Compton scattering. For shielding towards the experimenter a movable lead shielding was implemented to cover the source. In addition it prevents the emitted gamma quanta to hit the reference detector.

The green mark denotes the reference detector. It is formed by a PMT and a 10 cm long plastic scintillator BC-408 with a diameter of 1". Its sensitivity to gamma rays reaches down to energies of less than 100 keV. The fast rise (≈ 1 ns) and decay time (≈ 2.1 ns) allow a an easy setup of the coincidence timing. To enhance the light detection probability in the PMT, the plastic scintillator was coated with a reflective paint. Its wavelength of maximal emission is 425 nm which is in the same range as the light output of the liquid scintillator mixtures used. For that reason, the PMT used for the reference detector is of the same type as the one used for the liquid scintillator detector.

The PMTs used are of type 9111B from Electron Tubes Ltd., now distributed by ET Enterprises Limited. Their diameter is 1" and they have a spectral range of 280 nm – 630 nm. Therefore, they are very suitable for the observed wavelength. The PMT used for the plastic scintillator is powered by 810 V, whereas the more important one for the liquid

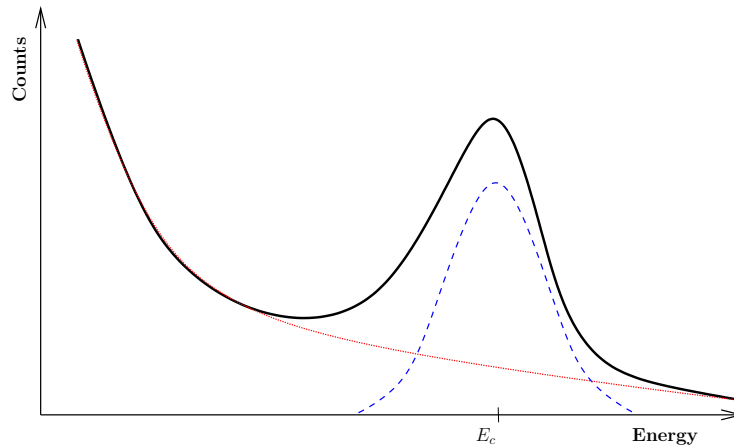


Figure 4.3: The black curve represents the expected signal as measured by scintillator detector in the coincidence Compton scattering experiment. It consists of the still persisting exponential background (red line) and the Compton energy peak (dashed blue line).

scintillator is powered by 1260 V.

The distance between the centers of the two detectors adds up to 60 cm. Designing the setup, it was paid attention to the detail that the radioactive source and the two detectors are all located in one and the same plane for all the different angles. This allows an exact determination of the deposited energy.

The most important part in figure 4.4 is marked in blue. It is the primary detector placed in the center of the rail. The scintillator containment, the tin, visible on top of the PMT in picture 4.4, is an early one. Different designs were studied to find an airtight, practicable and high reflective tin in order to have a low disturbing background rate due to unwanted scattering and a high reproducibility when replacing the tin after a refill. A schematic view of the final version that is used for the measurement is depicted in figure 4.5. It is made of bare aluminium for a high reflectivity. The walls are kept thin to avoid unwanted gamma scattering in the shell. To reduce unwanted multiple scattering inside the scintillator and to define an exact scattering angle, the cell containing the liquid is of small volume: 1" diameter (equal to the size of the PMT used) and a height of approximately 4 cm form a total detector volume of approximately 20 ml. It is sealed with a fused quartz glass at the bottom supplying good transmission properties at the emitted wavelength of ~ 400 nm. The glass is kept in place by deepenings in the main body and in the cover plate that is screwed to the main body. The clogging has direct contact to the scintillator and, therefore, must not react with it. For that reason polytetrafluoroethylene (teflon) is chosen as material. The tin is filled through a hole on top that is sealed by a screw afterwards. To keep a certain distance between the PMT and the fused quartz glass, to guarantee reproducibility, a spacer is integrated into the cover plate. A photograph is shown in figure 4.6.

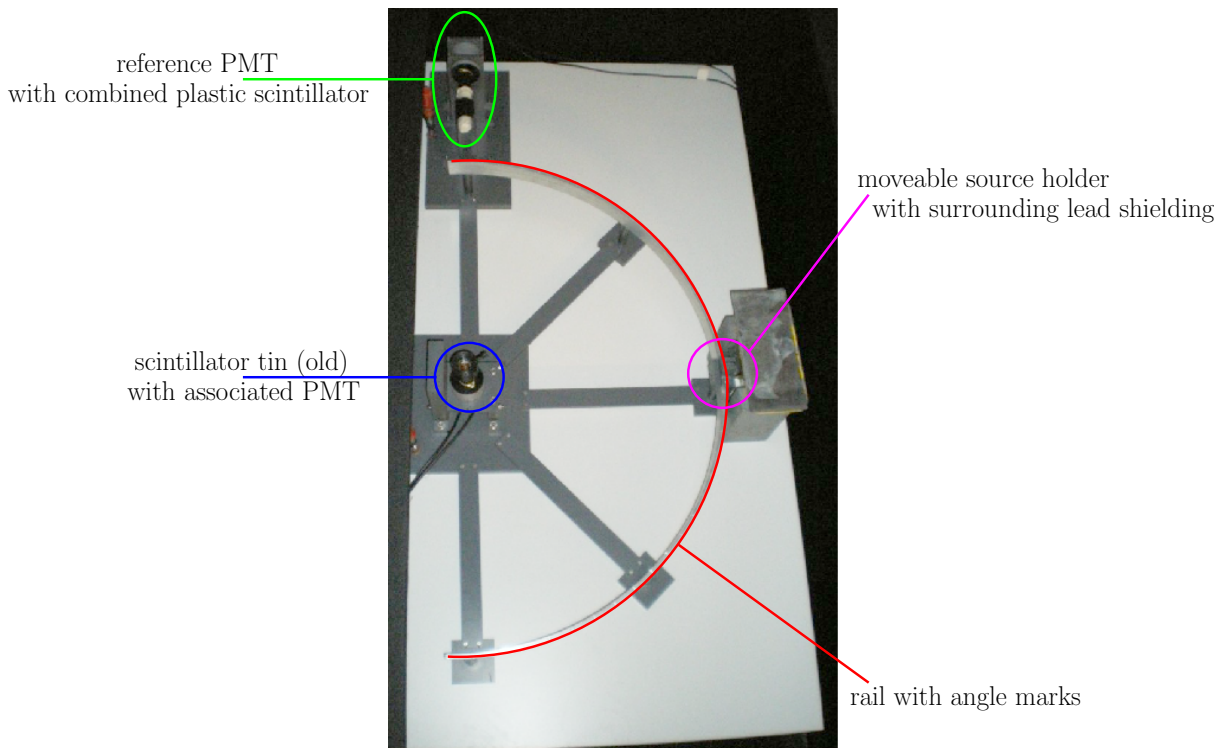


Figure 4.4: Picture of the quenching experiment. Visible is the rail hosting the source holder that is surrounded by a lead shielding. As well, the tin and its PMT are depicted. The reference detector consisting of a plastic scintillator and a PMT is marked. The scintillator containment, the tin, included here into the setup was an early version. The final one can be seen in figures 4.5 and 4.6.

4.2.2 Electronics and DAQ

After having discussed the setup of the experiment, the electronics used shall be described. A schematic overview is depicted in figure 4.7. The signals generated by the two scintillators are detected by the respective PMT, mentioned in the previous section. Transmitting the signals towards the read-out electronics, time differences due to different timing of liquid and plastic scintillator and different cable lengths, are nullified by a delay-box. The signal is then amplified by a CAEN Mod. N979 NIM-module and forwarded to a Fan In/Fan Out of type CAEN Mod. N625. Here, the signal is split. One part is going directly to the recorder, which will be explained later within this section. The other part is fed to the Leading Edge Discriminator (CAEN Mod. N840). As the signals generated by the PMTs are not completely identical, different settings have to be applied for the discriminator. For the tin signal a threshold of 60 mV is set, compared to 70 mV threshold for the plastic scintillator. A logical pulse of 35 ms width is generated and send to the coincidence module (CAEN Quad Coincidence Logic Unit Mod. N455). In case a signal of the liquid scintillator and a signal of the plastic scintillator are detected within a 20 ns time frame at this module,

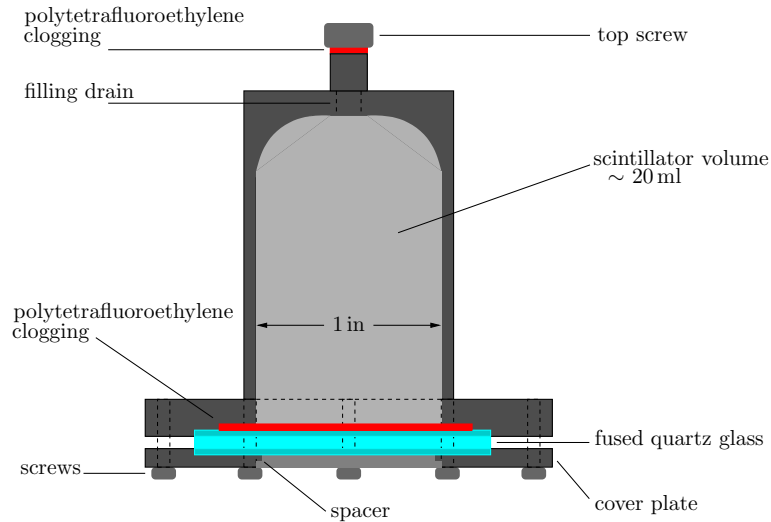


Figure 4.5: Schematic drawing of the scintillator container used, the tin. It is milled from an aluminium block. The other parts used are made of teflon (red), fused quartz glass (blue) and stainless steel (the screws). A detailed description of all components is presented within the text.

a trigger signal is generated and transmitted to the recorder. This 10 bit transient recorder (GaGe CompuScope CS82G) saves the pulses received from the Fan In/Fan Out if there is a trigger signal. In addition, the logical pulse from the Leading Edge Discriminator as well as the coincidence trigger is sent to a pulse generator (MPI Dual Gate Pulse Generator), in order to count them with a scaler (CAEN Quad Scaler and Preset Counter Timer Mod. N1145). The scaler, however, is just used for surveillance.

4.3 Investigated Scintillators

The scintillators investigated are the ones used in the running Borexino experiment and the one most probably used in the future LENA detector.

The sample from Borexino was taken from the IV in February 2011. It consists of PC with an additive of 1.5 g/l PPO and was operated for several years in the detector. The composition of the LENA scintillator is not yet finally decided. At the moment the most promising one consists of a mixture of LAB with 20 mg/l bisMSB and 3 g/l PPO. Compared to the Borexino scintillator a secondary flour (bisMSB) is added. In order to prevent self-absorption at large wavelengths it absorbs where the primary flour (PPO) emits and produces an additional wavelength shift. The mixture used was prepared directly in Munich. The absorption and emission wavelengths of the respective substances are shown in table 4.1. The given emission wavelengths are important to know, since the container materials and the PMT used have to be matched and optimized for this wavelength.

Based on the fact that scintillators react with oxygen and get polluted, provisions for



Figure 4.6: Picture of the scintillator tin used. For a more detailed description see figure 4.5 and section 4.3, respectively.

| Substance | Molecular Formula | Absorption [nm] | Emission [nm] |
|-----------|---------------------------------|-----------------|---------------|
| PC | C_9H_{12} | ~ 267 | ~ 290 |
| LAB | $C_9H_{12}(CH_2)_m, m = 7 - 10$ | ~ 260 | ~ 283 |
| PPO | $C_{15}H_{11}NO$ | ~ 303 | ~ 365 |
| bisMSB | $C_{24}H_{22}$ | ~ 345 | ~ 420 |

Table 4.1: Overview of the used scintillators and fluors along with their absorption and emission wavelengths. Data taken from [82][83].

filling the scintillator container are made to reduce air contact to a minimum. For this reason the scintillator is flushed with nitrogen before filling for approximately 5 min. The oxygen inside the container is exchanged by nitrogen. Then, a syringe is used to transfer the scintillator. When the container is filled slightly above half it is again flushed with nitrogen. Afterwards, the container is filled completely. It is taken care that no gas bubble remains in the container before sealing it. With these precautions, the scintillator remains stable and no refilling has to be done during the screening of one scintillator sample.

4.4 Light Yield Test Measurements

The measurement described in this section was first only performed as a system test, but was continued later on as a diploma thesis [69] for the Double-Chooz collaboration. The evaluation procedure, however, was originally developed for the quenching measurement and will therefore be presented and explained in the next section.

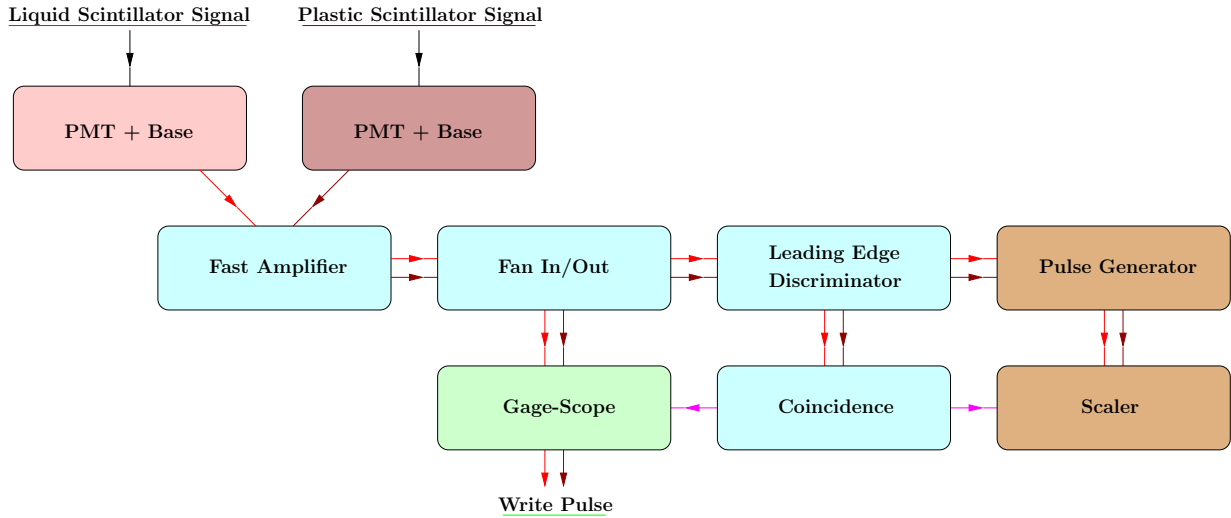


Figure 4.7: Schematic view of the electronics used. The different colors represent the different stages of the electronics chain. Red boxes mark the signal production, cyan the signal processing and green the final recording of the pulses. The electronics components for surveillance are marked in brown color.

In contrast to the measurement setup described in section 4.2.1, a weaker ^{137}Cs source is used and placed closer to the tin detector with a distance of approximately 9 cm. After proving that all the electronics work correctly and stable, a measurement of light yields concerning different scintillators is performed. During the measurement the distance and angle between source and tin is kept fixed. Regarding figure 4.3, a change in the peak position E_c is expected due to the different light yield of unequal scintillators. Because the deposited energy is directly proportional to the light yield, the relative differences in the peak position can be transferred directly to a change of the light yield. But as it is not possible to measure the total light yield with this experimental setup, only relative differences in the light yield can be determined. As a consequence, the first measurement to be done is a reference measurement with a well known scintillator, as already mentioned in section 3.3. Using this approach and setup, the scintillators finally used for the muon veto scintillator and the buffer liquid of the Double-Chooz detector were investigated (see table 4.2). The detailed work and analysis for this measurement series can be read in [69]. A similar measurement was performed in context of a bachelor thesis [84]. Here, the influence of oxygen contamination on the light yield of liquid scintillators was examined. The results are collected in table 4.3. Although the first measurement (after 0.25 days oxygen exposure) seems to stick out, an impact of the air contamination on the light yield is visible and should be investigated more in detail in the future.

| Muon Veto Scintillator | Buffer Liquid |
|--|--|
| 48.4 % vol. LAB 51.6 % vol. n-paraffin 2 g/l PPO 20 mg/l bisMSB | 46 % vol. n-paraffin 54 % vol. Ondina 917 |

Table 4.2: Liquids used in the Double-Chooz detector as investigated in [69].

| Time of Contamination [days] | Relative Light Yield |
|------------------------------|----------------------|
| 0 | 1.000 |
| 0.25 | 0.913 ± 0.022 |
| 1 | 0.981 ± 0.021 |
| 3 | 0.949 ± 0.025 |
| 7 | 0.966 ± 0.022 |
| 14 | 0.949 ± 0.025 |
| 35 | 0.938 ± 0.022 |

Table 4.3: Influence of oxygen contamination on the light yield of liquid scintillators as performed in [84]. It is obvious that the degrading light yield is linked to the length of oxygen exposure.

4.5 Quenching Measurements

The main purpose of the described experimental setup in this chapter is the determination of the electron quenching factor of liquid scintillators, the Birks factor k_B . After having proven the stability and the principle functionality of the system using the light yield measurements introduced in the previous section, the strong source mentioned in section 4.2.1 is again placed on the rail. A typical PMT-pulse received and recorded by the transient recorder is depicted in figure 4.8. It shows a clearly identifiable PMT peak with a smooth baseline. The time position of the pulse is determined in reference to the applied trigger signal. As a test for the coincidence setup, the timing of the two recorded pulses (generated by the tin and the reference detector) in relation to the coincidence trigger can be regarded. With a stable coincidence setup, the timing of the two detectors in reference to the trigger should be similar and should remain stable. The programs used for data evaluation are C++ based using an object orientated analysis framework called ROOT [85]. The result of one randomly picked angular measurement is depicted in figure 4.9. Indicated by color is the the respective amount of bin entries. The event spot ① (marked in black) is an indication for the coincidence setup working correctly as both detectors record most of the signals at the same time. The other events ②, ③, ④ (marked in gray) are coincidences not generated by the source. They consist of random coincidences or electronic noise. Each measurement for one certain scattering angle consists of 8000 pulses

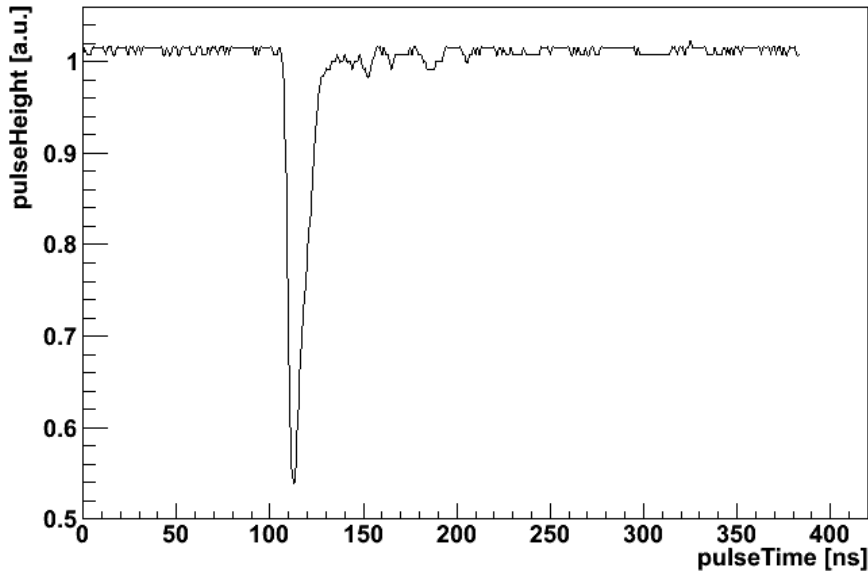


Figure 4.8: Picture of a single recorded PMT-pulse. Visible is the falling pulse itself and the baseline with minor oscillations. The area of the pulse can be used to calculate the deposited energy. Important for later analysis is in addition the time of the peak maximum.

complying with the coincidence settings and takes about one day of data taking. The pulse distribution for the 165° recording is shown in two 2-dimensional histograms with color coded bin entries in figure 4.10. As can be seen, the main amount of pulses is within the same size and shape. Also the timing with respect to the trigger is stable for all pulses. However, some show strong baseline fluctuations (marked in black) and do not comply with the ideal form presented in figure 4.8. Therefore, these pulses are not valuable for the coincidences measurement and contribute to the background. For the further analysis, pulses with too large baseline variations are excluded. To determine the deposited energy, the area of each pulse is calculated. This value is then used to generate the needed spectra that is illustrated in figure 4.11. The shape of the spectra is in good agreement with the expected schematic one, that is demonstrated in figure 4.3. Therefore, the fit function

$$F = p_2 \cdot \exp \left[-\frac{1}{2} \left(\frac{x - p_3}{p_4} \right)^2 \right] + \exp(p_0 + p_1 \cdot x) \quad (4.3)$$

can be used to describe the graph's characteristics. F gives the number of entries per area. The variables p_0 to p_4 are fit parameters adapted by the fit routine. The one used for subsequent analysis is p_3 that specifies the peak position and, therefore, the demanded deposited Compton energy of the respective scattering angle.

In order to determine the Birks parameter k_B , different scattering angles have to be scanned. As PC is the first scintillator investigated, the energy region of interest has

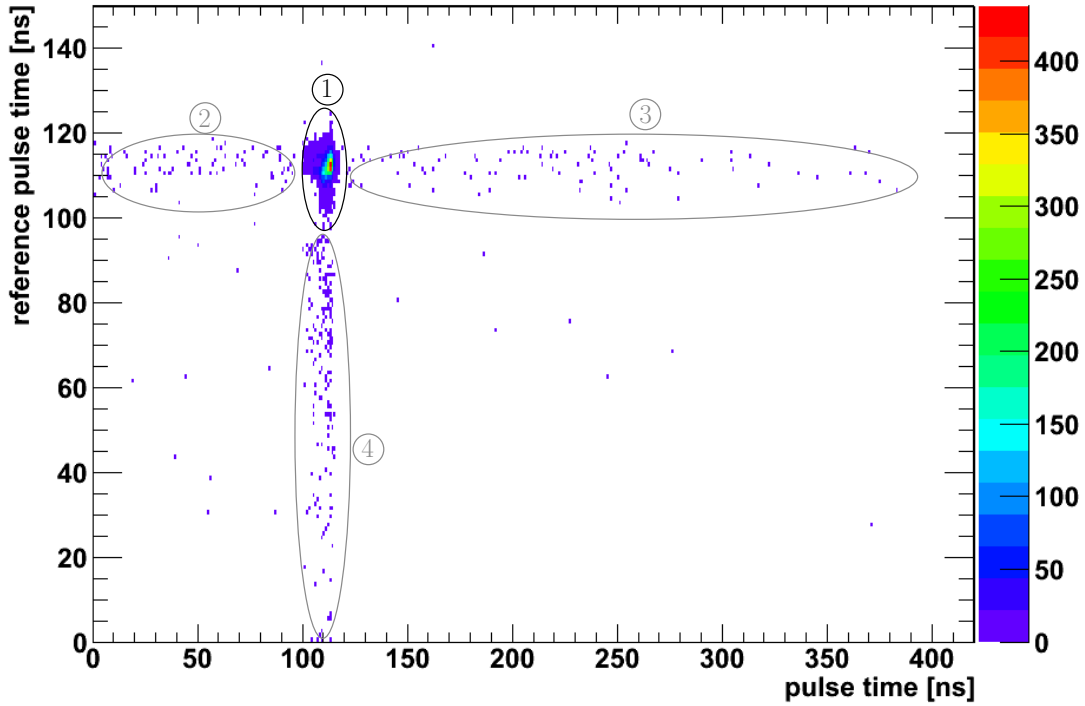
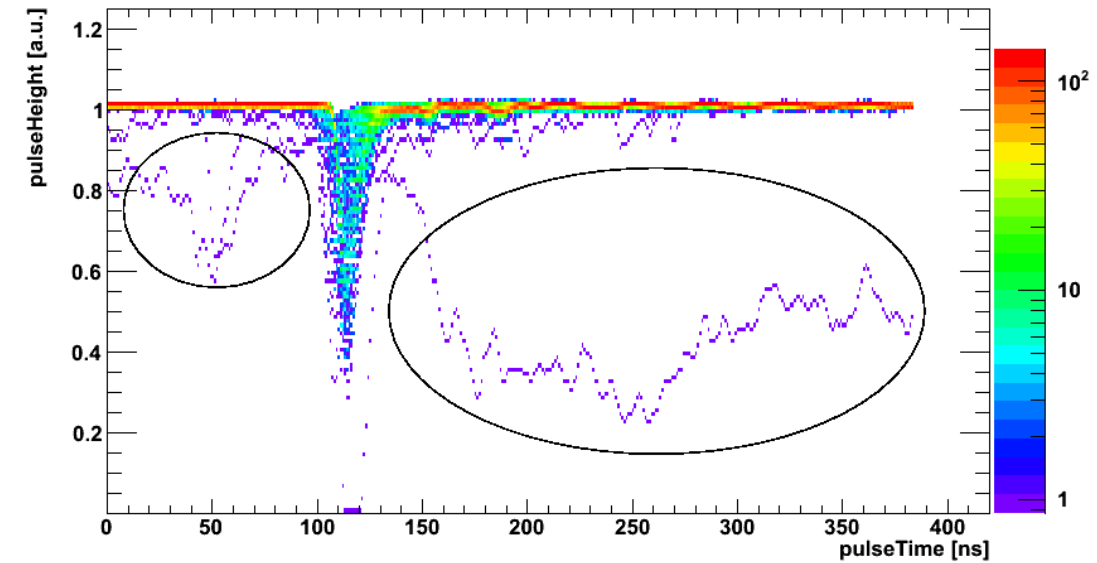


Figure 4.9: Affirmation of the coincidence timing. Shown is the time of the peak maximum in relation to the trigger signal for the pulses generated by the tin detector (x-axis) and the reference detector (y-axis). The color indicates the amount of the respective bin entries. Events ① marked in black are generated by the radioactive source complying with the coincidence setup. The events ②, ③, ④ marked in gray are due to random coincidences or electronic noise and, therefore, contribute to the background.

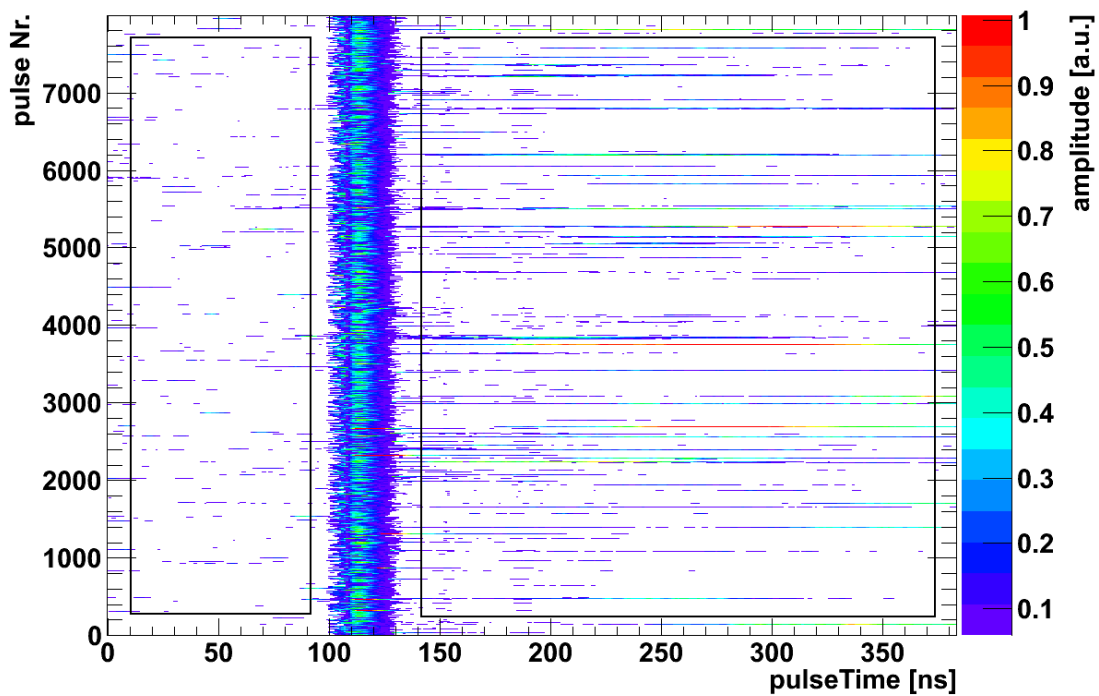
to be narrowed first. It turns out that the energy determined for larger scattering angles ($> 55^\circ$) shows a linear behaviour. In addition, the quenching is meant to be prominent for small energies. For the PC measurement of 15° a separation of the Compton peak and background signals was not possible anymore. Therefore, more angles are measured compared to the later series of LAB. The angle test series performed are exhibited in table 4.4 along with the calculated Compton energy of the recoil electron E_e for the respective angle (see equation 4.2).

4.6 Systematic Uncertainties

Before the final value of the Birks factor k_B is given in the next section, an overview of the errors that have to be taken into account for the measurement and the calculation is given in the present section.



(a)



(b)

Figure 4.10: Pictures of all recorded PMT-pulses for the 165° measurement of PC. pulse-Time refers to the respective time recorded for each received trigger.

(a) The color indicates the respective amount of bin entries. As can be seen, the baseline is stable for most pulses over time and the pulse form is as expected (see figure 4.8).

(b) For each pulse the time in respect to the trigger is shown along with an indication of the recorded pulse height (amplitude of the pulse). Most pulses are in good agreement in timing and amplitude to each other.

In both cases (a) and (b), pulses showing baseline fluctuations are marked in black. These pulses differ from the ideal pulse form (4.8) and therefore contribute to the background.

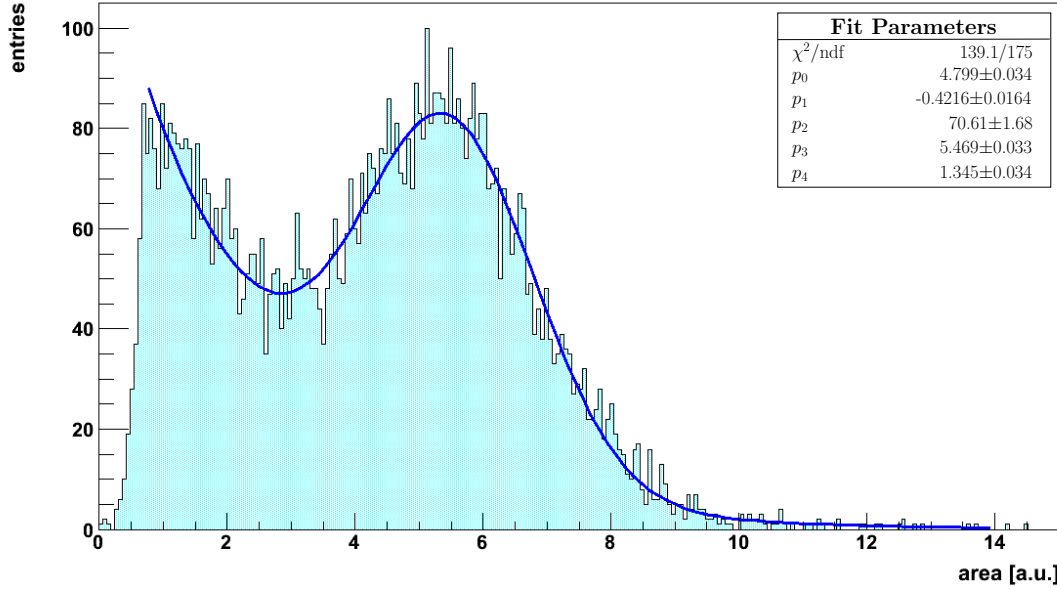


Figure 4.11: PC energy spectrum of the 165° measurement gained from 8000 single pulses. The integrated area corresponds to the deposited energy in the liquid scintillator. Visible in blue is the fit already applied to determine the value of the Compton energy at the respective angle. The fit parameters given are identical to the ones as defined in equation 4.3. The peak position that will be used later on, is given by p_3 .

| | | | | | | | | | | |
|----------------------|-----|----|----|-----|-----|-----|-----|-----|-----|-----|
| Angle [°] | 15 | 25 | 30 | 35 | 40 | 45 | 50 | 55 | 65 | 75 |
| Compton Energy [keV] | 28 | 72 | 98 | 126 | 154 | 182 | 209 | 235 | 283 | 324 |
| PC | (✓) | ✓ | ✓ | ✓ | ✓ | ✓ | ✓ | ✓ | ✓ | ✓ |
| LAB | | ✓ | | ✓ | ✓ | ✓ | ✓ | ✓ | | ✓ |

| | | | | | | | | | | |
|----------------------|-----|-----|-----|-----|-----|-----|-----|-----|-----|-----|
| Angle [°] | 85 | 95 | 105 | 115 | 125 | 135 | 145 | 155 | 160 | 165 |
| Compton Energy [keV] | 358 | 387 | 410 | 429 | 444 | 456 | 464 | 471 | 473 | 475 |
| PC | ✓ | ✓ | ✓ | ✓ | ✓ | ✓ | ✓ | ✓ | ✓ | ✓ |
| LAB | | | | ✓ | | | | | | ✓ |

Table 4.4: Test series of angles performed for the quenching measurements with the corresponding calculated Compton energy (see equation 4.2). The PC measurement in brackets was not used for later analysis, as the Compton peak could not be distinguished from the background.

4.6.1 Setup Accuracy

The first point that has to be considered is the experimental setup itself. The design was developed with the purpose to keep the error of the scattering angle in an acceptable

margin and the observation rate still at a decent range. The compromise found are the measures already described in section 4.2.1 resulting in an error for the scattering angle of under 5%. This error directly transfers into the error of the expected theoretical value of the Compton energy using equation 4.2. The accurateness of the manufacturing is precise enough so it has not to be taken into account compared to the previous mentioned spatial error.

Secondly, the error of the deposited energy is given by the fit shown in figure 4.11 and is strongly dependent on the overlap of signal and background. Hence, it is small for high energies and grows for smaller values. Also the lead shielding has an influence on the data. Gammas emitted by the ^{137}Cs source scatter off the lead and are generating a signal that complies with the coincidence settings. However, the energy detected is smaller than the one expected for the corresponding angle. This leads to a broadening of the Gaussian fit distribution. The total fit error ranges between 0.6% and 3.5%.

All errors are implemented in the final data set and are therefore considered by the final fit that will be introduced in section 4.7 and results in the kB-factor.

4.6.2 System Stability

The stability of the system is validated in several ways. The light yield measurement, described in section 4.4, is a first test of the running system and shows good behavior of all components. In order to examine the influence of the electronics used, more surveillance is necessary.

The linearity of the complete electronics system, including all electronic parts starting from the PMT until the transient recorder, has to be verified. Two different possibilities were used to do so. In both cases, a LED is used as a light source emitting at a wavelength comparable to the one of the liquid scintillator. It is powered by a tail pulse generator (BNC Model BH1). With a frequency of 1 kHz, a time delay of 100 μs , a rise time of 20 ns and a decay time of 100 ns a scintillator pulse is simulated. For the first set of measurements, the amplitude was fixed to a value of 3.725 a.u. and different optical filters were inserted between the LED and the PMT. With the known optical absorbance, the recorded energy distribution can be tested for a linear behavior. The result achieved for this technique is depicted in figure 4.12. The linear and thereby expected behavior of the electronics is existent, especially in the energy region of interest, i.e. peak areas < 7 a.u.. But, as the optical absorbances of the filters are just known to a certain degree of accurateness, there is a second method to test the energy stability of the system independently of these uncertainties. Therefore, only one filter is used for the complete test. A set of measurements consists of a fixed amplitude measured with and without the absorber. Varying then the amplitude of the LED-pulse between the different sets, the ratio between the two energies recorded should remain the same. The values gained for the experimental setup used are shown in figure 4.13 and show the same linear behavior as before. The bend visible in both stability plots is caused by the Gage-Scope card. Due to the high energies of the detected LED pulses, a wide energy range had to be recorded. Therefore, the setup of the Gage-Scope card had to be changed for high pulses compared to small ones. However,

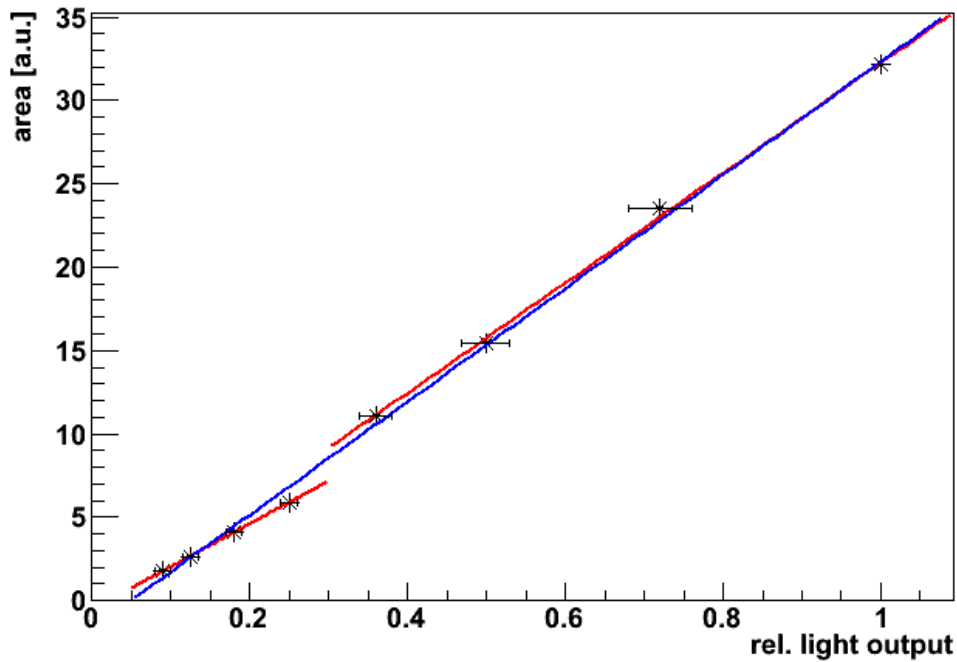


Figure 4.12: Using a LED as light source and different well-known optical filters, the linearity of the electronics system can be tested. The peak area, depicted on the y-axis, represents the detected energy (see figure 4.11). On the x-axis the normalized light output after the respective used filter is marked. The blue line describes a linear fit to the full data set. It can be seen that there is a small bend due to the electronics used (explanation in the text). Therefore, different intercepts in energy are considered. The two linear fits depicted in red comply with the data. As the energy region of interest for the quenching measurement is peak areas < 7 a.u., only the lower left fit has to be used and the system can be regarded as stable and linear in energy.

the energy measured in the quenching measurement is smaller than peak area < 7 a.u., as already mentioned. Consequently, this bend does not effect the taken data and can be neglected. The total system can be regarded as linear for the energy range of interest. Last, especially for the long test series performed for PC, the stability of the scintillator itself has to be monitored over time. Therefore, the energy spectrum for one and the same angle is measured several times after different time spans. The result is depicted in figure 4.14. It can be seen that despite all precautions the scintillator is not stable in time. It is assumed that this decay is originated from a small oxygen pollution of the liquid scintillator. Hence, it is decided to adjust all recorded data with the applied exponential fit for the later evaluation of the kB-factor. For each different measurement the time span to the first measurement performed is known. Using this value as input for the presented exponential fit (see figure 4.14), the total data set recorded is energy corrected as if it was taken at just one day.

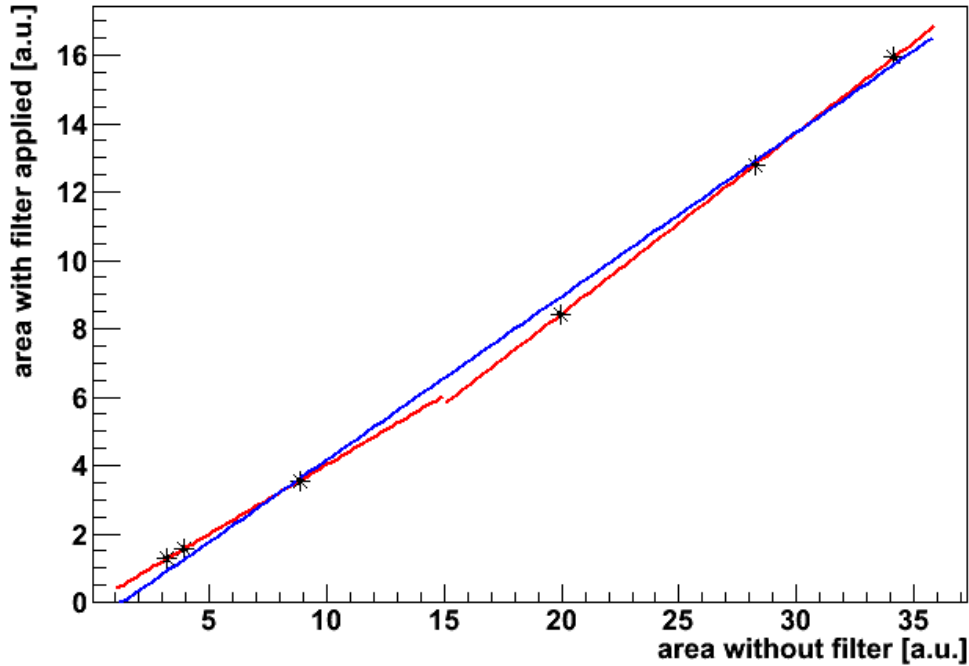


Figure 4.13: Second performed test of the system’s energy stability. Recorded energies, measured with (y-axis) and without (x-axis) optical filter, are plotted for different LED amplitudes. As already described in figure 4.12, the full data set is first fit linear (blue fit). There is a small bend (explanation in the text) that vanishes if sub energy regimes are regarded (2 red fits). For these a good linear behaviour of the system is found. As the energy interesting for the quenching experiment is peak areas < 7 a.u., only the lower left fit has to be used and the electronics system of the experiment shows the expected linear behavior.

4.7 Results – Birks Factor

To determine the Birks factor k_B , the energy corrected data, explained in the previous section, is used. Using the expected Compton energy compared to this deposited and detected energy, the gained data sample can be explained by the integral of equation 3.4 including the energy corrected Bethe-Bloch equation 3.6. This is done by a fit, using the k_B factor as an arbitrary fit parameter and a χ^2 minimization. The absolute scintillation efficiency L_0 can be extrapolated from the taken data and can be used as a start parameter for the fit routine. It serves as kind of normalization to adjust the scale. As quenching occurs mainly for low-energetic electrons, it is appropriate to assume the quenching as negligible for higher energies. Therefore, the needed value L_0 can be estimated by a linear fit to data points of the higher energy regime ($E_c > 300$ keV).

The total data sets and the resulting fit functions for PC and LAB are depicted in figures 4.15 and 4.16, respectively. The expected energy, determined by the Compton scattering,

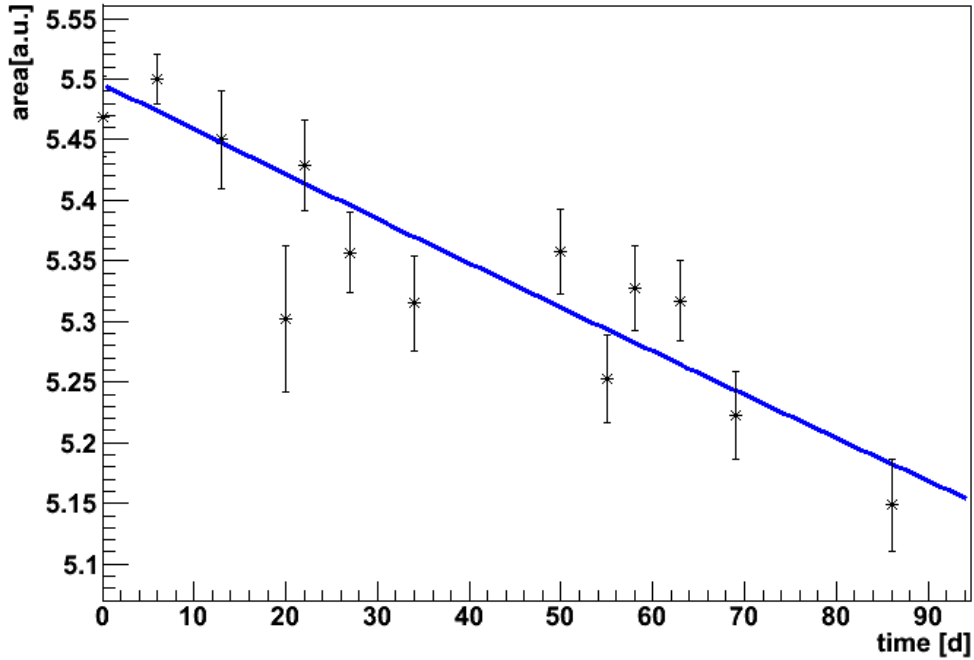


Figure 4.14: Detected Compton energy (represented in measures of the peak area in a.u.) for one and the same angle (165°) after certain time periods determined for the PC scintillator used. In blue, an exponential fit to the data is presented showing the decay of the light output.

is depicted on the x-axis in measures of eV, the detected energy is registered on the y-axis in arbitrary units of the enclosed area. The applied fit is demonstrated by the blue curve. The fit results of the respective kB-factors are collected in table 4.5.

Comparing the achieved value for PC with the one presented in [79], $k_B = 0.0172 \pm 0.0006$, an agreement within the errors can be found. Therefore, the kB-factor used in data analysis and simulations by the Borexino collaboration can be verified. Furthermore, it is shown that the method used in the present work to determine the kB-factor is credible and valid and, therefore, is an alternative and cross-check to the method presented in [79].

However, the gained value for LAB seems too high. There was no exactly equal sample tested in [79] making the comparison difficult. But the order of magnitude should be in the same range compared to PC. Therefore, it seems that the Birks gained factor for LAB is at least a factor 10 higher than expected. An explanation for this behavior can be found in the scintillator probe used. Later independently performed measurements [84][86][87] showed a very short attenuation length (≈ 3 m) for a LAB sample taken from the same storage container. This is a hint, that the used scintillator is polluted not only with oxygen, but also with other materials due to an inappropriate storage containment. These impurities change the ionization taking place in liquid scintillators. Therefore, for polluted samples an increase of the quenching is expected, resulting in a higher Birks factor than normal.

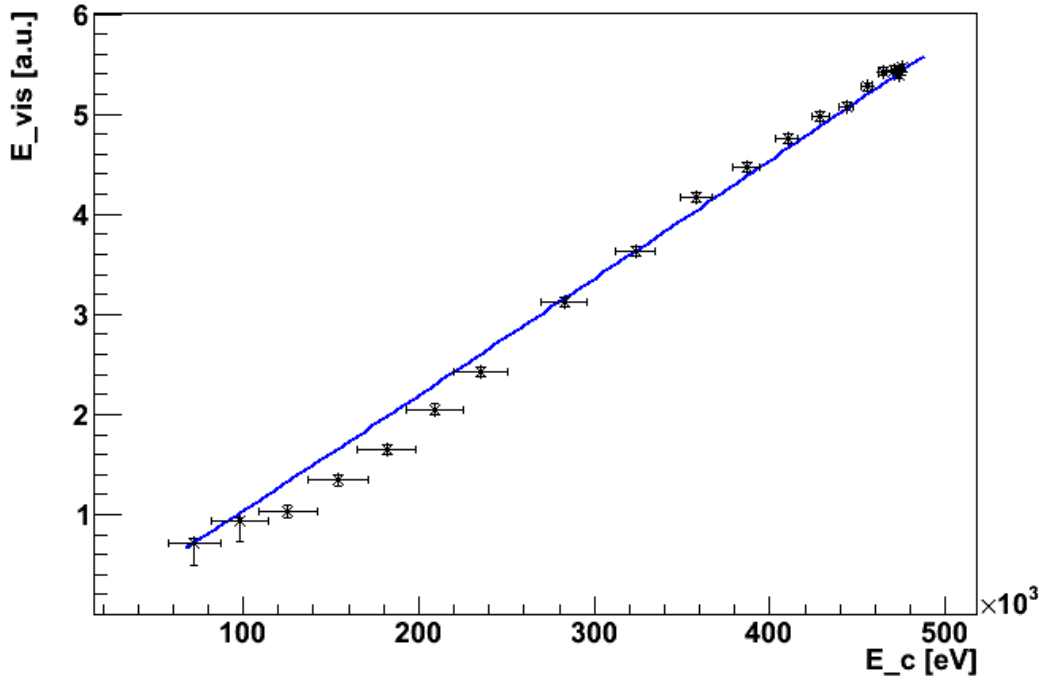


Figure 4.15: Final fit (blue line) determining the kB-factor for PC. E_c represents the calculated energy using equation 4.2, E_{vis} the detected energy in arbitrary units. The fit provides a kB-factor of $0.016 \pm 0.001 \frac{\text{cm}}{\text{MeV}}$.

So, as the LAB scintillator used for the quenching measurement presented in this thesis was strongly polluted, the increase of the kB-factor can be explained. Unfortunately there was no time to order a new and clean scintillator sample to redo the measurement because the radioactive source had to be returned and the experimental setup was already used for other measurements with a new electronic setup.

The presented results show that for liquid scintillator experiments, and therefore also for solar neutrino experiments, it is important to measure the actual scintillator used in the detector. Possible pollution can generate a difference between the kB-factor of the actual scintillator used and the in the laboratory measured reference sample. This may lead to errors in simulations or even in data analysis.

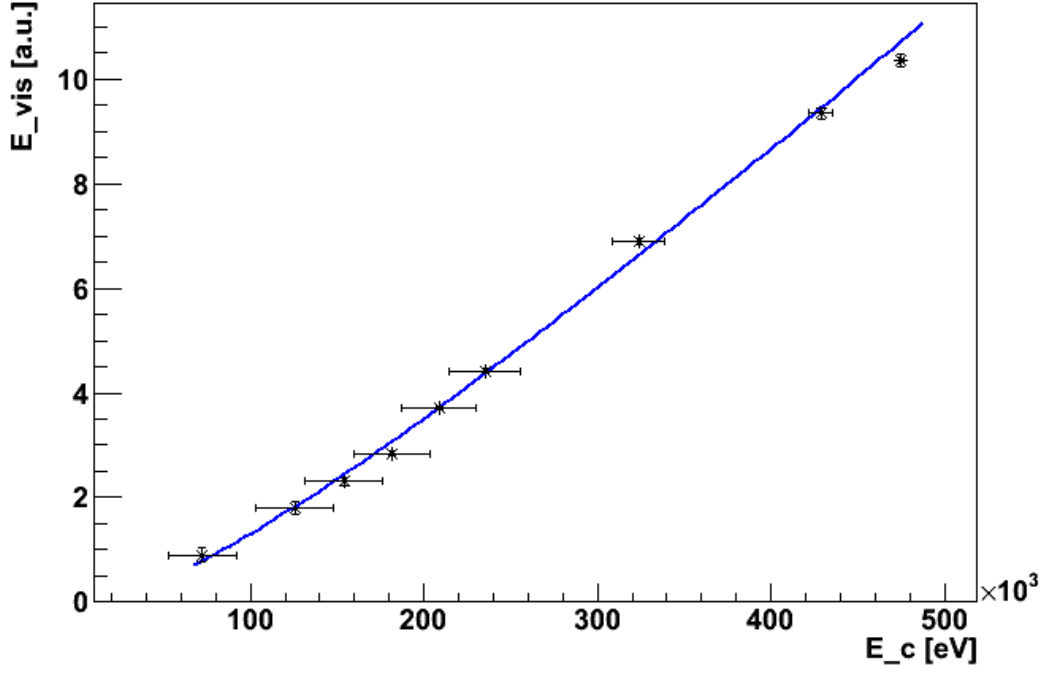


Figure 4.16: Final fit (blue line) determining the kB-factor for LAB. E_c represents the expected calculated energy using equation 4.2, E_{vis} the detected energy in arbitrary units. The fit provides a kB-factor of $0.342 \pm 0.013 \frac{\text{cm}}{\text{MeV}}$.

| Sample | kB-factor | Error |
|--------|-----------|-------|
| PC | 0.016 | 0.001 |
| LAB | 0.342 | 0.013 |

Table 4.5: Final results for the Birks factor including the fit errors for the two measured samples. Taking into consideration the respective absolute scintillation efficiency L_0 the values of the kB-factor are in units of $\frac{\text{cm}}{\text{MeV}}$.

Chapter 5

BOREXINO Background Rejection

A next point for low-energy neutrino experiments is the knowledge of background signals prominent in the data. Therefore, not only the different particles interacting in the detector have to be exactly known and identified, but also the electronics behavior itself needs to be understood. This chapter copes with this topic. First, an overview of the different expected background signals is given, followed by an introduction to a simulation software that was developed in the context of the present thesis. Last, an analysis of muons and neutrons originating indirectly from CERN [88] and detected within Borexino is presented.

5.1 Background Signals

In this section the most prevailing background sources are explained. Two different cases can be distinguished. The first are background events due to radioactivity being contained inside the detector itself. Those especially interfere with signals in the low-energy regime. In contrast, the second case that has to be considered, leaks also into high-energy regions. Although Borexino is located in an underground laboratory, not all unwanted particles can be shielded before entering into the detector. Muons, generated in the atmosphere, can pass through the surrounding shielding of rock and enter the detector, or can generate secondaries on their way. All these background events have to be well understood in order to gain information on the wanted neutrino signals.

5.1.1 Radioactive Contaminants

Most of radiation, interfering with the neutrino signals in the low energy window, are due to the scintillator itself. The liquid is organic and has unstable components, mainly ^{14}C . This isotope plays a dominant role in the energy region up to the endpoint of its β -spectrum at 156 keV. As it is a β -emitter, it mimics a neutrino event in the detector and, therefore, interferes directly with the neutrino detection.

Other radioactive isotopes, that are diluted in the scintillator, are components of the ^{238}U and ^{232}Th decay chains like ^{210}Pb and ^{210}Po . They can be dissolved in the liquid by surface

contact with the respective containment. But, because many of them are α emitters, a pulse shape discrimination can identify these background signals. Some of the few dissolved β emitters can be associated with their decay chains. Therefore, these isotopes can often be tagged using time and spacial coincidences. A well-known example is the fast ^{214}Bi - ^{214}Po coincidence.

A next important source of radiation is due to air leaks. Radon and Krypton are offered the possibility to enter into the sensitive detector volume and therefore contribute to the background. As Radon nuclei are part of the previous mentioned U/Th decay chains, these will decay to Po, Pi and Pb nuclei. For Krypton, a sub-dominant decay branch offers the possibility to identify the nuclei, using a $\beta\gamma$ -decay signal.

Last, external γ radiation has to be taken into consideration. Here, especially the radiation emitted by the glass of the PMTs, containing ^{40}K , has to be mentioned. But also γ radiation from outside the detector may enter. Therefore, shielding has to be applied to the experiment. In Borexino, this is done by the surrounding water tank and the buffer liquid.

5.1.2 Muons

The most obvious and visible contribution to background is due to muons. They are generated by cosmic rays in the atmosphere of the Earth. Here, protons generate hadronic showers that consist mainly of unstable mesons. The decays of these mesons produce muons. The muons typically have enough energy, so that they are not just able to reach the Earth's surface, but also to penetrate it to a certain depth. However, the other still existing components of the shower are stopped by some meters of overburden. Therefore, just muons remain as background for experiments located in underground laboratories. Depending on the amount of shielding, the mean energy of the muons is modified. It will rise with the depth of the used underground facility, since low-energy muons are stopped in the rock.

Most of the remaining muons that reach the detector still have enough energy to pass it completely. Just a few will be stopped inside the detector as the energy loss of the traversing muon is only approximately 2 MeV/cm. The muons arriving and entering e.g. at the Borexino detector have a mean energy of 280 GeV.

However, a muon is easily detectable inside the detector and, therefore, not too threatening for data evaluation. Though, the muon is able to generate secondaries on the way through the surrounding rock of the detector or in the detector itself, which are much harder to identify and to detect. These possibilities are described in the next two subsections.

5.1.3 Muon Induced Spallation Processes

A muon traversing the detector has the opportunity to hit nuclei of the detector materials and may create unstable states. As ^{12}C is one of the most abundant nuclei the probability to hit it is quite high. In doing so, some nucleons can be knocked out and ^{11}C or ^{10}C can be produced. Both visible isotopes act as a β^+ source and, therefore, interfere with the

neutrino detection. The released decay energy of the ^{11}C is located in the 1–2 MeV region and, therefore, interferes with the pep- and CNO neutrino detection. The energy of the ^{10}C is a bit higher and, hence, affects the ^8B neutrino detection.

A mechanism used by the Borexino collaboration to identify and veto the signals originated by ^{11}C and ^{10}C is the so-called Threefold Coincidence Technique [89][90].

5.1.4 Neutrons

The last background to be mentioned is due to neutrons. Low-energy neutrons can be absorbed by shielding material whereas high-energy ones can penetrate into the sensitive detector volume. These fast neutrons are knocked out of some nucleus by the previously mentioned cosmic muons. Generated in the detector, they can easily be vetoed because of the detectable parent incident particle, the muon. Problems emerge from neutrons generated outside the detector. There, no muon can be detected and the signal of a captured neutron inside the scintillator can mimic an antineutrino signal.

Anyway, an interesting and important property is the number of neutrons generated by a muon per meter track length inside the scintillator. This is described by the so-called neutron multiplicity. An analysis of this parameter, performed in the context of the present thesis, is explained later on in section 5.3.

5.2 BOREXINO's Outer Detector

A lot of background, present in a liquid scintillator neutrino detector, is generated by muons. Therefore, it is essential to first identify the muon correctly, and second, to know the exact track of the muon. Therefore, the Outer Detector has been build for the Borexino project. It is crucial to know the exact response and behavior of this subdetector. As a part of this thesis, the electronics used for the Outer Detector is studied and implemented into a simulation program. Using the simulation that takes also the influence of the electronics on recorded data into account, the tracking mechanism can be tested. The design of the outer water Cherenkov detector itself is described in section 2.3.

5.2.1 Electronics

The electronics of the Borexino detector is located in a separate room next to the experiment. The signal and high voltage cables of the PMTs are terminated here. The electronics used for the Inner and the Outer Detector are slightly different. The electronics of the Inner Detector is already completely included into a simulation tool, whereas this is done for the Outer Detector in context of this thesis. Therefore, the description of the electronics is limited to the Outer Detector's one. The rest of the system is described in [91].

The two racks, hosting the Outer Detector's electronics, are schematically depicted in figure 5.1. In the following the main focus is put on the electronics that are included into the simulation tool. The others will be just explained briefly. The spare boards located in a

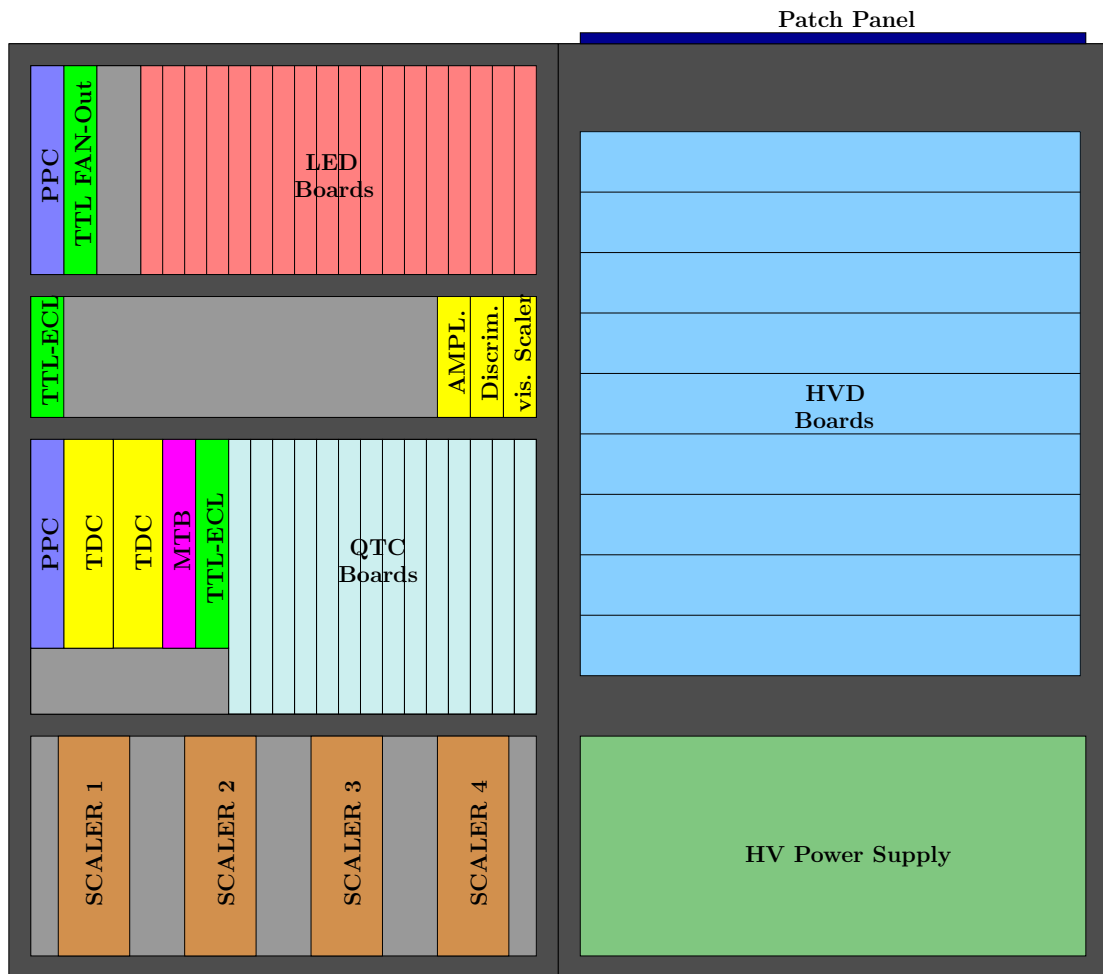


Figure 5.1: Schematic view of Borexino’s Outer Detector electronics hosted in two racks. The main parts are explained within the text.

NIM crate underneath the LED boards will not be explained in the following.

At the Patch Panel (dark blue) the cables of the Outer Detector’s 208 PMTs arrive and are forwarded to the HVD-boards. All the cables used are of equal length to reduce differences in the signal timing.

The HVD-boards (High-Voltage-Decoupler boards (light blue)) separate the PMT signal from the applied high voltage. In total, there are 9 boards with 24 channels each. In addition, a pulser system is included to check for damaged electronics channels by injecting a reference signal (see [64] for more detailed information). The decoupled or injected signal is forwarded to the QTC-boards.

At the bottom of the first rack, the HV Power Supply (light green) is located. Each PMT is powered for its own with a voltage of 1150 V to 1750 V, resulting in a gain of 10^7 . The HV system can be used to identify tripping or flashing PMTs.

The 18 LED Boards (red) are used to generate calibration light pulses for each PMT. These pulses are transmitted via optical fibers. Once per week this system is used to check the PMTs behavior in charge and time response.

The NIM-TTL-ECL (green) boards are logic translators. These level translations between the NIM- and TTL-signals allow a communication between the different module types used.

The communication to the single crates is ensured by the use of PPCs (blue). These Power PCs can be accessed via Ethernet and allow a remote control of most of the settings necessary.

The Muon Trigger Board (MTB (violet)) interprets the signals generated by the QTC-boards (see below) and generates a trigger signal, so the event is recorded. For a detailed view of the trigger system, the Outer Detector trigger as well as the Inner Detector trigger, see [91].

At the bottom of the left rack, 4 Scalers (brown) are located. They count the signals generated by the QTC-boards and are, therefore, used to monitor the signal rate at the counting room and to check for incorrectly working PMTs and electronics channels.

The most important part of signal processing are the 14 QTC Boards (light gray). They are so-called charge to time converters with 16 channels each. The first channel (channel number 0) is not used for PMT signals, but is reserved as service channel. In total, there are three outputs generated. Two for the trigger system and one for the further data acquisition and recording. The latter is sent to the TDC boards, and is essential for the electronics simulation. In order not to trigger on noise, a threshold is defined at -20 mV corresponding to 0.2 photoelectrons against the amplified ($\times 11$) copy of the input signal. The conversion of charge into time is done by integrating the input pulse. Using an offset P of the respective channel, the channel gain G and the recorded charge Q the time length T of the hit calculates to $T = P + G \cdot Q$. This value is used for further data processing as it bears most of the important hit information. The offset, also called pedestal, is determined at the beginning of each data taking run for each channel and is written to a database for later access.

The last modules to be mentioned are the two Time to Digital Converters (TDC (yellow)) generating the final output format of the processed signals. Each TDC board contains 4 TDC chips, each with 32 channels. The units keep recording data in a ring memory until receiving a trigger signal from the MTB. Then, the memory is read out backwards for the last approximately $8.5 \mu\text{s}$. The information written are the start and stop time of a

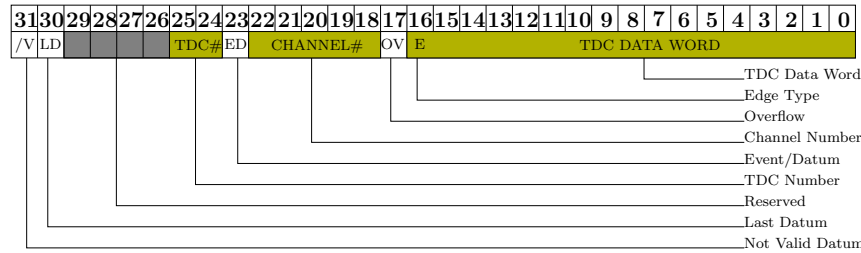


Figure 5.2: Structure of the 32-bit data word output of the TDCs. The colored parts are essential for the simulation of the Outer Detector’s electronics (section 5.2.3).

single event (called edges) making it possible to calculate the duration of the event. Hence, the edges are transferable to the charge information of the registered event, as mentioned before. This information is stored in the so-called TDC Data Word. The structure of the final all-including 32-bit data word that is written to hard disk and used for data analysis, includes the TDC Data Word as a part of it. A schematic view of the bit structure is depicted in figure 5.2. Here, the colored parts are essential for the later-on explained simulation of the Outer Detector’s electronics (see section 5.2.3) and contain important data used for event reconstruction, like charge and time. The other parts contain service information. In order to avoid problems identifying and allocating the recorded data to the respective TDC board and chip, so-called integrity channels are introduced, and are always fed with a generated integrity signal. They are similar to the service channels of the QTC-boards.

5.2.2 Electronics Stability

In order to calibrate the Outer Detector system, there are two independent systems, the LED and the pulser system. The LED system sends a defined light pulse to each PMT testing the total data acquisition system whereas the pulser system injects a reference signal directly into the HVD-boards testing only the electronics chain. But also these two systems may fail or be corrupted somehow as happened in the past. Another good and independent way to crosscheck the system stability is to monitor the taken data itself. This is unaffected by possibly wrong settings of the two calibration systems, in first order. Therefore, a macro was developed within the scope of this thesis to observe the data taken by the Outer Detector against time. The gained gradient gives a clue whether the total system remains stable or if problems occur.

The datasets used for this purpose are so-called dst files, from which the ^{14}C induced background events are already removed. The time span observed within this thesis ranges from the beginning of data taking in May 2007 until beginning of March 2013, represented by different increasing run numbers. As there are three different muon tagging systems, they are all used here and compared to each other in order to gain the best certainty achievable in the observation of the system stability. The different tags are done by the MTB, the

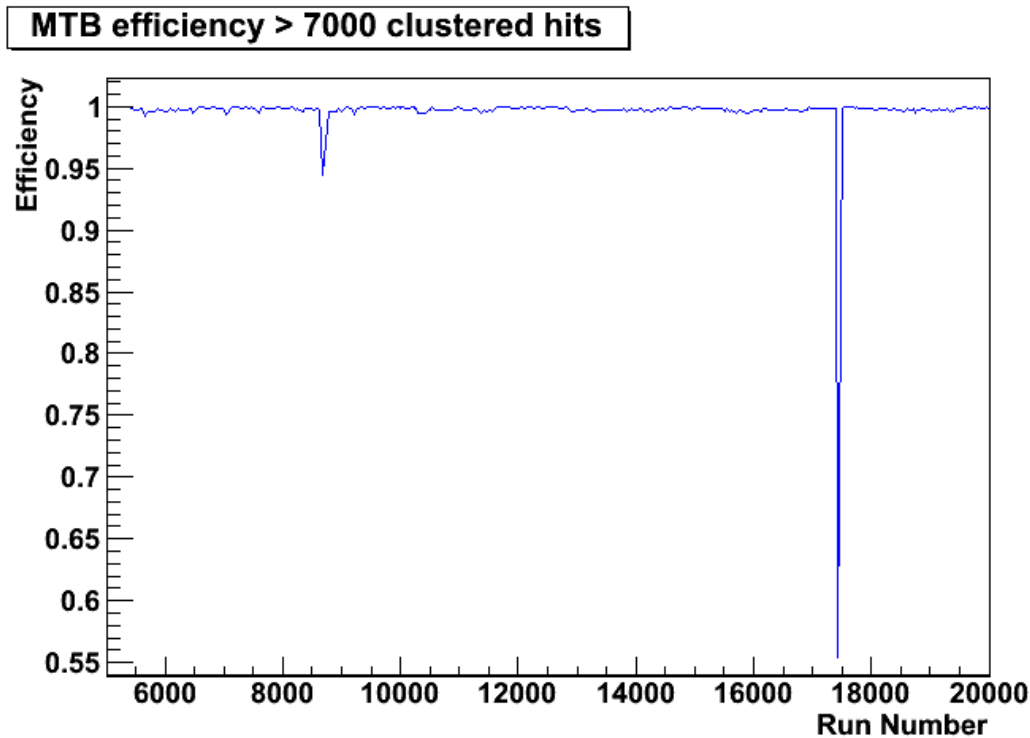


Figure 5.3: Stability and efficiency of the MTB. Depicted is the ratio of mouns tagged by the MTB to all tagged muons. The variable used to select the energy region of interest is clustered hits, a nonlinear energy observable. For clustered hits < 7000 the different muon tagging systems can't be compared to each other. As can be seen, the system is stable despite some minor fluctuations and two bigger spikes. The investigated data spans from the beginning of data taking in May 2007 until the beginning of March 2013.

MCR and the IDF. MTB is the trigger of the Outer Detector itself, the previously mentioned Muon Trigger Board. The MCR is the Muon Clustering of the Outer Detector's track reconstruction module. And finally, the IDF is the Inner Detector Flag. It uses pulse-shape discrimination to identify muons. The stability of the system can be checked using the ratio of different combinations of the respective detected number of events to the total sum of all detected events. Three different ratios to monitor the stability are regarded in the following. To test the Outer Detector's muon tagging stability, the number of MCR and MTB tagged muons to the number of all detected muons are regarded, respectively. To check the IDF, the amount of the MCR and simultaneously IDF tagged mouns is compared to the amount of just MCR tagged mouns. In addition, the energy of the observed muons has to be high enough, so the muon track reconstruction is working correctly. Otherwise the tagging systems cannot work correctly and, hence, can't be compared to each other. The energy variable used is called clustered hits, a nonlinear energy observable. The energy region of interest is defined for clustered hits > 7000 . The final plot results showing the

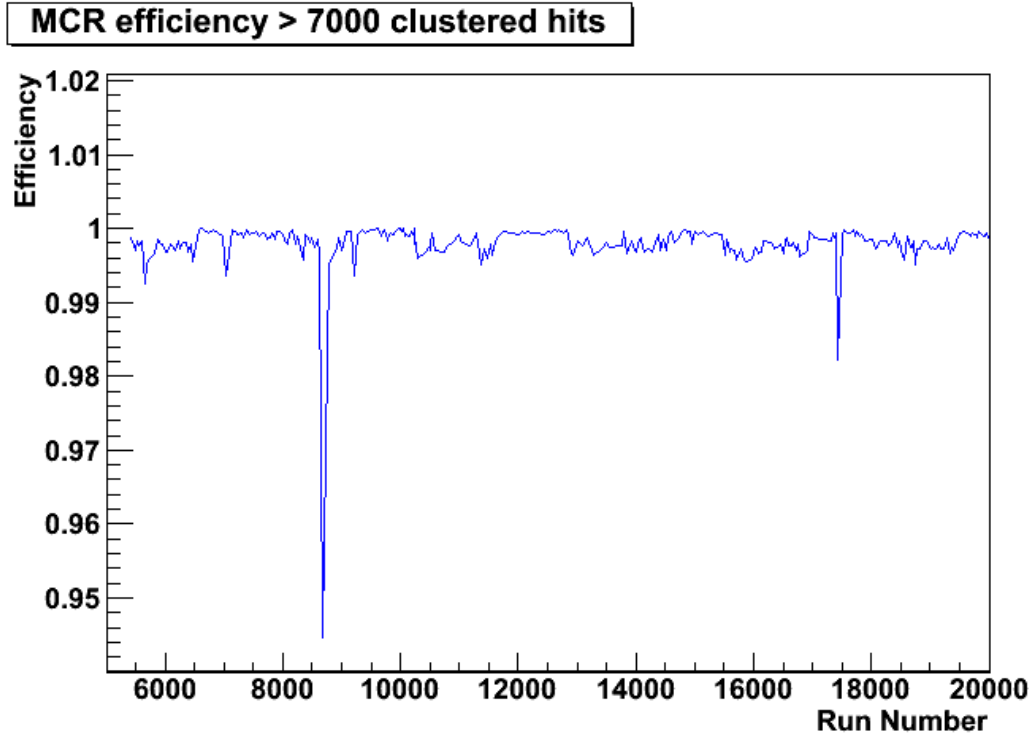


Figure 5.4: Stability and efficiency of the MCR. Depicted is the ratio of mounes tagged by the MCR to all tagged muons. The variable used to select the energy region of interest is clustered hits, a nonlinear energy observable. For clustered hits < 7000 the different muon tagging systems can't be compared to each other. As can be seen, the system is stable despite some minor fluctuations and two bigger spikes, time correlated to the ones present in figure 5.3. The investigated data spans from the beginning of data taking in May 2007 until the beginning of March 2013.

different ratios are depicted in figures 5.3 - 5.5.

It is visible, that the detector performs good and stable in this regime. There are some fluctuations visible in the MTB and MCR tagging efficiency. These are generated by an unstable Outer Detector. Sometimes, at the end of a run it happened that the electronics of the Outer Detector saturated and, therefore, some events were not detected. In addition, the muon track reconstruction of the Outer Detector sometimes generates problems depending on the hit pattern of the muon event. The two bigger spikes visible in figures 5.3 and 5.4 were generated by an Outer Detector not taking data for a bigger timespan within a run. However, the stability of the IDF shows an excellent behaviour with no fluctuations visible. As for data analysis all three different muon tagging systems are used, the stability and efficiency of muon identification can be regarded to be excellent.

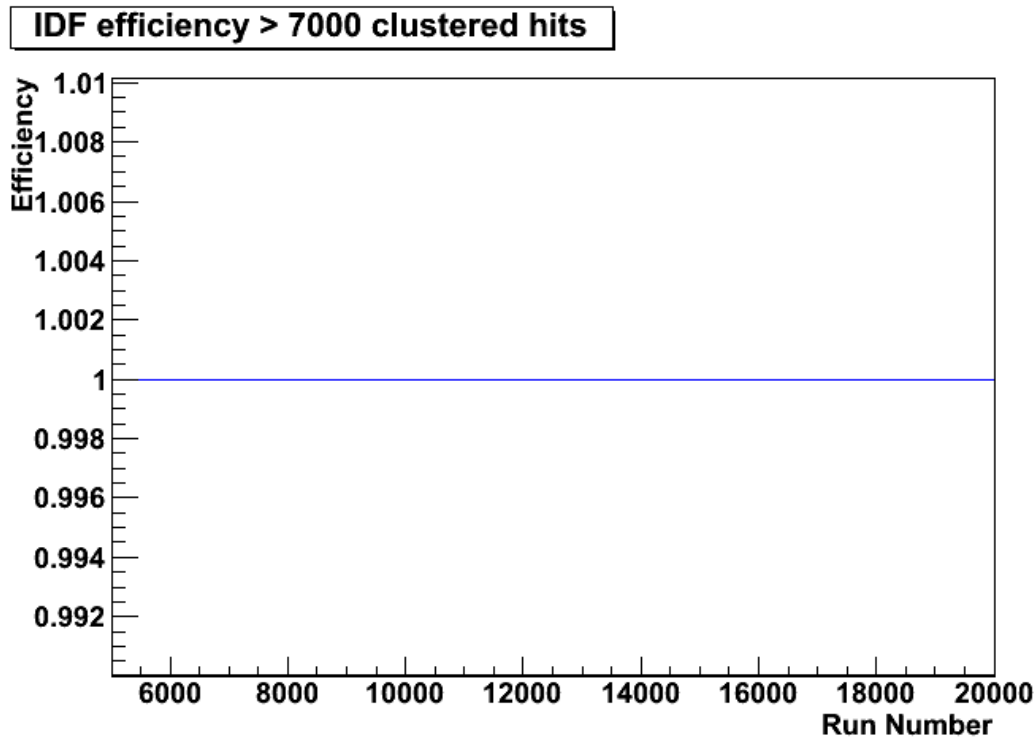


Figure 5.5: Stability and efficiency of the IDF. The sum of muons tagged by the IDF and the MCR is compared to the number of muons tagged by the MCR alone. The variable used to select the energy region of interest is clustered hits, a nonlinear energy observable. For clustered hits < 7000 the different muon tagging systems can't be compared to each other. As can be seen, the system is very stable. The investigated data spans from the beginning of data taking in May 2007 until the beginning of March 2013.

5.2.3 Electronics Simulation (BxElec)

The Borexino detector is a very complex system. In order to verify it is working properly, several components have to be checked and monitored. Some possible methods have already been reported in the previous section. To check the complete system, starting from the event taking place inside the detector until the end of data processing, different Monte Carlo simulations are used. The physical event in the detector, along with the light propagation to the PMTs including all secondary effects like scattering, absorption and reemission, are simulated by a program called G4Bx. It is based on Geant4 [92][93] including specifications for Borexino, like the detector design and the materials used. In order to process this simulated data with the normal data handling program Echidna [91] that was particularly developed for the Borexino project, the simulated data has first to be modified taking two aspects into account. First, the influence of the electronics on the detected signal has to be considered. Second, the data has to be put in a format readable by Echidna. For the Inner Detector both things are done by a simulation program called BxElec. However, for

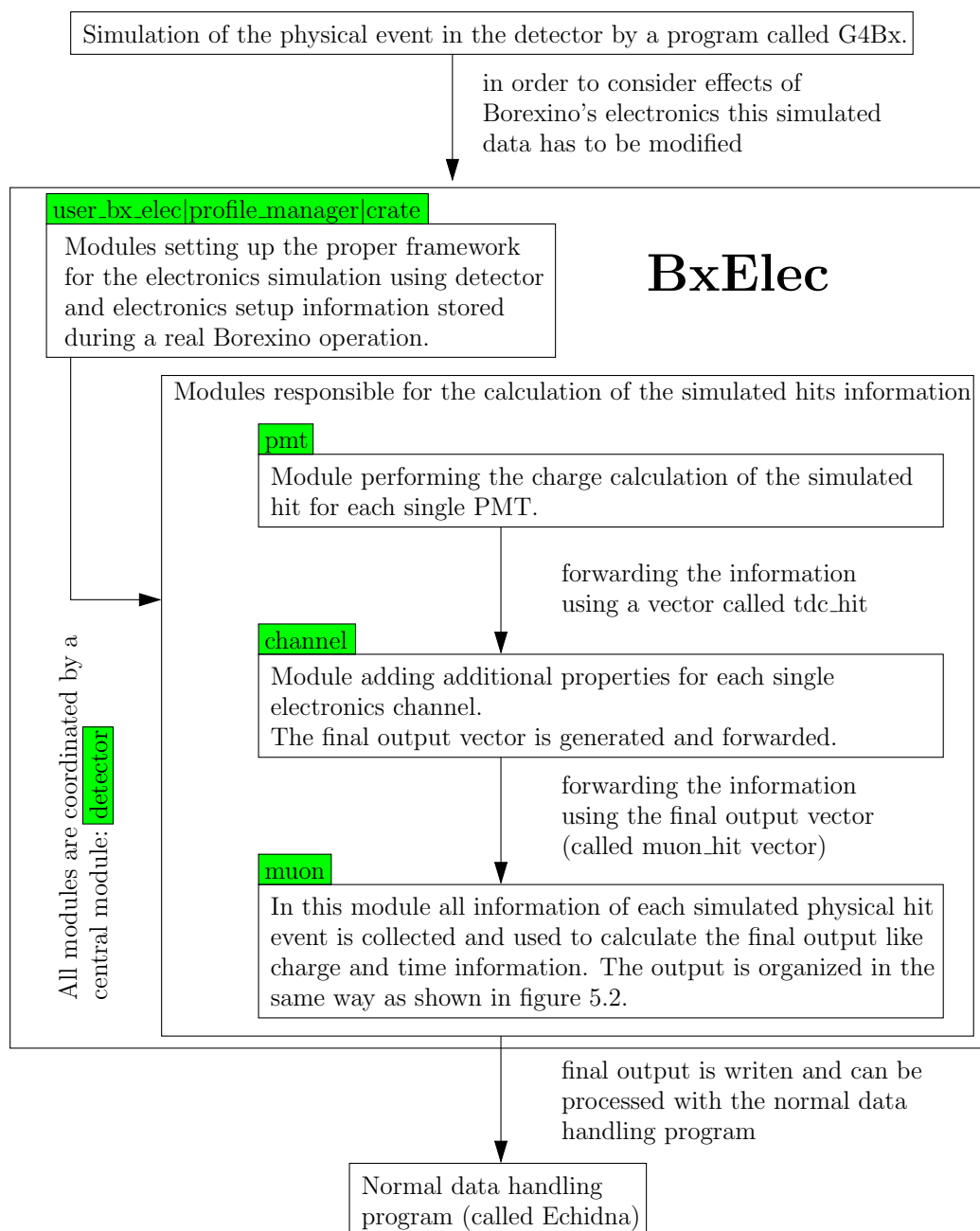


Figure 5.6: Simplified schematic view of the electronics simulation process. In green the name of the different simulation modules are given.

the Outer Detector this tool was not available. Starting within the Diploma thesis [64], the implementation of the electronics of the Outer Detector into the simulation program BxElec is continued as part of this thesis. A simplified schematic view of the electronics simulation process is depicted in figure 5.6. Most of the electronics described in section

5.2.1 have to be considered. An exception is the LED calibration system as a whole. It has no direct influence on the data taking process and can therefore be neglected for the simulation. Most important are the QTC and TDC boards. They are responsible for the calculation of the respective hit time and charge, and generate the final data format, the 32-bit data word (see figure 5.2). Corresponding to these two boards, vectors called `qtc_hit` and `muon_hit`, are introduced in the simulation. They contain the respective hit information that is generated in the electronics and are used to communicate between the different simulation modules as well as the final simulation output:

- **qtc_hit**: It contains information like charge, time and all other essential hit information that is normally produced in the QTC boards. However, the output can't be read directly by Echidna, but has to be transferred first. This behavior is similar to the electronics, as the signal of the OTCs is modified by the TDC boards.
- **muon_hit**: It is the remodeled version of the `qtc_hit` and contains the previous mentioned information of the TDC word. It is build the same way as the final output of the TDC boards, the structure of the final 32-bit data word (see figure 5.2). The contained information can therefore be processed by Echidna.

In the following the main modules of BxElec that are responsible for the Outer Detector electronics simulation, are explained. They are depicted in figure 5.7. In green color all modules generating the proper framework for the simulation are depicted. The modules doing the important calculations of the hit time and charge are illustrated in blue. Different needed getters are provided by the module `hit` depicted in yellow. All parts are merged and controlled in a central construction module `detector` (red color).

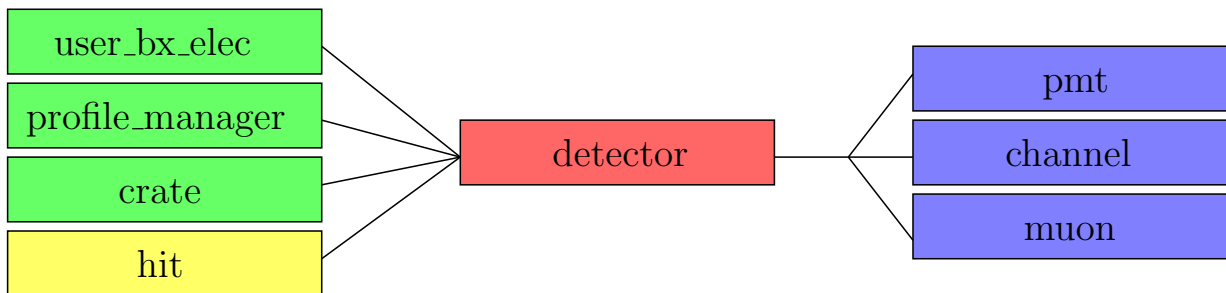


Figure 5.7: Overview of the modules essential for the simulation. In red color, the central construction module merging all data is presented. The modules responsible for the proper framework are depicted in green, whereas the modules doing the important calculations are shown in blue. The module depicted in yellow deploys different getters. An detailed explanation of the different modules is given within the text.

user_bx_elec:

It is a configuration file, meant to adjust the simulation individually to different run conditions. Specifying the run number used for the simulation, the properties for the simulated

electronics are set equal to those present during the real data run with the corresponding run number. Some parameters like dark count rate and different thresholds needed within the simulation can be modified by the user. If only a simulation of the Inner Detector is needed, the Outer Detector can here be switched off in order to increase calculation speed.

profile_manager:

As a first step, the simulation has to be fed with real information on the electronics in order to align it with reality. Each time a real data run is taken, the configuration of the electronics is written into a profile and stored to a database. To adjust the simulation with reality this database has to be read. The profile of a specified run number is then used to replicate the exact electronics behavior for the further steps performed within the simulation. The following different sections and values of a profile are important for the Outer Detector simulation part:

1. *MuonGeneralSetting*: The trigger-status for the so-called Muon Channels of the Outer Detector are set here. It provides information on the status of the different electronics channels (exact definition in the following bullet), whether all were activated for the chosen run or some were shut-off.
2. *MuonChannelMapping*: There are different possibilities an electronics channel can be used for:
 - ordinary channel: normal data is acquired during the run, containing the hit information. One single channel for each PMT.
 - integrity channel: a service or trigger reference channel used for calibration of the electronics.
 - empty channel: channels not activated and containing no data for the present run.

The different channel types are allocated to the respective channel numbers.

3. *MuonPredData*: In the first seconds of a real run, the electronics is calibrated. This information is stored here. An important value for the Outer Detector is the stored pedestal that is needed for the later on charge calculation.
4. *MuonCalibInfo*: Calibrating the PMTs used with the connected LED system, information on charge and time offset are stored here for all PMTs.
5. *MuonHolesMapping*: The information on the spatial position of the PMTs inside the detector is stored here. The channels are allocated to holes with a unique number, the PMTs are mounted in. This information is crucial for the possibility to perform event reconstruction and a muon track reconstruction with the simulated data.

In addition to the just mentioned settings that change for each run, other well-defined values are needed for an aligned simulation mimicking a real run. These further variables

are set in the next two modules, so the simulated events can be compared to real ones at the end.

detector:

This is the central file of the simulation module, the intersection of all used files. In addition, the 216 PMTs of the Outer Detector and the service channels are declared as muon channels and saved into a vector. In total, 256 muon channels are defined. They are arranged in line with the 2240 channels for the Inner Detector, called laben channels. The muon channels can be addressed by the other modules, using the logic channel number starting at 3001. In a similar manner, the vector saving the information of the crates used is extended by the muon crate. In addition, different possible calibration hit types are declared here. In this way, a so-called integrity hit was invented for later usage. Last, the command to write the final data is given, as well as control messages during the simulation itself are generated and printed to screen.

crate:

In alignment with the crates of the Inner Detector, a new crate hosting the muon channels is imposed. A respective delay time is assigned. The crate can be switched on or off in the configuration file `user_bx_elec`. This is similar to the run configuration module of the real data acquisition system. In doing so, all muon channels are enabled or disabled for the simulation performed.

pmt:

This part of the simulation program combines two parts of the electronics chain, the PMTs and the QTC boards. It generates the physical output of the PMTs and, therefore, the primary charge information of the detected hit. The charge of the PMT is calculated by counting the amount of photoelectrons recognized by the PMT. Therefore, a vector is build and filled with the time ordered information of the photoelectrons. In addition, values describing PMT behaviors are set here, particularly the dark count rate. But also values needed to calculate the charge using the amount of collected photoelectrons are defined here, like the gain and the charge raising time of each PMT. A calibration charge is set for the simulation of calibration runs, according to the measured LED pulses. All this information is needed to build the previously mentioned vector `qtc_hit` including the processed charge. In reality, this is performed by the QTC boards, passing the name to the vector. Despite the calculation of the charge, also data describing the boards itself are stored and applied in the vector `qtc_hit`, for example the decay times of the respective boards and the previously mentioned pedestal of the QTC chips. The charge calculation for the muon channels is quite different from the one performed for the Inner Detector. Whereas the laben channels measure the height of the detected charge peak, the QTC boards use the equivalence of charge and time (see the description of the QTC boards in section 5.2.1). The pulses of the PMTs are transferred to a time gate, defined by two variables: the lead-time and the trail-time. They refer to the start-time and to the end-time of the detected hit. Together with the other variables, describing the PMT and QTC board

behavior, those values are saved into the `qtc_hit` vector for later processing. In total, four different charge types can be distinguished:

1. *normal charge*: Refers to a real Borexino operation. The charge is calculated using the gathered information of the photoelectrons collected by the respective activated PMT.
2. *calibration charge*: As previously mentioned, this charge mimics the charge information of the associated LED system, using well-defined values being different than for the normal charge calculation.
3. *integrity charge*: This charge is needed for service only. It has a fixed value that is clearly distinguishable from all other charges. Therefore, an easy identification of all integrity channels is possible later on.
4. *dark charge*: When a PMT does not recognize any hit, there also is a dark count rate present. It is generated by thermionic electrons emitted by the photocathode and the pending dynode current. The dark charge simulates this effect.

Another effect that is considered in this module is the possibility of hit and event separation, respectively. A variable `dt` is introduced to measure the time distance between two recognized hits. Because the QTC boards have a certain decay time after a hit, the value `dt` needs to be bigger than that, in order to distinguish the two hits. If this is not the case, the ongoing hit is discarded and the next one is saved.

channel:

This part of the simulation is responsible for allocating a PMT to the associated electronics channel. The most interesting and important channel type is the ordinary one, as defined and assigned in the `profile_manager`. For this case, as a first step, the channel is filled with dark noise. Later on, the hit information of the PMT, and hence the collected charge information, is added to the respective channel. With those variables the `qtc_hit` vector is finally filled and the respective values of the channels pedestals along with their time offsets are saved and passed to the `muon_hit` vector.

The `muon_hit` itself is treated in a special section of the file. It uses the information delivered by the `qtc_hit`. First of all, the PMT has to be allocated as a so-called muon PMT together with a logic channel number, to make it distinguishable from the Inner Detector channels. The next important step is to check for an existing trigger. If the amount of collected photo electrons together with the respective channel's dark count rate, corresponding to the total detected charge, exceeds a defined threshold, the hit is declared a muon hit. If all of the previously mentioned is the case, the values for the final output, corresponding to the 32-bit word, are then generated in a file called `muon`. The dependency of the `qtc_hit` and `muon_hit`, along with the most important involved files and values, is depicted in figure 5.8.

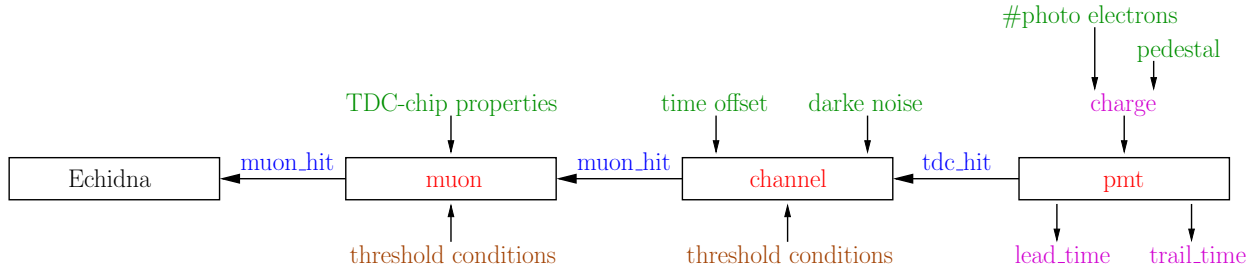


Figure 5.8: Schematic view of the main parts of the simulation program BxElec for Borexino's Outer Detector electronics. The boxes represent the most important, modified and new modules (red). In blue color the respective output of the different modules is depicted. Green are input data that are used to calculate certain needed values (magenta). Depicted in brown are certain conditions that have to be complied with.

muon:

All essential parts of the final 32-bit word (see figure 5.2) are generated in this module. The main task is to organize the hit information in a way it can be accessed by Echidna later on. Therefore, the structure of the simulated information must be comparable to the one of the TDC boards. The main information is set in the variables `lead_edge` and `trail_edge`. The charge information of the channels is used altogether with all the other timing values and TDC-chip properties to build the correct values. In addition, it is important to distinguish the channels, processed by the two TDC-boards and the respective four TDC-chips. Using the integrity channels and their charge information, this can be done, as they are clearly distinguishable from the ordinary channels. The final `muon_hit` is saved. It contains now the information of the respective channel meaning the channel number itself and the `lead_edge` or the `trail_edge` information. The output format is similar to the final 32-bit word of the TDC-boards (depicted in figure 5.2) and can therefore be processed like real data with Echidna.

hit:

A file containing getters to provide the `qtc_hit` and `muon_hit` vector with the needed data. In contrast to the Inner Detector simulation, the `lead_time` and `trail_time` variable are used here to build the output format of the final `muon_hit`. The TDC word is defined and generated. The values of the needed variables are obtained by the module `muon`.

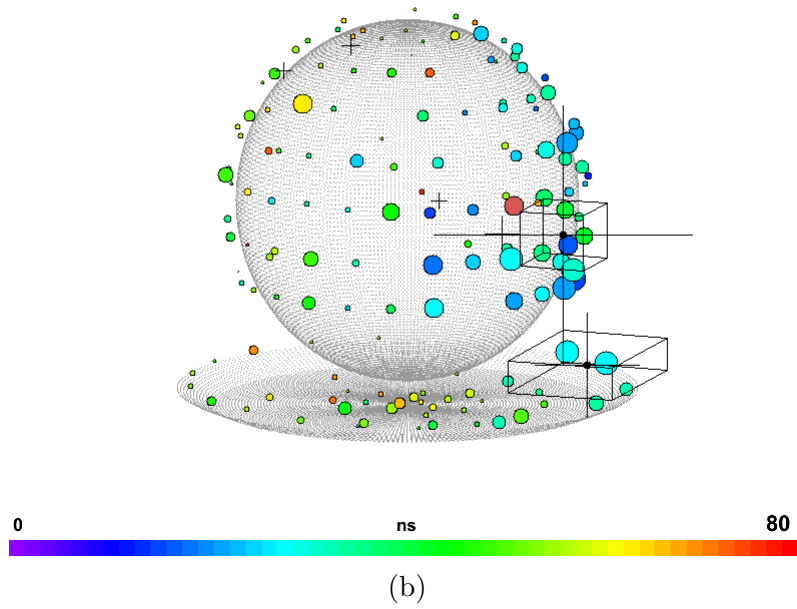
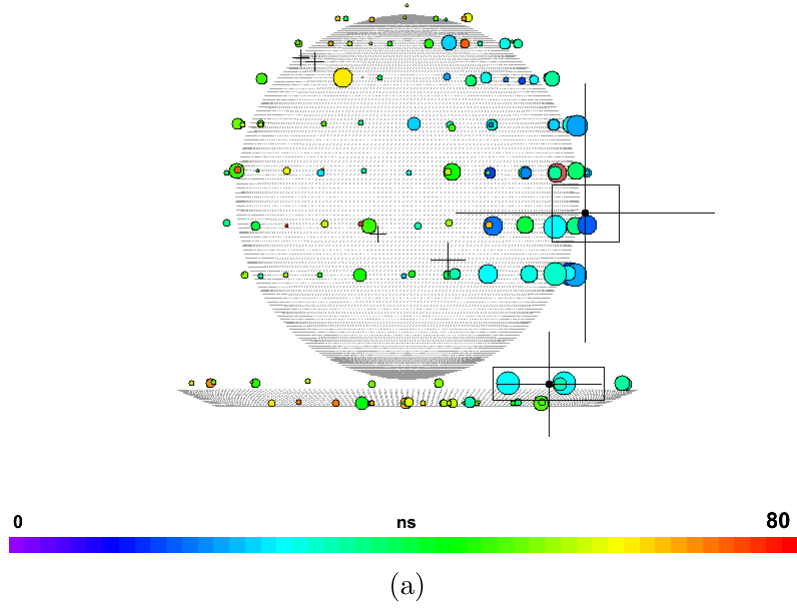
In addition to the above explained modules, other files had to be edited to allow the needed data handling and interfile communication. This includes the modification of different parsers and the modification of files responsible for different timing configurations. Still missing, and not part of the present thesis, is the development of a stand-alone trigger for the Outer Detector simulation, as it has not yet been decided by the collaboration to include such a trigger module. At the moment, the outer system is just evaluated when there is a trigger generated in the Inner Detector. This may lead to problems in the hit-time pat-

tern of the Outer Detector simulation and, therefore, to difficulties in data reconstruction. In addition, the simulation tool G4Bx has problems handling muons crossing the Inner Detector volume due to the high light yield and the big amount of produced secondaries. In any case, the Outer Detector simulation is now working and can be used to test the Outer Detectors behavior, as will be shown in the next section.

5.2.4 Outer Detector Performance

Originally, the calibration tools were designed to test and validate the detector and, hence, the taken data. But also modules of the data processing system Echidna can be tested. One of the main purposes of the simulation for the Outer Detector is to test the muon track reconstruction. But because of the still missing trigger module, the results of the Outer Detector simulation have to be regarded with care. In order to test the system, muons crossing the Inner as well as the Outer Detector have to be simulated with G4Bx. In the simulations, the point of origin is located in the middle of the Borexino detector. All coordinates refer to this point. In the following, the observed muons are generated at a height of 15 m and an offset of 5 m to a randomly picked side, as the detector is spherical. Their energy is set to 100 GeV. The flight direction is oriented downwards. To rule out side effects that could originate in a special run setup, two different and independent run setups are used for the electronics simulation. The two data samples are processed with BxElec including an activated Outer Detector module. Afterwards, the gained data samples are treated regularly by Echidna. The final data sets are used to validate the muon track reconstruction. The results are shown in figure 5.9 for run number 11000 and in figure 5.10 for run number 14977, respectively. Depicted is a schematic view of the Stainless Steel Sphere and the bottom of the Outer Detector, that are equipped with PMTs. The colored circles represent the detected charge, indicated by the diameter. The coloring represents the timing of the respective hit related to the trigger signal in ns. The two black boxes are the reconstructed entry and exit clusters of the simulated muon. The black line in figure 5.10 represents the reconstructed muon track. It is obvious that there are problems concerning the muon track reconstruction using data simulated for the Outer Detector. But this is not caused by the reconstruction module, but by the simulation itself. The still missing trigger results in a wrong time distribution of the hits, whereas the hit distribution itself is already good. However, for the hit patterns depicted in the to figures 5.9 and 5.10 including the wrong hit time distribution, the muon track reconstruction works. Until now, no evidence is found to doubt the procedure of the muon track reconstruction of the Outer Detector.

So far, as a conclusion of this chapter it can be said that the Outer Detector shows a good time stability and the detection efficiency of muons is very satisfactory. There are no hints to doubt the overall muon detection efficiency of the combined different systems of 99.992%, as cited in [94]. Also the track reconstruction seems practicable.



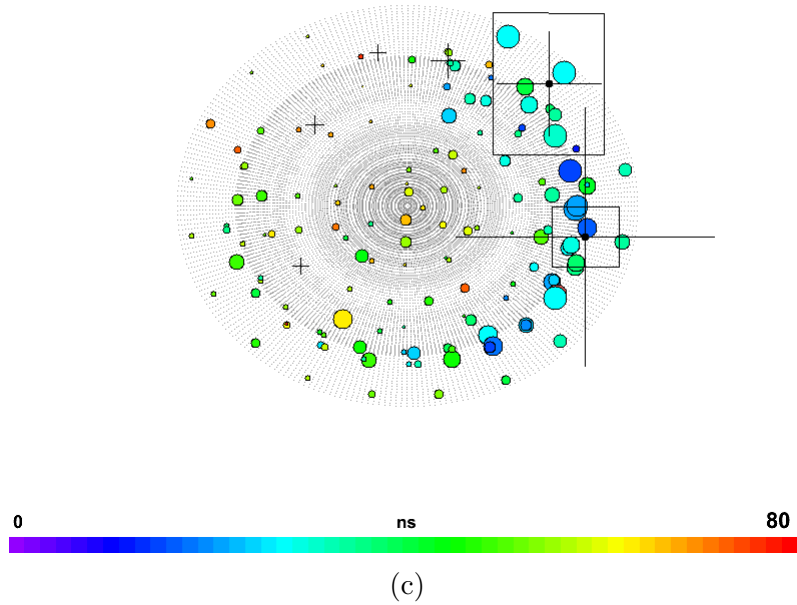
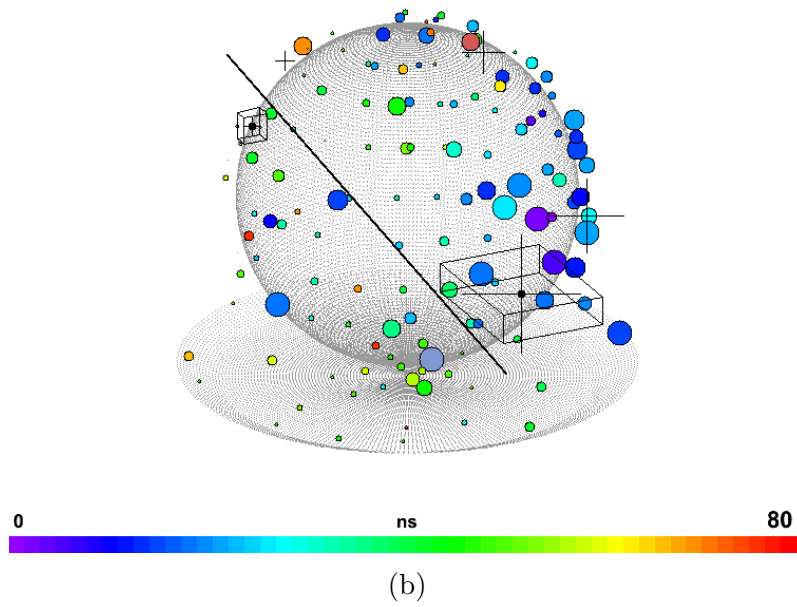
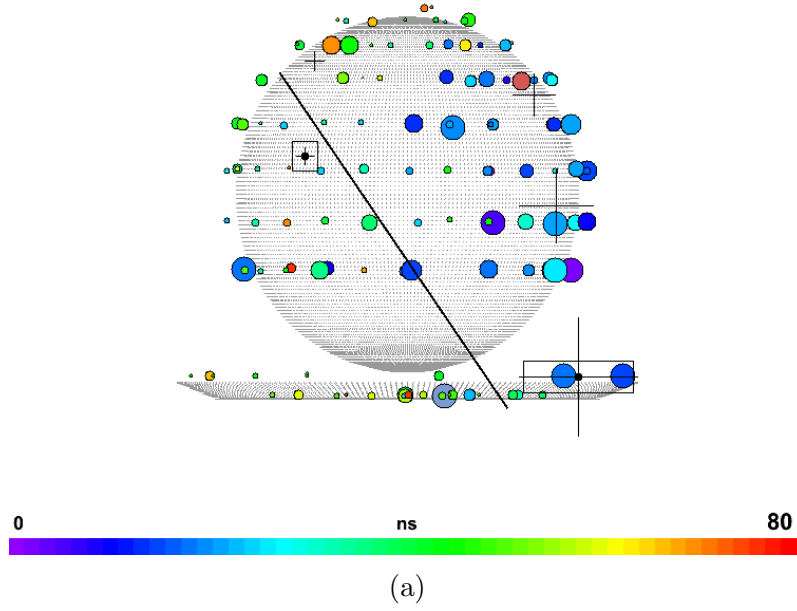


Figure 5.9: Muon track reconstruction of simulated data including BxElec for run number 11000. Shown is the schematic view of the Stainless Steel Sphere and the bottom of the Outer Detector, that are equipped with PMTs. Simulated is a muon crossing the detector vertically with an energy of 100 GeV and a distance of 5 m to the detector center. In (a) the detector is regarded from the side, in (b) from diagonal above and (c) depicts the detector directly from above. The colored circles represent the detected charge, indicated by the diameter. The coloring indicates the timing of the respective hits relating to the trigger in ns. Though the reconstruction of the entry and exit cluster of the muon succeeds (represented by the two black boxes), the reconstruction of the resulting muon track fails nevertheless because of a misleading timing information. The problem is aroused due to a still missing Outer Detector trigger in the simulation.



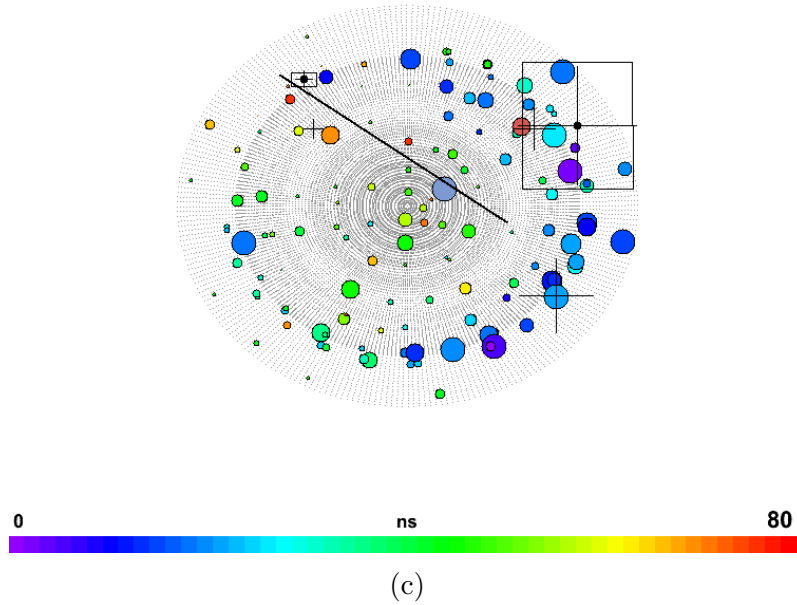


Figure 5.10: Muon track reconstruction of simulated data including BxElec for run number 14977. Shown is the schematic view of the Stainless Steel Sphere and the bottom of the Outer Detector, that are equipped with PMTs. Simulated is a muon crossing the detector vertically with an energy of 100 GeV and a distance of 5 m to the detector center. In (a) the detector is regarded from the side, in (b) from diagonal above and (c) depicts the detector directly from above. The colored circles represent the detected charge, indicated by the diameter. The coloring indicates the timing of the respective hits relating to the trigger in ns. The two black boxes are the reconstructed entry and exit clusters. Though the two clusters are not located at their expected places due to the wrong hit time information, compared to figure 5.9 the track reconstruction succeeded. The result is given by the black line. The misleading time distribution of the reconstructed hits results in a track reconstruction that is tilted sideways. The problem is aroused due to a still missing Outer Detector trigger in the simulation.

5.3 CNGS-Beam induced Neutrons

The Borexino detector shares an experimental hall with the Opera detector [95] in the LNGS underground laboratories. Hence, there is the possibility to observe the pulsed neutrino beam generated in CERN and send to Gran Sasso, the so-called CNGS-beam [95][96]. Originally designed for the first detection of neutrino oscillations in direct appearance mode by observing the ν_μ to ν_τ transition, it also offers the possibility for Borexino to use the beam for means of calibration. At the LNGS, the neutrino beam arrives with an incline of 3.5° below the horizon, corresponding to a zenith angle of 93.5° . Its width is more than one kilometer. With the well defined beam orientation, muon track reconstruction can be tested for horizontal muon tracks. As the mean neutrino energy of the beam is about 18 GeV and the mean energy of the induced muons is about 16 GeV, these muons are low in energy compared to cosmic ones with a mean energy of 280 GeV and, therefore, can give a glance to lower-energy neutron production. This will be discussed in the present chapter. In addition, the speed of neutrinos was determined as a cross check to the results obtained by the Opera experiment (see section 6.1.5).

5.3.1 Data Selection

To identify events induced by the neutrino beam, a time coincidence is set up between the beam generation at CERN and its detection at Borexino. The time-correlated events are then tagged as CNGS events and can in later analysis be distinguished from normal events. The beam is not present all the time, but just for some few weeks in a row. In 2012 the beam parameters were changed and a new timing system was installed in order to achieve better timing coincidences. For the analysis in the present thesis, only data taken before those changes is considered. With a fully operational detector starting measurements in May 2007, a data sample of approximately 163000 events is used. The different runs and their respective event number are depicted in figure 5.11. The data files used are also dst files, as already described in section 5.2.2 and, therefore, already cleaned of all ^{14}C background events. Nevertheless, a lot of remaining unwanted events are present in the data sample. Different cuts have to be applied to reduce the sample to the wanted muons and their secondary neutrons. The cuts used are explained in detail in the next section.

5.3.2 Applied Cuts

This section explains the different cuts applied to reduce the data sample to a trustworthy one for CNGS neutron analysis. As a first step, and just for cross-checking, the data sample is again searched for ^{14}C background events. Therefore, an energy cut corrected with the amount of live PMTs is used. Furthermore, it has to be assured that the regarded muons are all through-going ones related to the Inner Detector, in order to rule out effects due to muon decay in the sensitive volume. Therefore, several cuts are applied based on visible energy and reconstruction of muons in the Inner and the Outer Detector. Also considered is the relative timing of the two independent detectors. The following is a collection of the

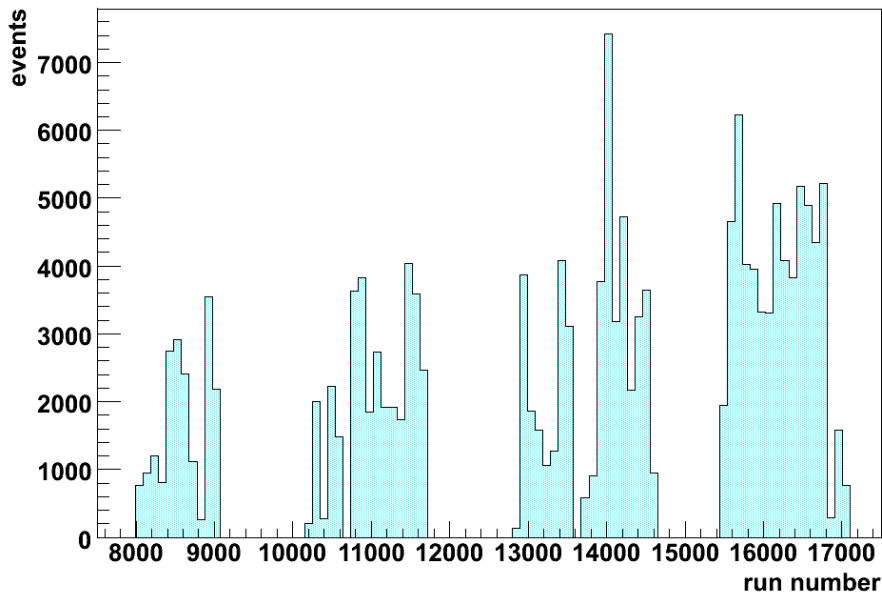


Figure 5.11: Data sample used for the CNGS neutrino beam induced neutron production analysis, ranging from May 2007 to the end of 2011.

applied cuts:

- selection of muons crossing the IV:
 - visible energy greater than 300 MeV
 - impact parameter below 4.25 m
- Muon track alignment (ID):
 - reconstructed zenith angle between 78° and 107° .
 - x coordinate of entry point (EP) greater than 6.0 m (facing towards CERN)
 - x coordinate of exit point (XP) smaller than -6.0 m (facing away from CERN)
- Timing cuts (ID&OD)
 - first OD signal followed by ID signal within 30–60 ns (expected delay is 43.5 ns)
 - maximum difference between OD EP and XP time coordinate of 64 ns

The angular distribution of the remaining muons is shown in figure 5.12, corresponding to approximately 1,800 tracks. It is in good agreement with the expected zenith angle of 93.5° , that is stated at the beginning of section 5.3. For further analysis, the mean muon path length in the Inner Vessel of the detector has been determined to (8.12 ± 0.14) m by the Inner Detector track reconstruction.

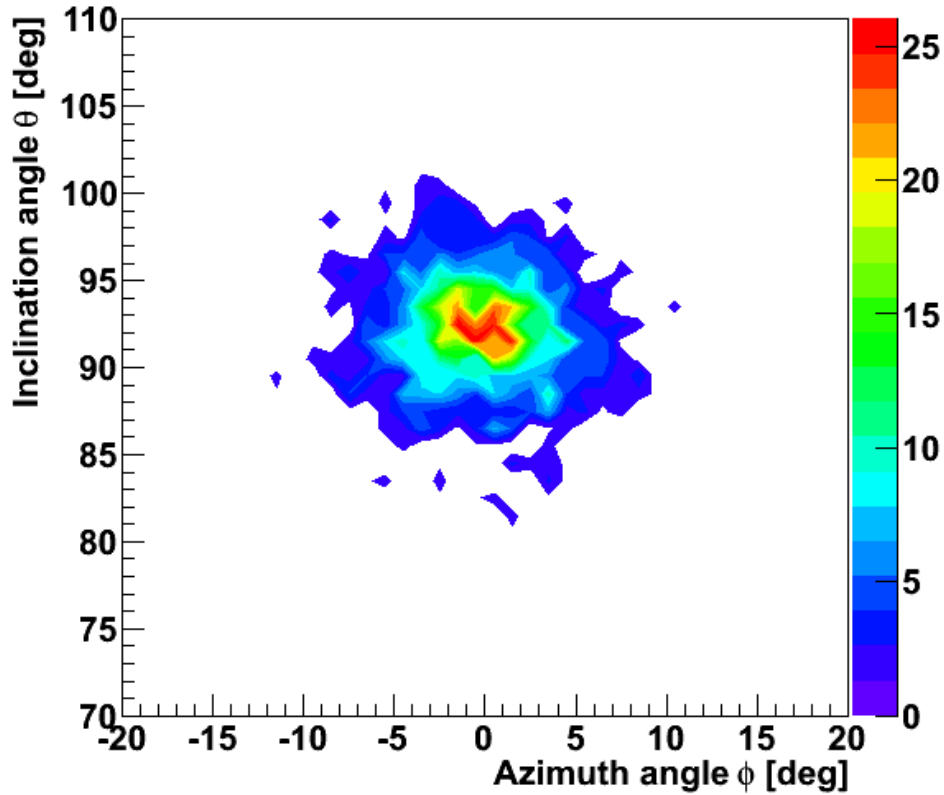


Figure 5.12: Angular distribution of the remaining CNGS muons after all applied cuts. It is in good agreement with the expectation of 93.5° .

5.3.3 Neutron Multiplicity

Each single detected muon event that has passed all applied cuts, is searched for produced neutrons. Before counting the registered amount of neutrons, the corresponding neutron sample again is cleaned by a ^{14}C -cut (see previous sections). The systematic error of the neutron rate is determined to be less than 4% by varying the different applied cuts. Compared to the statistical error of $\sim 30\%$ it is very small and can be neglected in the following. Referred to the number of selected CNGS muon events, the neutron rate is $(0.063 \pm 0.023) n/\mu$. The neutron multiplicity distribution is depicted in figure 5.13. Normalized to the muon track length, the neutron rate is determined to $(6.8 \pm 2.6) \cdot 10^{-5} n/(\mu \cdot (\text{g}/\text{cm}^2))$.

Compared to values in the range of $\approx 4 \cdot 10^{-5} n/(\mu \cdot (\text{g}/\text{cm}^2))$ generated by simulations [97] using FLUKA [98][99], the results are approximately factor 2 higher than expected but still in the right order of magnitude and in accordance considering errors. As an explanation for

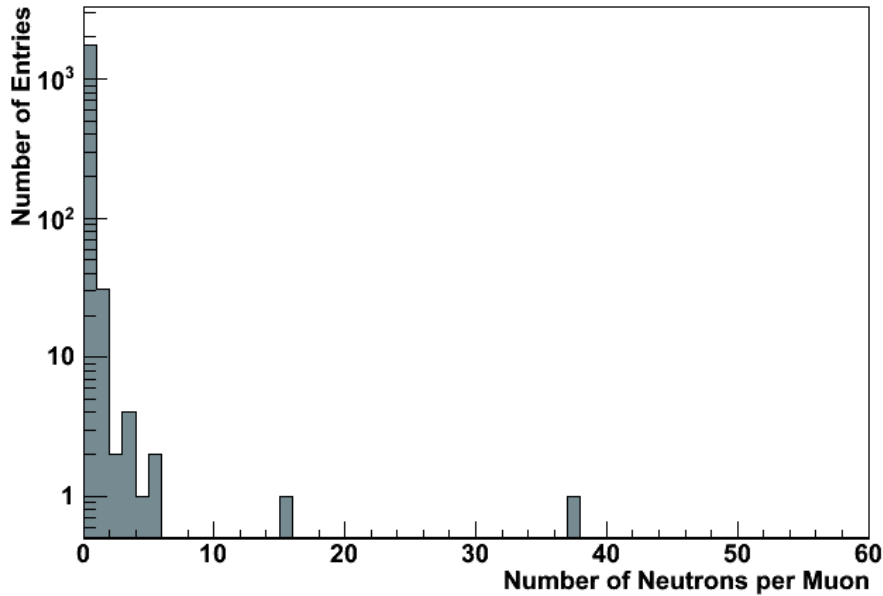


Figure 5.13: Neutron multiplicity for CNGS muons. The neutron rate is determined to $(0.063 \pm 0.023) n/\mu$.

this divergence between the CNGS beam induced neutron production rate and simulations a misinterpretation of the simulated data is considered [100].

Although the simulation seems credible for higher energy regions, as it is in good agreement with data for cosmic muons [101], there is a diversity of approximately 20% for the high-energy muons [102]. Again the simulated rate is lower than the experimental one. The misinterpretation of the taken data in reference to the simulated data is in ongoing investigation. The simulation still might not consider some hadronic components of the beam correctly or they could still be completely missing [100]. These may also penetrate the detector and could be able to generate additional neutrons there. Thus, the neutron multiplicity could increase. Therefore, future modifications concerning the simulation are scheduled.

Chapter 6

BOREXINO Results and Prospects

As stated in chapter 1, there is a big variety of physics that can be investigated with neutrinos. The Borexino experiment has the great possibility to measure some of these neutrinos and, therefore, can test some of the different theoretical models. The detector started to measure with a fully operational detector in May 2007 and still continues to take data. The results achieved so far by the Borexino collaboration are collected in section 6.1. But of course there are still open questions investigated by the collaboration. An overview of these prospects is presented in section 6.2. Being part of the collaboration, the work presented within this thesis contributes directly to the so far achieved results and also to the future perspectives.

6.1 BOREXINO Results

6.1.1 ^7Be Neutrinos

Borexino was designed especially for the low-energy spectrum of solar neutrinos. It was the first experiment to measure ^7Be neutrinos in real-time [103]. Gaining more statistics over time, a high precision measurement of the neutrino rate and flux was reported in 2011 [104] using a total fiducial exposure of 153.6 ton·yr for the analysis.

The energy region of interest is set to 290 - 1270 keV because the shoulder of the mono-energetic ^7Be neutrinos is expected at a recoil energy of 660 keV (compare figure 1.4). The final spectrum, after an applied muon cut, a fiducial volume cut, after removing the ^{214}Bi - ^{214}Po coincidences and a statistical subtraction of the remaining ^{210}Po α -events is depicted in figure 6.1. To obtain the ^7Be neutrino rate, an analytic fit is applied to the remaining spectral components, including the persisting background generated by ^{85}Kr , ^{210}Bi , ^{11}C , and a fixed combined rate of pp, pep and CNO neutrinos. It results in a ^7Be neutrino rate of 47.0 ± 1.9 counts/(day · 100 ton).

As a second possibility, a Monte Carlo based fit is applied to the same data sample, producing a rate of 45.5 ± 1.5 counts/(day · 100 ton) for the ^7Be neutrinos. Combining both methods, a final rate of $46.0 \pm 1.5(\text{stat})_{-1.6}^{+1.5}(\text{syst})$ is obtained, corresponding to a flux

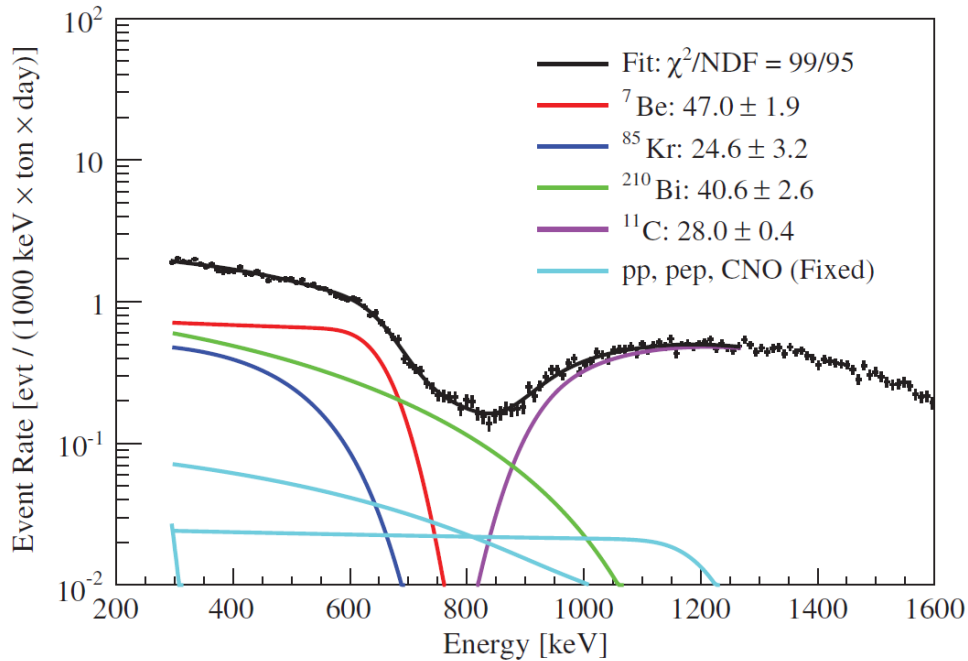


Figure 6.1: ${}^7\text{Be}$ neutrino spectrum as recorded by Borexino, with cuts removing the ${}^{214}\text{Bi}$ - ${}^{214}\text{Po}$ coincidences already applied and a statistical subtraction of the remaining ${}^{210}\text{Po}$ α -events. The results of the analytic fits to the different contributions to the spectrum are given in units of counts/(day \cdot 100 ton). The picture is taken from [104], *reprinted with permission from APS*.

of $(3.10 \pm 0.15) \cdot 10^9 \text{ cm}^{-2} \text{ s}^{-1}$. Using these values, the no oscillation hypothesis can be ruled out at a 5σ level.

6.1.2 ${}^8\text{B}$ Neutrinos

All other experiments before Borexino were just able to identify ${}^8\text{B}$ neutrinos with energies higher than 5 MeV in real-time, due to their thresholds. Therefore, the next aim for the Borexino collaboration was to determine the rate and flux of those ${}^8\text{B}$ neutrinos even for lower energies down to 3 MeV in real-time. The results presented here use 488 live days of data for analysis. A detailed explanation of the analysis can be found in [90].

The first cuts applied are similar to those mentioned in section 6.1.1. Due to the higher energy window observed for this analysis, more cuts are needed in addition. To remove cosmogenic background, a 6.5 s veto cut for the total fiducial volume is applied after each muon observed in the Inner Detector. That way most of neutrons generated in the Inner Detector are rejected. Neutrons that are originated by muons just traversing the Outer Detector are vetoed by applying a 2 ms cut after each of these muons. The crucial background originated by the $\beta\gamma$ -decays of ${}^{208}\text{Tl}$ can be subtracted statistically. The remaining data

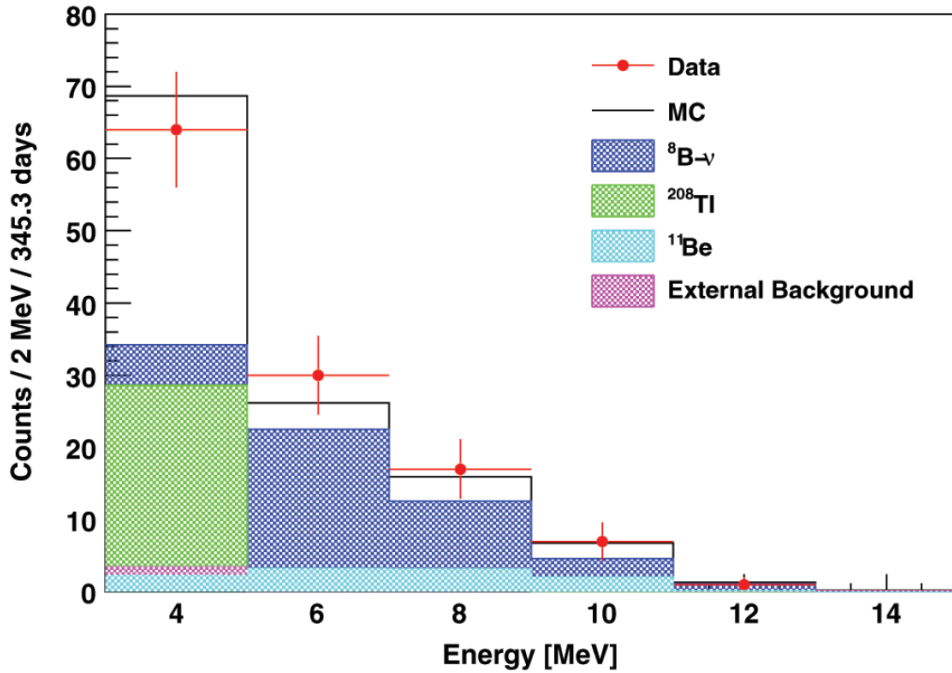
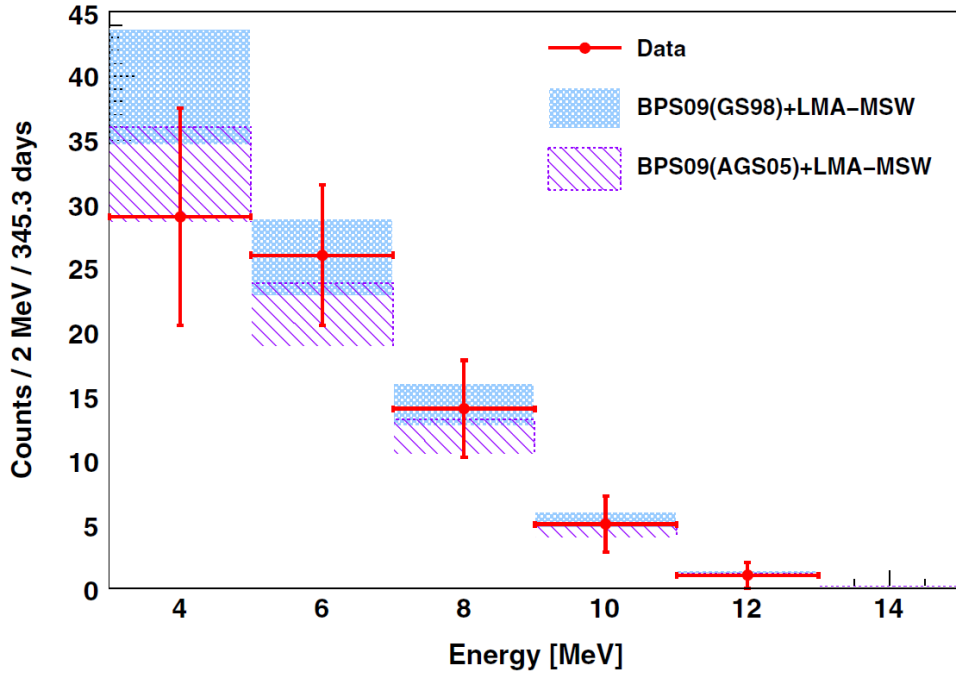


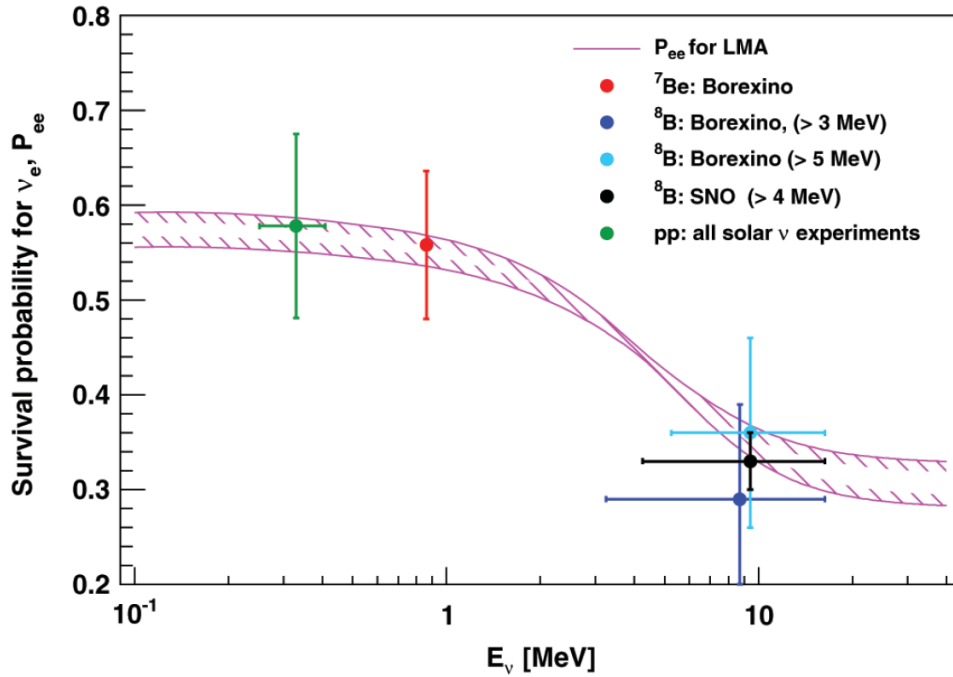
Figure 6.2: ${}^8\text{B}$ neutrino spectrum as recorded by Borexino, with cuts removing the ${}^{214}\text{Bi}$ - ${}^{214}\text{Po}$ coincidences already applied and a statistical subtraction of the remaining ${}^{210}\text{Po}$ α -events. In addition, a 6.5 s time veto after each muon entering the Inner Detector is applied along with a 2 ms veto cut for muons just detected in the Outer Detector. Last, the $\beta\gamma$ -decays of ${}^{208}\text{Tl}$ are subtracted statistically. The red dots represent the taken data points, compared to a Monte Carlo simulation (black line). The respective contributions of simulated ${}^8\text{B}$ neutrinos and simulated different background signals are depicted by the colored areas. The data is in agreement with the simulation. The picture is taken from [90], *reprinted with permission from APS*.

sample consists of 345.3 live days. The spectrum finally achieved is shown in figure 6.2. The red dots represent the taken data points, that are compared to a Monte Carlo simulation (black line) consisting of ${}^8\text{B}$ neutrinos and the different background signals, depicted by the respective colored areas. The final value obtained for the ${}^8\text{B}$ neutrino rate is $0.22 \pm 0.04(\text{stat}) \pm 0.01(\text{syst})$ counts/(day \cdot 100 ton) corresponding to a flux of $(2.4 \pm 0.4 \pm 0.1) \cdot 10^6 \text{ cm}^{-2}\text{s}^{-1}$. These values are in good agreement with measurements performed by SNO [105][106][107] and SuperKamiokande [108][109].

The final spectrum of the ${}^8\text{B}$ neutrinos is depicted in figure 6.3a and is compared to two Monte Carlo simulations. For the simulation different models using high and low metallicity as well as the MSW-LMA neutrino oscillation [110] are used. With this measurement, Borexino is the first experiment able to measure neutrinos of the low-energy vacuum-dominated and the high-energy matter-enhanced regions at the same time. The electron neutrino survival probability is plotted in figure 6.3b. The dots represent the measure-



(a)



(b)

Figure 6.3: (a) The final spectrum of ^8B neutrinos with all cuts applied. The measured data is compared to two Monte Carlo simulations, denoted by the colored areas, using input parameters from models using high and low metallicity in addition to the MSW-LMA neutrino oscillation model [110].

(b) Electron neutrino survival probability as a function of the neutrino energy E_ν , with dots marking the measurements of different experiments. The shaded area depicts the electron neutrino survival probability assuming the BPS09(GS98) standard solar model [34] and the MSW-LMA solution.

Both plots are taken from [90], *reprinted with permission from APS*.

ments of different experiments, including Borexino. The shaded area depicts the electron neutrino survival probability assuming the BPS09(GS98) standard solar model [34] and the MSW-LMA solution. The measured data points are consistent with the prediction of the MSW-LMA solution.

6.1.3 pep Neutrinos and CNO Neutrino Limit

A further aim of the Borexino experiment is a direct measurement of the survival probability of electron neutrinos in the transition region between vacuum-dominated and matter-enhanced regions. An interesting probe, never been directly measured before, is the pep neutrino.

A data sample taken between January 2008 and May 2010, corresponding to a fiducial exposure of 20409 ton · day, is used for the analysis (see [111] for a detailed description). Despite applying the cuts mentioned in the last two sections, a crucial background remains, cosmogenic ^{11}C . A coincidence is used to veto these events. This so-called three-fold coincidence (TFC) veto uses the correlation between the track of the incident muon and the capture of the ^{12}C knock-out neutron. The functionality is demonstrated in the top of figure 6.4. Applying an additional pulse shape analysis and removing all other best-fit rates, the pure pep neutrino spectrum remains, as shown in the bottom of figure 6.4. With ^8B and pp neutrino rate fixed to the rate predicted by the SSM, the best fit produces a pep neutrino rate of $3.1 \pm 0.6_{\text{stat}} \pm 0.3_{\text{syst}}$ counts/(day · 100 ton) with an upper limit of the CNO neutrino rate determined to 7.9 counts/(day · 100 ton) at a 95% confidence level. The correlation between the fit of the pep and CNO neutrino rate is depicted in figure 6.5a. Assuming a non-neutrino flavor-oscillating model, one would expect a pep neutrino rate of (4.47 ± 0.05) counts/(day · 100 ton). This hypothesis can be ruled out at a 97% confidence level, leading to a survival probability of $P_{ee} = 0.62 \pm 0.17$ at 1.44 MeV. Figure 6.5b shows this new value as the first directly measured survival probability in the transition region in combination with the previous determined ones.

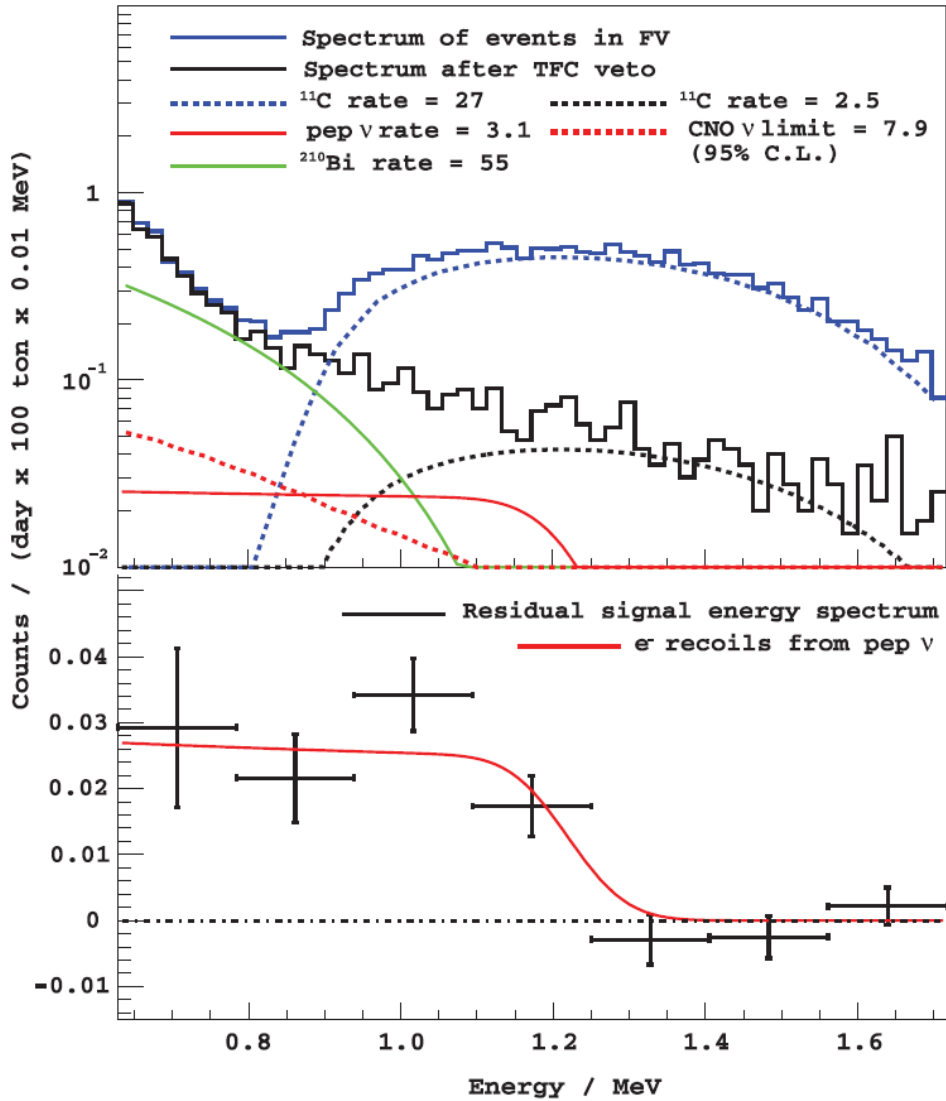
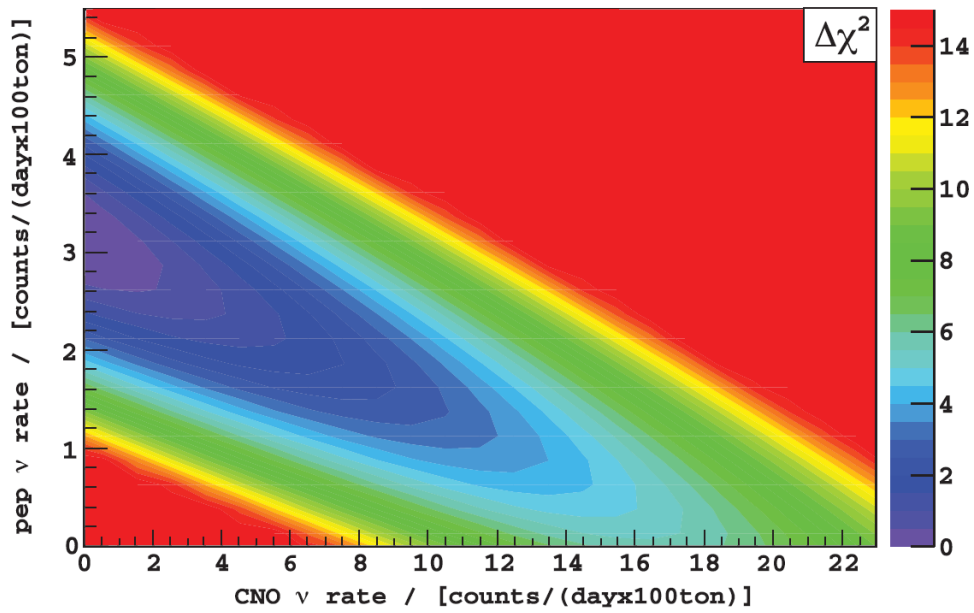


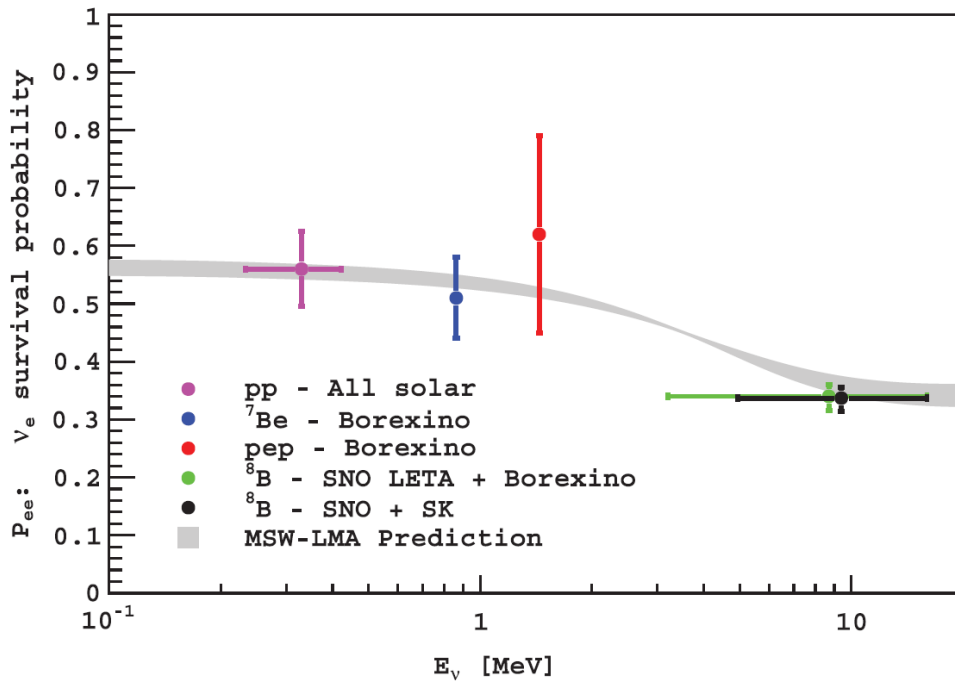
Figure 6.4: Top: Recorded spectra inside the fiducial volume before (blue line) and after (black line) applying the TFC veto. In addition, the best estimates for the pep neutrino are shown as well as the still remaining background from ^{210}Bi . The CNO rate is an upper limit determined by the analysis. The values in the legend are given in units of counts/(day \cdot 100 ton).

Bottom: Final spectrum of the remaining pep neutrino events (black) after application of all cuts, an additional pulse shape analysis and the removal of all other best-fit rates. For comparison, the best fit for the pep neutrino rate is shown, too.

The picture is taken from [111], *reprinted with permission from APS*.



(a)

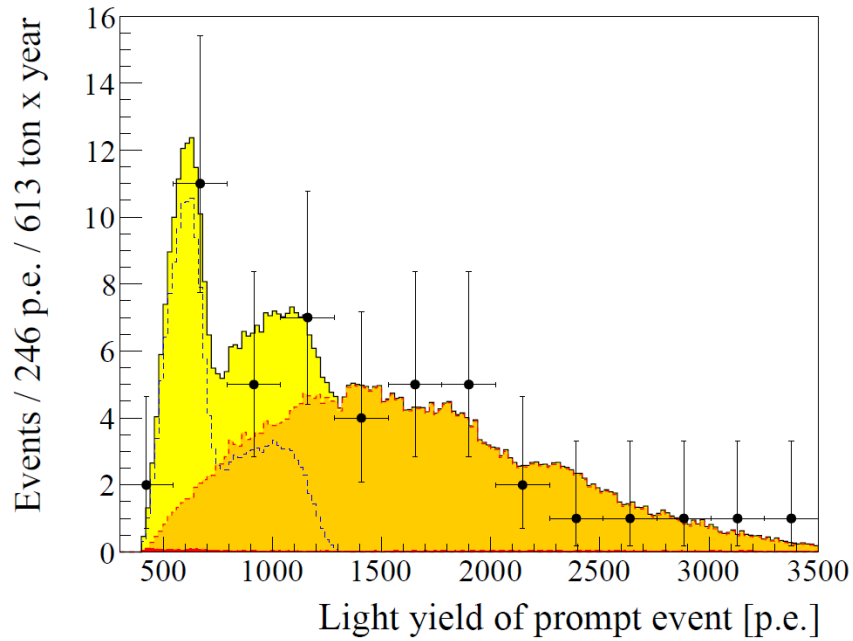


(b)

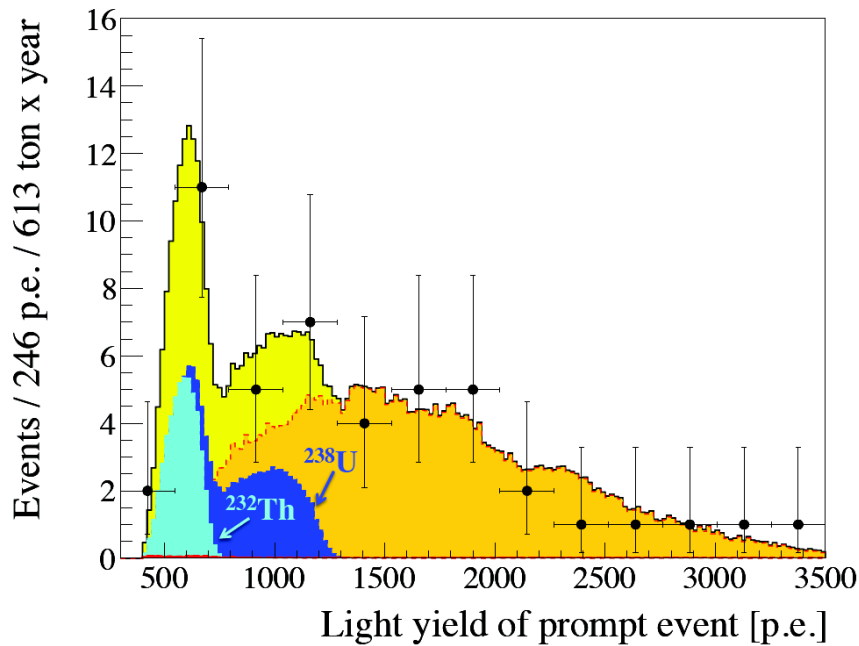
Figure 6.5: (a) $\Delta\chi^2$ -profile of the pep and CNO neutrino interaction rate for different fixed values and the best-fit. (b) Electron neutrino survival probability with the new pep neutrino result in the transition region. The pictures are taken from [111], *reprinted with permission from APS*.

6.1.4 Geoneutrinos

As Borexino is also sensitive to the detection of antineutrinos, analyses regarding geoneutrinos (see section 1.5) are performed. A first analysis was presented in 2010 [112] with an update in 2013 [113] using 1352.6 live days of data. As a first selection, the cuts explained in the previous chapters are applied in order to reduce background signals. As geoneutrinos are measured via the inverse neutron beta decay, $\bar{\nu}_e + p \rightarrow e^+ + n$, coincidences between the captured neutron and positron can be used in addition to confine on wanted events. The positron is detected first and, therefore, is referred to as prompt signal, whereas the neutron candidate is named delayed. The energy of the respective signals has to be $Q_{\text{prompt}} < 408 \text{ p.e.}$ and $860 \text{ p.e.} < Q_{\text{delayed}} < 1300 \text{ p.e.}$, where the unit p.e. (photoelectrons) corresponds to approximately 2 keV. Next, a spatial coincidence cut can be applied. The two events, prompt and delayed signal, have to be reconstructed in a maximal distance of $\Delta R < 1 \text{ m}$ to each other because of the diffusion length of the neutron. Last, a time coincidence cut is used. The two events have to be detected in a $20 \mu\text{s} < \Delta t < 1280 \mu\text{s}$ time window due to the neutron capture time. With all cuts applied, the fiducial exposure was reduced to $(613 \pm 26) \text{ ton} \cdot \text{year}$. In total, 46 antineutrino candidates survived all cuts, including an expected still prominent background of $0.70 \pm 0.18 \text{ events}$. The best fit value for geoneutrinos of $N_{\text{geo}} = (14.3 \pm 4.4) \text{ events}$ and for reactor antineutrinos of $N_{\text{react}} = 31.2_{-6.1}^{+7.0} \text{ events}$ is shown in figure 6.6a. For the fit, a fixed chondritic mass Th/U ratio of 3.9 is assumed. In a second fit approach, this ratio was regarded as a free parameter. The best achieved fit results are $N_{\text{Th}} = 3.9 \pm 4.7 \text{ events}$ and $N_{\text{U}} = 9.8 \pm 7.2 \text{ events}$, depicted in figure 6.6b. The probability for the absence of a geoneutrino signal is $6 \cdot 10^{-6}$. In addition, the measurement of the reactor antineutrino events of $N_{\text{react}} = 31.2_{-6.1}^{+7.0}$ fits expectations taking neutrino oscillations into account.



(a)



(b)

Figure 6.6: Light yield spectrum of the 46 antineutrino candidates (black data points) with the best fit (colored areas). The yellow area depicts the contribution of geoneutrinos to the total signal. The dashed red line, fencing the orange area, shows the part of reactor antineutrinos. The contribution of still persisting background is demonstrated by the red line at the bottom of the figure. 500 p.e. correspond to approximately 1 MeV.

(a) The dashed blue line gives the best fit result for the geoneutrino signal, assuming a fixed chondritic mass Th/U ratio of 3.9.

(b) The fit with a free chondritic mass Th/U ratio results in a contribution of ^{238}U and ^{232}Th , as demonstrated by the blue and cyan colored areas, respectively.

The pictures and values are taken from [113], *reprinted with permission from Elsevier*.

6.1.5 Neutrino Velocity Measured with the CNGS-Beam

There had been great confusion when the OPERA Collaboration reported a velocity measurement of neutrinos being faster than light [114]. Although this result was withdrawn in 2012 [115], other experiments were motivated to test those results. As Borexino is using the same beam as OPERA, it was decided to do a neutrino speed analysis. Therefore, a new timing and GPS system was installed to achieve a better timing resolution. In addition, the distance of the Borexino detector to the CNGS proton target, where the neutrino beam is generated, was determined by a geodetic investigation using GPS. An exact position of the institute itself and the localization of Borexino inside the underground framework was achieved. A modified pulsed beam was delivered between May 10th and May 24th 2012, to ensure best timing possibilities. An exact description of the analysis performed by the Borexino collaboration can be found in [116]. As mentioned before (section 5.3.1), a time coincidence between the detected events in the Borexino detector and the beam generation at CERN is essential for the CNGS event tagging. Adding 2.439 ms to the closest CNGS GPS timing tag, the nominal neutrino time-of-flight, a time window of 100 μ s is used as coincidence setting. For the data analysis only events referring to muons detected inside the Inner Vessel that feature a certain track length are regarded. At the end, the observed data set consists of 62 CNGS events. With an exact event-time reconstruction, all events can be folded into a single event distribution. In doing so, all events have to be time corrected for different effects: instrumental delays, geometrical corrections due to the muon event reconstruction and the Sagnac effect. For clarity, the estimated time of flight is subtracted. The final result is depicted in figure 6.7. For a 17 GeV muon neutrino, the time difference to a particle traveling with speed of light is $\delta t = 0.8 \pm 0.7_{stat} \pm 2.9_{sys}$ ns, well consistent with zero.

6.2 BOREXINO Prospects

6.2.1 CNO Neutrinos

At the moment, the CNO neutrino rate is determined just as an upper limit within the pep-neutrino analysis as already mentioned in section 6.1.3. However, with a stable detector and an untouched liquid scintillator, the background prominent for this analysis could be better determined. After a certain time span, the ^{210}Po decay rate will become stable and gets into an equilibrium with the problematic ^{210}Bi . Because of this, it is possible to measure the ^{210}Bi rate via the ^{210}Po decay rate. Then, the energy spectra can be subtracted. Combined with a well-known detector response including the electron quenching effect, the CNO neutrino signal could be detected in this way.

6.2.2 pp Neutrinos

Still under investigation is the determination of the pp neutrino flux and rate that forms 91% of the total solar neutrino flux. Therefore, a pp neutrino rate of 140 counts/(day·100 tons)

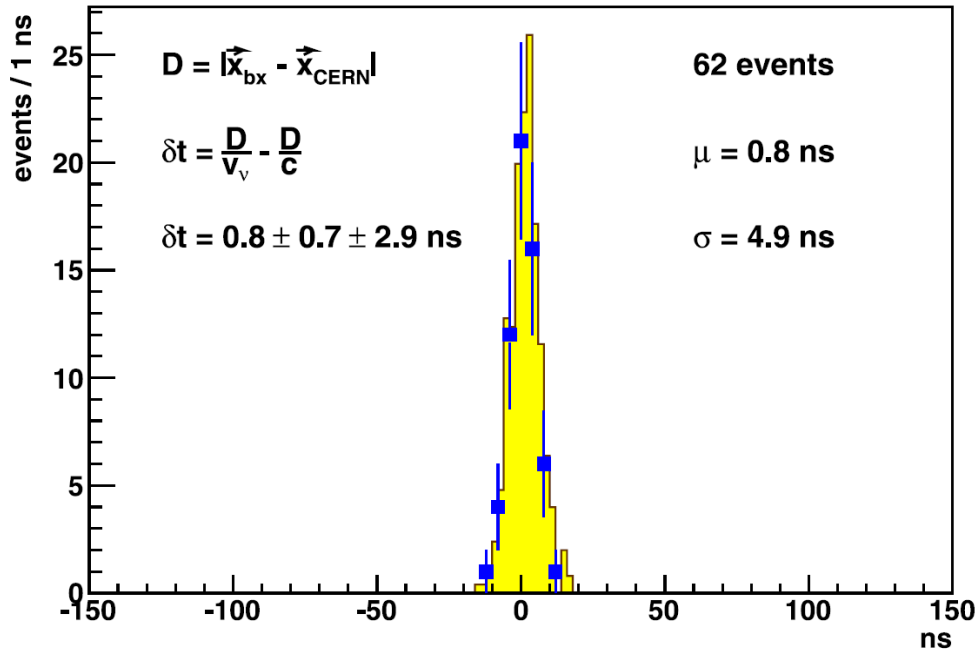


Figure 6.7: Time-of-flight difference between a neutrino and a particle moving at light speed as published in [116] (*reprinted with permission from Elsevier*). The time corrected distribution of all 62 CNGS events folded is depicted by the blue data points and compared to a Monte Carlo simulation (yellow filled area). The mean value, $\delta t = 0.8 \pm 0.7_{stat} \pm 2.9_{sys}$, is in good agreement with zero. It is determined by a Gaussian fit along with the statistical error. The distance between CERN and the center of Borexino is D .

is expected for the Borexino detector. But, as the expected pp-neutrino signals are superimposed by the ^{14}C background signals, the analysis is difficult. With $Q = 157 \text{ keV}$ for the ^{14}C decay and a detector resolution of $\approx 10\%$ in this energy regime the ^{14}C distribution is smeared out up to 200 keV . With more statistics and a well known detector response including the Birks factor k_B for the electron quenching at low energies, it will hopefully be possible to disentangle the different events in the near future.

6.2.3 Short Distance Neutrino Oscillations

Data taken by different experiments yield for a possible additional sterile neutrino state. Because Δm_{41}^2 is expected to be in the order of 1 eV^2 , an oscillation length $\leq 10 \text{ m}$ is expected. With its low background and its large liquid scintillator volume, in addition to the possibility to detect both low-energy electron neutrinos and anti-neutrinos, Borexino has the chance to investigate this subject. Using strong neutrino and anti-neutrino sources placed near the detector (distance of the source to the detector's center $\sim 8 \text{ m}$), short distance neutrino oscillations could be observed within the detector's sensitive volume. A

detailed view of the proposed short distance neutrino oscillation observation can be found in [117].

6.2.4 Supernova Neutrinos

With its approximately 300 t of liquid scintillator, Borexino is a small detector concerning the detection of supernova neutrinos. For a core-collapse Supernova at the center of our galaxy, corresponding to a distance of approximately 10 kpc, 60 - 100 events are expected. In July 2009 Borexino joined the Supernova Early Warning System (SNEWS). With the present pool of neutrino detectors combined there, not only timing information, but also a broad spatial constraint that is dependent on the track reconstruction possibilities of the different detectors, can be given to optical telescopes. Up till now, no alarm has been formed.

Chapter 7

The LENA Project

The physics program of neutrino detectors is limited by the size of the sensitive detector volume available and the achieved radiopurity. However, the functionality of scintillator detectors has been demonstrated with great success. To remove these restrictions, future detectors with bigger sensitive volumes are under investigation. A promising approach is the LENA (Low Energy Neutrino Astronomy) project [18]. In the present chapter, the design and the physics goals, as defined by simulations, will be described briefly.

7.1 Detector Design

LENA is a future liquid scintillator detector that is in principle an enhancement of the Borexino detector. The present design [118], valid for a mine in Pyhäsalmi, Finland, is depicted as a schematic drawing in figure 7.1.

The height of the concrete detector tank is 100 m with a diameter of 32 m. Because of the size of the detector LAB is chosen as liquid scintillator, because of its attenuation length fitting the detector dimensions best. In total, 69.1 kt of LAB with 3 g/l PPO and 20 mg/l BisMSB added are needed. In difference to the Borexino detector no extra buffer liquid is used. The buffer is formed by the scintillator volume contained between the detector walls and the PMT scaffolding. An additional buffer is applied for each PMT included in an optical module. Each of these modules consists of the PMT, the PMT's electronics socket, a connector, μ -metal and light-collecting Winston cones. The housing of an optical module is formed by a steel encapsulation and an acrylic glass window sealing it to one side. The space contained by this window and the PMT's photocathode is filled with a non-scintillating buffer liquid for radioactive shielding. In total, 29600 optical modules are mounted to the scaffolding. Optical modules attached to the cylinder barrel of the scaffolding have their front located 14 m from the detector center axis. To shield the PMTs from light generated in the declared buffer region, the scaffolding is blinded by thin steel plates. The total active volume left for observation consists of 50.8 kt LAB mixture. As outer muon veto, the surrounding cavern is filled with ultra pure water and equipped with 4000 encapsulated PMTs, whereas on the top of the tank plastic scintillator panels with

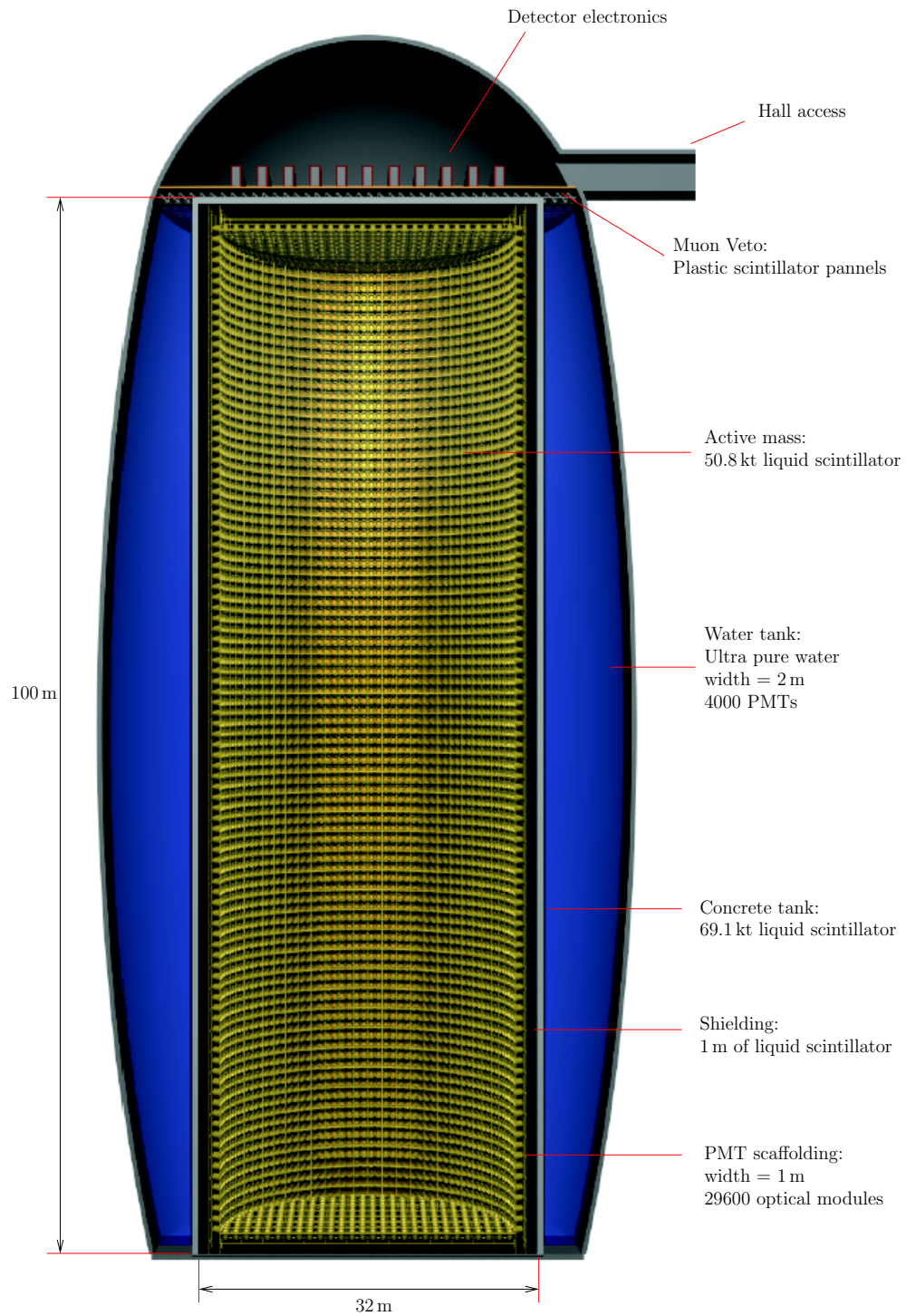


Figure 7.1: Schematic drawing of the future LENA detector.

PMTs are used.

The favoured location for the LENA detector is the already mentioned mine in Pyhäsalmi, Finland. A possible second detector site, the underground laboratory Laboratoire Souterrain de Modane in the Fréjus mountains, France, is investigated in addition.

7.2 Physics Program

In the following, the physics program of the LENA detector will be explained. The simulations performed for this purpose by the different LENA working groups use the detector design described in section 7.1. Being part of the Munich LENA working group, the work presented in course of the present thesis contributes to the simulations performed so far. Until now the kB factor of LAB for electrons was set to 0.15 mm/MeV in the simulations. As demonstrated in section 4.7, this value is still investigated and not yet verified. Especially for low-energy solar neutrinos, the factor can make a difference. Further, it is assumed that the radiopurity in the LENA detector is of the same order of magnitude as achieved by Borexino. The values presented in the following are taken from [18] and [119].

- **Solar Neutrinos**

Due to the big size of the detector, higher event rates as in Borexino are expected in LENA. For the analysis of the different neutrino fluxes, variable fiducial volumes are assumed due to the need of different radioactive shielding. A list of the different rates and the fiducial volumes used for analysis are depicted in table 7.1. Using these values, the MSW-LMA oscillation module can be tested. After four years of measurement, the $P_{ee} = \text{const}$ model can be ruled out with a 5σ significance. In addition, modulations in the ${}^7\text{Be}$ flux, annual modulations or solar cycle modulations, can be observed with a sensitivity of 1% in relative amplitude after one year of measurement. This can be even enhanced to a 0.3% sensitivity in relative amplitude after 10 years of measurement.

| Neutrino Source | Fiducial Mass [kt] | Neutrino Rate [cpd] |
|-----------------|--------------------|---------------------|
| ${}^7\text{Be}$ | 35 | $1.0 \cdot 10^4$ |
| ${}^8\text{B}$ | 35 | 81.4 |
| pep | 30 | $2.8 \cdot 10^2$ |
| CNO | 30 | $1.9 \cdot 10^2$ |
| pp | 30 | 40 |

Table 7.1: Solar neutrino rates as expected for LENA. With up to 200 times higher rates than Borexino, a better neutrino detection sensitivity can be reached for LENA. Data taken from [18].

- **Geoneutrinos**

As the geoneutrino rate is strongly dependent on the Earth's crust, it is therefore dependent on the location of the detector. For the location in Pyhäsalmi a rate of approximately 1000 events per year is expected. In contrast, at a location on the other side of the Earth, like Hawaii, the rate would only be approximately 350 events per year. The possible gained sensitivity in the measurement of the U and Th geoneutrino flux, as well as the U/Th ratio, is, in addition, dependent on the total amount of nuclear power plants in the area. The expected precisions for the two possible detector sites, Pyhäsalmi and Fréjus, are listed in table 7.2. In addition, a new limit on the thermal power of the Earth geo-reactor could be set to 2 TW.

| Location | Live Time [years] | U-flux [%] | Th-flux [%] | U/Th [%] | total geo- ν -flux [%] |
|------------|-------------------|------------|-------------|----------|----------------------------|
| Pyhäsalmi | 1 | 6 | 12 | 17 | 3 |
| | 3 | 3 | 8 | 10 | 2 |
| | 10 | 2 | 4 | 5 | 1 |
| Pyhäsalmi* | 1 | 7 | 14 | 21 | 4 |
| | 3 | 4 | 8 | 11 | 2 |
| | 10 | 2 | 4 | 6 | 1 |
| Fréjus | 1 | 14 | 25 | 35 | 6 |
| | 3 | 9 | 12 | 20 | 3 |
| | 10 | 4 | 7 | 11 | 2 |

Table 7.2: Expected precisions in the geoneutrino measurement for different possible LENA detector sites. * takes future Finnish reactors into account. Due to a smaller rate of reactor antineutrinos in Pyhäsalmi compared to Fréjus, the precisions in the geoneutrino measurement are better in Finland. Data taken from [18].

- **Supernova Neutrinos**

In total, six detection channels can be used to detect supernova neutrinos, three charged (CC) and three neutral (NC) current reactions, as shown in table 7.3. The most prominent one is still the inverse beta decay. The rates presented assume a core collapse supernova at a distance of approximately 10 kpc. In total, $1.6 \cdot 10^4$ events could be recorded, not only enabling a time-dependent analysis. In addition, energy- and flavor-resolved data evaluation would be possible allowing to probe the mechanics of the collapse itself as well as neutrino properties.

- **Diffuse Supernova Neutrino Background (DSNB)**

The main detection channel for the DSNB is the inverse beta decay. This leads to a irreducible background generated by reactor-, geo- and atmospheric electron antineutrinos. Therefore, the observation window for the LENA detector is set between 10 and 30 MeV. With a good signal to background discrimination a rate of 2 to 20

| Channel | Current | # Events |
|---------------------------------|---------|----------|
| IBD | CC | 9250 |
| ν -p | NC | 4179 |
| ν - ^{12}C | NC | 1296 |
| ν -e | NC | 496 |
| ν_e - ^{12}C | CC | 468 |
| $\bar{\nu}_e$ - ^{12}C | CC | 459 |

Table 7.3: Number of events as will be detected by the LENA detector for a core collapse supernova at a distance of approximately 10 kpc for the respective detection channels. The high rate of events and flavor-resolved data allows a more detailed analysis of the mechanics of the collapse itself as possible for Borexino. Data taken from [119].

DSNB antineutrino events per year is expected. The final efficiencies for signal and background rejection are still under investigation.

- **Long Baseline Neutrino Oscillations**

Even LENA is designed primarily for neutrino astronomy, it could be used in combination with a neutrino factory to probe neutrino oscillations. Assuming the CERN as neutrino generating facility pointing towards the LENA detector in Pyhäsalmi, the 2288 km long baseline can be used to search for the neutrino mass hierarchy. As the traversed matter influences and modifies the survival probabilities of neutrinos and antineutrinos over long distances, the sign of this change can be investigated to determine the neutrino mass hierarchy. Regarding the ν_e ($\bar{\nu}_e$) appearance and the ν_μ ($\bar{\nu}_\mu$) disappearance channels, the hierarchy could be determined with an accuracy of more than 5σ after 10 years of measurement. The CP-violation would remain undetected.

- **Neutrino Parameters**

Besides the mass hierarchy mentioned before other basic neutrino parameters could be checked, like θ_{13} . Astrophysical neutrinos could be used to confirm the mixing angle θ_{12} , especially ^8B neutrinos could provide new data for the survival probability of electron neutrinos. In addition, supernova neutrinos could provide the possibility to check for mass hierarchy and mixing angles.

Atmospheric neutrinos could be used to verify and improve the value of the mixing angle θ_{12} and the squared mass difference Δm_{12}^2 as determined by Super-Kamiokande. Expanding the idea of neutrino oscillations, radioactive sources could be used to investigate short baseline oscillations generated by sterile neutrinos, similar to the plans of the Borexino collaboration (see section 6.2.3). Due to the height of LENA of ≈ 100 m a detailed investigation of disappearance oscillation should be possible. In addition to the oscillation length, the spatial resolution allows to observe the oscillation pattern with the squared mass difference in a range of $\Delta m^2 = (0.1 - 2)$ eV.

Even in case of more than one sterile neutrino flavor, the oscillation patterns produced by the different sterile neutrino flavors should be distinguishable from each other.

- **Proton Decay**

With its huge volume, LENA would have the possibility to investigate proton decay. The decay channel of interest for liquid scintillator detectors is $p \rightarrow K^+ \bar{\nu}$. Whereas the produced antineutrino escapes the detector without generating a detectable signal, the produced signal of the decelerating kaon and the signal produced by the decay particle of the kaon, named muon or pion, are visible in the detector. This leads to a double signature of energy deposition detected with a time difference of 12.8 ns. Using the coincidence signal would lead to a total detection efficiency of 65% assuming a good background rejection. With a measuring time of 10 years, a new limit for the proton life time could be set to $\tau_p > 4 \cdot 10^{34}$ years in case no signal is found.

Chapter 8

Conclusion & Outlook

Neutrinos play an important role in modern physics as they can be used as messengers. During time, different experiments were set up to examine various neutrino properties. A state-of-the-art low-energy neutrino experiment is Borexino. Many results have been published by the Borexino collaboration, however, some parts of the detector are still investigated for a better understanding.

Because present neutrino detectors are limited in their prospects due to the size of their sensitive detector volume, bigger detectors are investigated for the future. A promising approach is the LENA project.

The most important part of the Borexino and the LENA detector is formed by the liquid scintillator, their sensitive volumes. Many properties, like light yield and attenuation length, are already well known. On the other hand, the influence of electron quenching is only known blandly. As it has an influence on energy reconstruction and on simulations, it is important to get an exact knowledge of the quenching effect.

Therefore, in the course of this thesis, an experiment was performed to repeal this scarcity. The principle idea of this measurement is to use the properties of Compton scattering along with a radioactive source emitting gamma-particles with a well-known energy, to examine the energy deposited in liquid scintillators. As first test series light yields of different scintillators were determined in course of a Diploma and Bachelor thesis. Using these first tests together with further calibration measurements, the complete experimental setup, from the liquid scintillator to the complete electronics system used, was determined to be stable. The data taken to examine the quenching effect was evaluated by a fit using the so-called Birks formula including the Bethe-Bloch equation modified for electrons.

The first scintillator investigated was a sample of the actual scintillator used in the running Borexino detector. A Birks factor of $k_B = 0.016 \pm 0.001 \frac{\text{cm}}{\text{MeV}}$ was determined. Comparing this value to previous measurements and to the value used for Borexino Monte-Carlo simulations showed good compliance.

Next, the most promising scintillator for the LENA detector, a mixture of LAB with 20 mg/l bisMSB and 3 g/l PPO, was examined. A Birks factor of $k_B = 0.342 \pm 0.013 \frac{\text{cm}}{\text{MeV}}$

was obtained. Compared to PC and other similar scintillators, this factor seems too high. Regarding the attenuation length it turned out that the scintillator used was strongly polluted. Due to the experimental setup had been used and changed for a Bachelor student and the radioactive source used was not available any more immediately after this LAB measurement, an investigation of a new, clean scintillator sample was not possible. In the future, the electron quenching measurement of LENA's LAB scintillator should be redone with a previously cleaned – or better – new sample. In addition, further examinations of light yields and Birks factor determinations for other liquid scintillator experiments are scheduled.

Another important part of the Borexino experiment is formed by the Outer Detector. This water Cherenkov detector serves as an active muon veto. As most of the cosmogenic background generated inside the detector is produced by muons, a good muon identification is essential for a good working experiment.

In the present thesis an analysis was presented that monitors and checks the detection efficiency over time. In total, three different muon tagging systems including the Inner as well as the Outer Detector were used for this purpose. The different tagging systems were compared to each other showing a very stable Outer Detector muon tagging system with a high efficiency of 99.992%. Also the muon identification system of the Inner Detector works flawless during the observed time period. No reason to doubt the overall muon tagging efficiency was found. The monitoring of the different muon identification systems is intended to be continued in the future to grant a good working Outer Detector and in case of problems an easy and fast identification of the damaged muon tagging system.

Another crucial task of Borexino's Outer Detector is the muon track reconstruction. In order to test and validate it, Monte-Carlo simulations performed by a program called G4Bx were used. To consider also effects produced by the electronics, the complete electronics chain had to be implemented in the simulation. For the Inner Detector this simulation tool was already existent (called BxElec), but still missing for the Outer Detector. Therefore, within the present thesis, the total electronics chain starting from the photoelectron detection at the PMT until the final TDC output was simulated. This program was applied to the output data of G4Bx and produced a data set readable with Borexino's normal data handling system Echidna. In this way, the final output of the simulated data now mimics real taken and processed data. The simulation of the Outer Detector's electronics is now working and can be used to test the muon track reconstruction with events simulated.

Not part of this thesis was the construction of a stand-alone trigger module for the Outer Detector simulation. As a result, the event reconstruction shows a hit-timing problem influencing the reconstruction. As the muon-track reconstruction is strongly dependent on the hit-time of the entry- and exit-hit-cluster, the track reconstruction fails or gives wrong results. Hence, the still missing trigger module should be coded in the future.

Borexino has the great possibility to examine the CERN to Gran Sasso (CNGS) neutrino beam. With the beam direction and energy being well-known an exact background-event examination can be performed. Especially the low-energy muons of 16 GeV are of interest to test the neutron tagging mechanism normally used for cosmogenic muon-induced neutrons.

Therefore, in course of this thesis, the neutron production rate of these well-defined 16 GeV CNGS muons in Borexino's liquid scintillator volume was studied. Restricting the observed data to only CNGS beam induced events in addition to other spatial and time cuts, the investigated data set was reduced to a clean muon and neutron sample. A neutron production rate of $(0.063 \pm 0.023) n/\mu$ was determined. Normalized to the total muon-track length, a neutron multiplicity of $(6.8 \pm 2.6) \cdot 10^{-5} n/(\mu \cdot (\text{g}/\text{cm}^2))$ was able to be reported. The value, including errors, was in accordance with simulations performed with Fluka that produced values in the range of $\approx 4 \cdot 10^{-5} n/(\mu \cdot (\text{g}/\text{cm}^2))$ but still showed deviations. First examinations of the difference showed a problem within the simulation package used as also for high-energy muons the simulated values showed divergencies of $\sim 20\%$. Therefore, future studies concerning the simulation and the deviation are scheduled.

Borexino is continuing to take data and together with the work presented in this thesis a more detailed understanding of the detector response is possible. With a stable and well understood detector and well-known radioactive background signals a detection of CNO neutrinos is feasible in the future. Even the possibility to detect pep neutrinos exists.

List of Figures

| | | |
|------|--|----|
| 1.1 | Level-crossing due to matter oscillation | 4 |
| 1.2 | Fusion by the pp-chain in the sun | 5 |
| 1.3 | Fusion by the CNO-cycle in the sun | 6 |
| 1.4 | Neutrino spectra of the SSM | 7 |
| 1.5 | Neutrino flux development around the time of a core collapse Supernova | 8 |
| 1.6 | Geoneutrino spectrum as reported by KamLAND | 10 |
| 2.1 | Borexino detector design | 16 |
| 3.1 | π -electron energy levels of liquid scintillators | 20 |
| 4.1 | Compton scattering kinematics | 26 |
| 4.2 | Schematic setup of the coincidence quenching experiment | 27 |
| 4.3 | The expected Compton spectrum | 28 |
| 4.4 | Picture of the quenching experiment | 29 |
| 4.5 | Schematic drawing of the scintillator container used | 30 |
| 4.6 | Picture of the tin used | 31 |
| 4.7 | Schematic view of the electronics used | 32 |
| 4.8 | Picture of a single recorded PMT-pulse | 34 |
| 4.9 | Affirmation of the coincidence timing | 35 |
| 4.10 | Pictures of all recorded PMT-pulses for one angle measurement of PC | 36 |
| 4.11 | PC energy spectrum of the 165° measurement | 37 |
| 4.12 | Energy linearity of the system, no. 1 | 39 |
| 4.13 | Energy linearity of the system, no. 2 | 40 |
| 4.14 | Time stability of the PC scintillator used | 41 |
| 4.15 | Final fit determining the kB-factor for PC | 42 |
| 4.16 | Final fit determining the kB-factor for LAB | 43 |
| 5.1 | Schematic view of Borexino's Outer Detectors electronics | 48 |
| 5.2 | Structure of the 32-bit data word output of the TDCs | 50 |
| 5.3 | Stability and efficiency of the MTB | 51 |
| 5.4 | Stability and efficiency of the MCR | 52 |
| 5.5 | Stability and efficiency of the IDF | 53 |
| 5.6 | Simplified schematic view of the electronics simulation process | 54 |

| | | |
|------|--|----|
| 5.7 | Overview of the modules essential for the simulation | 55 |
| 5.8 | Schematic view of some simulation parts chain | 59 |
| 5.9 | Muon track reconstruction of simulated data for run number 11000 | 63 |
| 5.10 | Muon track reconstruction of simulated data for run number 14977 | 65 |
| 5.11 | CNGS neutrino beam data sample | 67 |
| 5.12 | Angular distribution of the CNGS muons | 68 |
| 5.13 | Neutron multiplicity for CNGS muons | 69 |
| 6.1 | ^7Be neutrino spectrum as recorded by Borexino | 72 |
| 6.2 | ^8B neutrino spectrum as recorded by Borexino | 73 |
| 6.3 | Final ^8B neutrino spectrum and electron neutrino survival probability | 74 |
| 6.4 | pep neutrino rate as measured by Borexino | 76 |
| 6.5 | Correlation between the pep and CNO neutrino rate and survival probability of electron neutrinos including the pep neutrino rate | 77 |
| 6.6 | Best fits for geoneutrinos with and without a fixed chondritic mass Th/U ratio | 79 |
| 6.7 | Time-of-flight difference between a neutrino and a particle moving at light speed | 81 |
| 7.1 | LENA detector design | 84 |

List of Tables

| | | |
|-----|--|----|
| 1.1 | Generation scheme in the Standard Model | 2 |
| 1.2 | The exchange bosons of the weak interaction | 2 |
| 1.3 | Neutrino oscillation parameters and properties | 4 |
| 1.4 | DSNB limits published by the SuperKamiokande collaboration | 9 |
| 2.1 | Neutrino interactions in liquid scintillators | 13 |
| 3.1 | Attenuation and scattering lengths of liquid scintillators | 22 |
| 3.2 | Influence of the fluor concentration on the light yield | 23 |
| 3.3 | Relative light yield of different scintillators | 23 |
| 4.1 | Overview of the scintillators and fluors used | 31 |
| 4.2 | Investigated liquids for the Double-Chooz detector | 33 |
| 4.3 | Influence of oxygen contamination on the light yield of liquid scintillators | 33 |
| 4.4 | Test series of angles performed for the quenching measurements | 37 |
| 4.5 | Final results for the Birks factor | 43 |
| 7.1 | Solar neutrino rates as expected for LENA | 85 |
| 7.2 | Expected precisions in the geoneutrino measurement for different LENA detector sites | 86 |
| 7.3 | Supernova events as expected for the LENA detector | 87 |

References

- [1] W. Pauli, *Offener Brief an die Gruppe der Radioaktiven bei der Gauvereins-Tagung zu Tübingen*, in *Wissenschaftlicher Briefwechsel mit Bohr, Einstein, Heisenberg u.a.*, 39, Springer, Berlin (1985)
- [2] F. Reines and C. L. Cowan, *The Neutrino*, Nature **178**, 446 (1956)
- [3] B. T. Cleveland, et al., *Measurement of the Solar Electron Neutrino Flux with the Homestake Chlorine Detector*, The Astrophysical Journal **496**, 505 (1998)
- [4] W. Hampel, et al., *GALLEX solar neutrino observations: results for GALLEX IV*, Physics Letters B **447**, 127 (1999)
- [5] M. Altmann, et al., *Complete results for five years of GNO solar neutrino observations*, Physics Letters B **616**, 174 (2005)
- [6] J. Abdurashitov, et al., *Results from SAGE (The Russian-American gallium solar neutrino experiment)*, Physics Letters B **328**, 234 (1994)
- [7] J. N. Bahcall, and H. A. Bethe, *Solution of the solar-neutrino problem*, Phys. Rev. Lett. **65**, 2233 (1990)
- [8] Y. Abe, et al., Double-Chooz Collaboration, *Indication of Reactor $\bar{\nu}_e$ Disappearance in the Double-Chooz Experiment*, Phys. Rev. Lett. **108**, 131801 (2012)
- [9] F. P. An, et al., *Observation of Electron-Antineutrino Disappearance at Daya Bay*, Phys. Rev. Lett. **108**, 171803 (2012)
- [10] S. Abe, et al., The KamLAND Collaboration, *Precision Measurement of Neutrino Oscillation Parameters with KamLAND*, Phys. Rev. Lett. **100**, 221803 (2008)
- [11] R. Wendell, et al., The Super-Kamiokande Collaboration, *Atmospheric neutrino oscillation analysis with subleading effects in Super-Kamiokande I, II, and III*, Phys. Rev. D **81**, 092004 (2010)
- [12] P. Adamson, et al., MINOS Collaboration, *Measurement of Neutrino and Antineutrino Oscillations Using Beam and Atmospheric Data in MINOS*, Phys. Rev. Lett. **110**, 251801 (2013)

- [13] K. Abe, et al., The T2K Collaboration, *First muon-neutrino disappearance study with an off-axis beam*, Phys. Rev. D **85**, 031103 (2012)
- [14] S. M. Bilenky, *Majorana neutrino mixing*, Journal of Physics G: Nuclear and Particle Physics **32**, R127 (2006)
- [15] R. Abbasi, et al., IceCube Collaboration, *Measurement of the atmospheric neutrino energy spectrum from 100 GeV to 400 TeV with IceCube*, Phys. Rev. D **83**, 012001 (2011)
- [16] S. Adrián-Martínez, et al., *Measurement of atmospheric neutrino oscillations with the ANTARES neutrino telescope*, Physics Letters B **714**, 224 (2012)
- [17] G. Alimonti, et al., *Science and technology of Borexino: a real-time detector for low energy solar neutrinos*, Astroparticle Physics **16**, 205 (2002)
- [18] M. Wurm, et al., *The next-generation liquid-scintillator neutrino observatory LENA*, Astroparticle Physics **35**, 685 (2012)
- [19] Particle Data Group, *Review of Particle Physics*, Physics Letters B **667** (2008)
- [20] B. Povh, et al., *Teilchen und Kerne*, Springer-Verlag Berlin Heidelberg (2004)
- [21] M. Fukugita, and T. Yanagida, *Physics of Neutrinos*, Springer-Verlag Berlin Heidelberg (2003)
- [22] Scottish Graduate Series, *Neutrinos in Particle Physics, Astrophysics and Cosmology*, CRC Press (2008)
- [23] N. Schmitz, *Neutrino Physik*, Teubner, Stuttgart (1997)
- [24] B. Aharmim, et al., SNO Collaboration, *Low-energy-threshold analysis of the Phase I and Phase II data sets of the Sudbury Neutrino Observatory*, Phys. Rev. C **81**, 055504 (2010)
- [25] A. Gando, et al., KamLAND Collaboration, *Constraints on θ_{13} from a three-flavor oscillation analysis of reactor antineutrinos at KamLAND*, Phys. Rev. D **83**, 052002 (2011)
- [26] K. Abe, et al., Super-Kamiokande Collaboration, *Solar neutrino results in Super-Kamiokande-III*, Phys. Rev. D **83**, 052010 (2011)
- [27] P. Adamson, et al., MINOS Collaboration, *Measurement of the Neutrino Mass Splitting and Flavor Mixing by MINOS*, Phys. Rev. Lett. **106**, 181801 (2011)
- [28] J. Hosaka, et al., Super-Kamiokande Collaboration, *Three flavor neutrino oscillation analysis of atmospheric neutrinos in Super-Kamiokande*, Phys. Rev. D **74**, 032002 (2006)

- [29] J. K. Ahn, et al., RENO Collaboration, *Observation of Reactor Electron Antineutrinos Disappearance in the RENO Experiment*, Phys. Rev. Lett. **108**, 191802 (2012)
- [30] C. Weinheimer, et al., *High precision measurement of the tritium spectrum near its endpoint and upper limit on the neutrino mass*, Physics Letters B **460**, 219 (1999)
- [31] L. Bornschein, KATRIN Collaboration, *The KATRIN experiment - a direct measurement of the electron antineutrino mass in the sub-eV region*, Nuclear Physics A **752**, 14 (2005)
- [32] S. Schönert, et al., *The GERmanium Detector Array (Gerda) for the search of neutrinoless $\beta\beta$ decays of ^{76}Ge at LNGS*, Nuclear Physics B - Proceedings Supplements **145**, 242 (2005)
- [33] J. Beringer, et al., Particle Data Group, *Review of Particle Physics*, Phys. Rev. D **86**, 010001 (2012)
- [34] J. N. Bahcall, A. M. Serenelli, and S. Basu, *10,000 Standard Solar Models: A Monte Carlo Simulation*, The Astrophysical Journal Supplement Series **165**, 400 (2006)
- [35] J. N. Bahcall, A. M. Serenelli, and S. Basu, *New Solar Opacities, Abundances, Helioseismology, and Neutrino Fluxes*, The Astrophysical Journal Letters **621**, L85 (2005)
- [36] A. Burrows, *Supernova explosions in the Universe*, Nature **403**, 727 (2000)
- [37] S. Woosley and T. Janka, *The physics of core-collapse supernovae*, Nat Phys **1**, 147 (2005)
- [38] M. Liebendörfer, et al., *A Finite Difference Representation of Neutrino Radiation Hydrodynamics in Spherically Symmetric General Relativistic Spacetime*, The Astrophysical Journal Supplement Series **150**, 263 (2004)
- [39] P. Antonioli, et al., *SNEWS: the SuperNova Early Warning System*, New Journal of Physics **6**, 114 (2004)
- [40] M. A. Ruderman, *Astrophysical neutrinos*, Reports on Progress in Physics **28**, 411 (1965)
- [41] S. E. Woosley, J. R. Wilson and R. Mayle, *Gravitational Collapse and the Cosmic Antineutrino Background*, The Astrophysical Journal **302**, 19 (1986)
- [42] J. F. Beacom, *The Diffuse Supernova Neutrino Background*, Annual Review of Nuclear and Particle Science **60**, 439 (2010)
- [43] S. Ando and K. Sato, *Relic neutrino background from cosmological supernovae*, New Journal of Physics **6**, 170 (2004)

- [44] S. Ando and K. Sato, *Supernova relic neutrinos and observational implications for neutrino oscillation*, Physics Letters B **559**, 113 (2003)
- [45] M. Malek, et al., *Search for Supernova Relic Neutrinos at Super-Kamiokande*, Physical Review Letters **90**, 061101 (2003)
- [46] M. Wurm, et al., *Detection potential for the diffuse supernova neutrino background in the large liquid-scintillator detector LENA*, Physical Review D **75**, 023007 (2007)
- [47] A. Rubbia, *Underground neutrino detectors for particle and astroparticle Science: The Giant Liquid Argon Charge Imaging Experiment (GLACIER)*, Journal of Physics: Conference Series **171**, 012020 (2009)
- [48] G. Eder, *Terrestrial neutrinos*, Nuclear Physics **78**, 657 (1966)
- [49] S. T. Dye, *Geoneutrinos and the radioactive power of the Earth*, Reviews of Geophysics **50** (2012)
- [50] Committee on the Status and National Research Council Research Objectives in the Solid-Earth Sciences, *Solid-Earth Sciences and Society*, The National Academies Press (1993)
- [51] J. M. Herndon, *Nuclear georeactor origin of oceanic basalt $^3\text{He}/^4\text{He}$, evidence, and implications*, Proceedings of the National Academy of Sciences **100**, 3047 (2003)
- [52] T. Araki, et al., *Experimental investigation of geologically produced antineutrinos with KamLAND*, Nature **436**, 499 (2005)
- [53] K. S. Hirata, et al., *Observation in the Kamiokande-II detector of the neutrino burst from supernova SN1987A*, Phys. Rev. D **38**, 448 (1988)
- [54] S. Fukuda, et al., *The Super-Kamiokande detector*, Nuclear Instruments and Methods in Physics Research Section A: Accelerators, Spectrometers, Detectors and Associated Equipment **501**, 418 (2003)
- [55] C. Arpesella, et al., *Measurements of extremely low radioactivity levels in BOREXINO*, Astroparticle Physics **18**, 1 (2002)
- [56] G. Alimonti, et al., Borexino Collaboration, *The liquid handling systems for the Borexino solar neutrino detector*, Nuclear Instruments and Methods in Physics Research Section A: Accelerators, Spectrometers, Detectors and Associated Equipment **609**, 58 (2009)
- [57] Re-edited by S-O Flyckt and Carole Marmonier, *Photomultiplier Tubes Principles and Applications*, Photonis (2002)
- [58] W. R. Leo, *Techniques for Nuclear and Particle Physics Experiments*, Springer-Verlag Berlin (1994)

- [59] M. Wurm, *Cosmic Background Discrimination for Rare Neutrino Event Search in Borexino and LENA*, Ph.D. thesis, Technische Universität München (2009)
- [60] A. Ianni, D. Montanino, and F. Villante, *How to observe 8B solar neutrinos in liquid scintillator detectors*, Physics Letters B **627**, 38 (2005)
- [61] J. F. Beacom, W. M. Farr, and P. Vogel, *Detection of supernova neutrinos by neutrino-proton elastic scattering*, Phys. Rev. D **66**, 033001 (2002)
- [62] Y. Abe, et al., Double-Chooz Collaboration, *Reactor $\bar{\nu}_e$ disappearance in the Double-Chooz experiment*, Phys. Rev. D **86**, 052008 (2012)
- [63] J. Benziger, et al., *The nylon scintillator containment vessels for the Borexino solar neutrino experiment*, Nuclear Instruments and Methods in Physics Research Section A: Accelerators, Spectrometers, Detectors and Associated Equipment **582**, 509 (2007)
- [64] T. Lewke, *Calibration and Efficiency Determination of the Borexino Muon Veto Based on the First Realtime Measurements of ^7Be Solar Neutrinos*, Diploma thesis, Technische Universität München (2007)
- [65] A. Jabłoński, *Über den Mechanismus der Photolumineszenz von Farbstoffphosphoren*, Zeitschrift für Physik **94**, 38 (1935)
- [66] J. B. Birks, *The Theory and Practice of Scintillation Counting*, Pergamon Press, New York (1964)
- [67] J. B. Birks, *The Efficiency of Organic Scintillators*, Proceedings of the University of New Mexico Conference on Organic Scintillation Detectors (1960)
- [68] M. Wurm, et al., *Optical scattering lengths in large liquid-scintillator neutrino detectors*, Review of Scientific Instruments (2010)
- [69] J. Meyer, *Realization and Characterization of the Muon Veto Scintillator and the Buffer Liquid of the Double-Chooz Experiment*, Diploma thesis, Technische Universität München (2010)
- [70] M. Wurm, *Untersuchungen zu den optischen Eigenschaften eines auf PXE basierenden Flüssigszintillators und zum Nachweis von "Supernovae Relic Neutrinos" mit dem zukünftigen Neutrinodetektor LENA*, Diploma thesis, Technische Universität München (2005)
- [71] D. Hellgartner, *Lepton track reconstruction in LENA and attenuation length measurements in liquid scintillators*, Diploma thesis, Technische Universität München (2011)

- [72] S. Todor, *Solar neutrinos with LENA and a spectroscopical analysis of liquid-scintillators*, Diploma thesis, Technische Universität München (2008)
- [73] H. Back, et al., *Study of neutrino electromagnetic properties with the prototype of the Borexino detector*, Physics Letters B **563**, 35 (2003)
- [74] H. O. Back, et al., *Study of phenylxylylethane (PXE) as scintillator for low energy neutrino experiments*, Nuclear Instruments and Methods in Physics Research Section A: Accelerators, Spectrometers, Detectors and Associated Equipment **585**, 48 (2008)
- [75] G. Alimonti, et al., *Light propagation in a large volume liquid scintillator*, Nuclear Instruments and Methods in Physics Research Section A: Accelerators, Spectrometers, Detectors and Associated Equipment **440**, 360 (2000)
- [76] G. Alimonti, et al., Borexino Collaboration, *The Borexino detector at the Laboratori Nazionali del Gran Sasso*, Nuclear Instruments and Methods in Physics Research Section A: Accelerators, Spectrometers, Detectors and Associated Equipment **600**, 568 (2009)
- [77] J. M. Winter, *Phenomenology of Supernova Neutrinos, Spatial Event Reconstruction, and Scintillation Light Yield Measurements for the Liquid-Scintillator Detector LENA*, Diploma thesis, Technische Universität München (2007)
- [78] J. B. Birks, *Scintillations from Organic Crystals: Specific Fluorescence and Relative Response to Different Radiations*, Proceedings of the Physical Society. Section A **64**, 874 (1951)
- [79] C. Aberle, *Optimization, simulation and analysis of the scintillation signals in the Double-Chooz experiment*, Ph.D. thesis, Ruperto-Carola University of Heidelberg (2011)
- [80] S. M. Seltzer and M. J. Berger, *Evaluation of the collision stopping power of elements and compounds for electrons and positrons*, The International Journal of Applied Radiation and Isotopes **33**, 1189 (1982)
- [81] S. M. Seltzer and M. J. Berger, *Improved procedure for calculating the collision stopping power of elements and compounds for electrons and positrons*, The International Journal of Applied Radiation and Isotopes **35**, 665 (1984)
- [82] T. M. Undagoitia, *Measurement of light emission in organic liquid scintillators and studies towards the search for proton decay in the future large-scale detector LENA*, Ph.D. thesis, Technische Universität München (2008)
- [83] F. Elisei, et al., *Measurements of liquid scintillator properties for the Borexino detector*, Nuclear Instruments and Methods in Physics Research Section A: Accelerators, Spectrometers, Detectors and Associated Equipment **400**, 53 (1997)

- [84] S. M. Prummer, *Bestimmung optischer Parameter und der Stabilität des Flüssigszintillators für den LENA - Detektor*, Bachelor thesis, Technische Universität München (2012)
- [85] R. Brun and F. Rademakers, *ROOT - An Object Oriented Data Analysis Framework*, in *Proceedings AIHENP'96 Workshop*, Nucl. Inst. & Meth. in Phys. Res. A 389 (1996)
- [86] V. Zimmer, *Private communications*, Technische Universität München (2013)
- [87] D. Hellgartner, *Private communications*, Technische Universität München (2013)
- [88] <http://home.web.cern.ch/> (2013)
- [89] C. Galbiati, et al., *Cosmogenic ^{11}C production and sensitivity of organic scintillator detectors to pep and CNO neutrinos*, Phys. Rev. C **71**, 055805 (2005)
- [90] G. Bellini, et al., Borexino Collaboration, *Measurement of the solar ^8B neutrino rate with a liquid scintillator target and 3 MeV energy threshold in the Borexino detector*, Phys. Rev. D **82**, 033006 (2010)
- [91] D. D'Angelo, *Towards the detection of low energy solar neutrinos in BOREXino: data readout, data reconstruction and background identification*, Ph.D. thesis, Technische Universität München (2006)
- [92] J. Allison, et al., *Geant4 developments and applications*, Nuclear Science, IEEE Transactions on **53**, 270 (2006)
- [93] S. Agostinelli, et al., *Geant4a simulation toolkit*, Nuclear Instruments and Methods in Physics Research Section A: Accelerators, Spectrometers, Detectors and Associated Equipment **506**, 250 (2003)
- [94] G. Bellini, et al., Borexino Collaboration, *Muon and cosmogenic neutron detection in Borexino*, Journal of Instrumentation **6**, P05005 (2011)
- [95] R. Acquafredda, et al., *The OPERA experiment in the CERN to Gran Sasso neutrino beam*, Journal of Instrumentation **4**, P04018 (2009)
- [96] I. Efthymiopoulos, et al., *First Year Physics at CNGS, presented at PAC09, Vancouver, Canada, 4-8 May 2009*, Technical Report EuCARD-CON-2009-013 (2009)
- [97] A. Empl, *Borexino Internal Report* (2012)
- [98] G. Battistoni, et al., *The FLUKA code: Description and benchmarking*, in *Hadronic Shower Simulation Workshop*, volume 896 of *AIP Conference Proceedings*, 31–49 (2007)
- [99] A. Ferrari, et al., *FLUKA: A multi-particle transport code*, CERN-2005-10, INFN/TC.05/11, SLAC-R-773 (2005)

- [100] A. Empl, Q. Meindl, and M. Wurm, *Borexino private communications* (2012)
- [101] G. Bellini, et al., Borexino Collaboration, *Cosmogenic Backgrounds in Borexino at 3800 m water-equivalent depth*, to be submitted (2013)
- [102] R. Möllenberg, *Private communications*, Technische Universität München (2013)
- [103] C. Arpesella, et al., Borexino Collaboration, *First real time detection of ${}^7\text{Be}$ solar neutrinos by Borexino*, Physics Letters B **658**, 101 (2008)
- [104] G. Bellini, et al., Borexino Collaboration, *Precision Measurement of the ${}^7\text{Be}$ Solar Neutrino Interaction Rate in Borexino*, Phys. Rev. Lett. **107**, 141302 (2011)
- [105] B. Aharmim, et al., SNO Collaboration, *Electron energy spectra, fluxes, and day-night asymmetries of ${}^8\text{B}$ solar neutrinos from measurements with NaCl dissolved in the heavywater detector at the Sudbury Neutrino Observatory*, Phys. Rev. C **72**, 055502 (2005)
- [106] B. Aharmim, et al., SNO Collaboration, *Determination of the ν_e and total ${}^8\text{B}$ solar neutrino fluxes using the Sudbury Neutrino Observatory Phase I data set*, Phys. Rev. C **75**, 045502 (2007)
- [107] B. Aharmim, et al., SNO Collaboration, *Independent Measurement of the Total Active ${}^8\text{B}$ Solar Neutrino Flux Using an Array of ${}^3\text{He}$ Proportional Counters at the Sudbury Neutrino Observatory*, Phys. Rev. Lett. **101**, 111301 (2008)
- [108] J. Hosaka, et al., Super-Kamiokande Collaboration, *Solar neutrino measurements in Super-Kamiokande-I*, Phys. Rev. D **73**, 112001 (2006)
- [109] J. P. Cravens, et al., The Super-Kamiokande Collaboration, *Solar neutrino measurements in Super-Kamiokande-II*, Phys. Rev. D **78**, 032002 (2008)
- [110] L. Wolfenstein, *Neutrino oscillations in matter*, Phys. Rev. D **17**, 2369 (1978)
- [111] G. Bellini, et al., Borexino Collaboration, *First Evidence of pep Solar Neutrinos by Direct Detection in Borexino*, Phys. Rev. Lett. **108**, 051302 (2012)
- [112] G. Bellini, et al., Borexino Collaboration, *Observation of geo-neutrinos*, Physics Letters B **687**, 299 (2010)
- [113] G. Bellini, et al., Borexino Collaboration, *Measurement of geo-neutrinos from 1353 days of Borexino*, Physics Letters B **722**, 295 (2013)
- [114] T. Adam, et al., OPERA Collaboration, *Measurement of the neutrino velocity with the OPERA detector in the CNGS beam*, arXiv:1109.4897v1 [hep-ex] (2011)
- [115] T. Adam, et al., OPERA Collaboration, *Measurement of the neutrino velocity with the OPERA detector in the CNGS beam*, arXiv:1109.4897v4 [hep-ex] (2012)

- [116] P. A. Sanchez, et al., Borexino Collaboration, *Measurement of CNGS muon neutrino speed with Borexino*, Physics Letters B **716**, 401 (2012)
- [117] Borexino Collaboration, *SOX: Short distance neutrino Oscillations with BoreXino*, arXiv:1304.7721v2 [physics.ins-det] (2013)
- [118] D.Hellgartner, et al., *Liquid Scintillator Specification Document*, Internal Laguna Report **v0.1** (2012)
- [119] D.Hellgartner, et al., *Report on Detector Performance Evaluation*, Internal Laguna Report **v0.13** (2013)

Acknowledgement

The present thesis developed during my time at the Chair for Experimental Physics and Astroparticle Physics E15 of the Technische Universität München. My gratitude to Professor Dr. Stefan Schönert and Professor Dr. Franz von Feilitzsch must be expressed for giving me this opportunity.

Further, I want to thank my doctoral adviser Professor Dr. Lothar Oberauer. His guidance and support were essential for this work. In addition, many conversations not related to the topic generated a relaxed and friendly atmosphere.

Next, I am grateful to Dr. Jürgen Friese and Dr. Roman Gernhäuser of the Chair E12 for giving me the possibility to use their radioactive source. Without this source the performed measurements would have been impossible.

Great thanks go to all the members of our work shop. Their contribution and know-how were important for a working experiment.

All the members and colleagues of the chair E15 must be thanked. For the time everyone was forbidden to enter the Neutrino-Laboratory my excuses have once more to be expressed. For all the discussions concerning physics and non-professional subjects my thanks have to be applied. Also the very pleasant atmosphere at our chair has to be mentioned. Our secretary Maria Bremberger must be mentioned for all the help and being very patient.

Thanks to all the members of the Borexino Collaboration for always giving me a warm welcome and some fascinating time in Italy.

Most important my family. Without the support of my brother and my parents all I have achieved so far would not have been possible.